5-2019

Determining the Influence of Lateral Margin Mechanical Properties on Glacial Flow

Kate Hruby
University of Maine, kate.hruby@maine.edu

DETERMINING THE INFLUENCE OF LATERAL MARGIN MECHANICAL PROPERTIES ON GLACIAL FLOW

By

Kate Hruby

B.A. University of New England, 2016

A THESIS

Submitted in Partial Fulfillment of the

Requirements for the Degree of

Master of Science

(in Earth and Climate Sciences)

The Graduate School

The University of Maine

May 2019

Advisory Committee:

Christopher Gerbi, Professor of Earth and Climate Sciences, Advisor

Peter Koons, Professor of Earth and Climate Sciences

Seth Campbell, Professor of Earth and Climate Sciences

DETERMINING THE INFLUENCE OF LATERAL MARGIN MECHANICAL PROPERTIES ON GLACIAL FLOW

By Kate Hruby

Thesis Advisor: Dr. Christopher Gerbi

An Abstract of the Thesis Presented
in Partial Fulfillment of the Requirements for the
Degree of Master of Science
(in Earth and Climate Sciences)

May 2019

The lateral margins of glaciers and ice streams play a significant role in glacial flow. Depending on their properties, like temperature and ice crystal orientation, they can cause a resistance to flow or enhance it. In combination with our current changing climate, flow patterns can dictate the mass balance of an ice body. It is therefore more important than ever to understand the impact that variations at the margins can have on flow. However, the lateral margins of glaciers and ice streams are an often-neglected part of ice dynamics; they are harder to sample than the center of a glacier's flow path because of debris and crevassing, so we have little data about them. We are attempting to change that. To assess the sensitivity of flow to material properties of the ice, I join computer modeling with measurements taken on the lateral margin of a mountain glacier. My sensitivity analysis is two-fold: 1) I combine synthetic geometries and parameters to provide conclusions regarding the effect lateral margins have on glacier flow, and 2) I use properties of Jarvis Glacier, Alaska as a case study for the input of *in situ* fabrics and temperatures into my model.

In complementary work, we have measured the geometry and velocity of Jarvis Glacier, Alaska, as well as the thermal profile and crystal orientation at two locations 25 m and 100 m from the lateral margin. This access to a realistic scenario provides a reference for the sensitivity tests, allowing us to understand what parameters have the greatest impact on 3D glacial velocity. In the following chapters, the questions I address in depth are: 1) to what extent do ice crystal fabric and temperature in the lateral margins matter in determining glacial flow, and 2) have we accurately captured the essential mechanics of these parameters and their relationship to flow? Results show that while Jarvis's warm lateral margin temperatures do alter flow, the glacier's weakly-oriented fabric does not. However, if the ice crystals in a glacier were more oriented than they are in Jarvis, flow could double, or even triple, especially if the glacier has a frozen bed. By adding just 10 m of highly oriented ice crystals to the sides of an ice body, flow increases by 26% and that number rises the farther into the glacier I assign the oriented fabric. Temperature changes create similar patterns. My models produce expected stress and strain rate relationships throughout the ice body and can capture part of the deformation occurring naturally in Jarvis; horizontal shear in my model matches what we measured in Jarvis near the surface and underestimates what we measured in Jarvis near the bed. This deviation near the bed is most likely from weak till or water, variables that my model does not account for. To address these missing components in the future, a user could manipulate the open-source modeling software I am using as a platform for this project. Given the potential influence of parameters like crystal orientation and temperature on the overall movement of an ice body, it is imperative we both acquire more data at the lateral margins of glaciers and ice streams as well as include those data into flow calculations to more accurately model and predict the behavior of ice.

TABLE OF CONTENTS

LIST OF TABLES

LIST OF FIGURES

CHAPTER 1

PROPERTIES AND BEHAVIORS OF ICE

1.1 Glaciers and Society

Black Rapids, Alaska (Figure 1.1): a town populated by more glaciers than buildings, more frequented by moose than people. Despite the apparent emptiness and lack of habitation, Black Rapids is home to a tourist lodge, a glacier-fed river, an oil pipeline and a dynamic history. Standing on the road beneath the mountains of the Eastern Alaska Range and looking out across the Delta River one can see evidence of a landscape shaped by mountain glaciers. In 1936, Black Rapids Glacier surged toward Delta River and then began receding in 1937, leaving behind moraines far out into the valley that have not been touched since, and will likely never be touched again (Kienholz et al. 2017). This is good news for the Trans-Alaska oil pipeline across the river, which has a risk of damage from a surge, but bad news for the people who rely on the meltwater runoff of this glacier. Due to our changing climate, Black Rapids Glacier is getting thrown off balance in the 21st century, meaning it might disappear completely in the 22nd (Kienholz et al. 2017).

Figure 1.1: Black Rapids, Alaska. In the center of the image, Black Rapids Glacier is visible between the central mountains of the Alaska Range. Delta River, Black Rapids Lodge, the Alaska Highway and the Trans-Alaska Pipeline are in the foreground.

Turn around and look east from that spot on the road and you will see mountains shoot right up from the ground, piercing the clouds settling in with gusts of wind. Hidden within those mountains is Jarvis Glacier, an ice body smaller than Black Rapids Glacier, but with no less of an impact. Jarvis Creek, the meltwater coming from the ice and snow, flows into Delta River. These creeks and rivers are the drinking water and fishing grounds for the people who live near its banks.

This reliance on glaciers is a theme in mountain communities across the globe, which are feeling air temperatures increase at unprecedented rates (Mountain Research Initiative EDW Working Group 2015). Alaskan mountains could see 4.5˚C of air temperature change by the end of the century, increasing ice melt and disrupting the contribution glaciers provide to a watershed; in dry months, a glacier is a source of drinking water and irrigation even if there isn't any rain (Bradley et al. 2006). Once a glacier disappears, the watershed no longer has its buffer, and mountain communities will be much more reliant on rain water throughout the year. We must remember, also, that glaciers are not just a consumption need, but an energy and infrastructure one as well. Communities in the Andes in South America rely on hydropower, and as water flux becomes inconsistent, these communities will have to find other forms of energy, such as fossil fuels (Bradley et al. 2006), perpetuating another lobe of the positive feedback loop that is accelerating climate change. Summer tourism in the Alps depends on 40,000 km of trail and hut networks that are increasingly susceptible to landslides and rockfalls as glaciers retreat; the more the ice retreats, the more maintenance must go into these networks and the more unsafe these regions become for hikers, mountaineers and scientists (Ritter et al. 2012). Sea level rise is also a valid concern, and one that impacts communities across the globe. Even though mountain glaciers have a smaller footprint in the cryosphere than the Greenland and Antarctic ice sheets, the

contribution to sea level rise from mountain glaciers will be around 10 centimeters by 2100, which amounts to about a third of all sea level rise in this century (Radić and Hock 2011).

To allow for communities to adapt to coming changes in our environment, we need glacier models that can accurately predict flow, both the patterns of today and the patterns of the future. Despite the importance of understanding ice behavior, significant uncertainties exist about the mechanical properties of ice that determine how it viscously moves, such as the impact of lateral margins. Flow laws have been developed through lab and field experiments with ice collected on the flow lines and divides of glaciers and ice sheets (Haefeli 1952; Colbeck and Evans 1973; Gow and Williamson 1976; Hooke 1981; Herron and Langway 1982; Pimienta et al. 1987; Lipenkov et al. 1989; Thorsteinsson et al. 1997; Wang et al. 2002). Data from these locations can be extrapolated out to the lateral margin, however, due to lack of *in situ* measurements, our expectations of ice parameters on the margin are just that, expectations (Bons et al. 2018). The lateral margins of an ice body can provide up to 100% of the glacier's resistance to flow (Jackson and Kamb 1997; Raymond et al. 2001), so flow laws and glacier models have therefore been missing a large region of data that could make a substantial difference to flow predictions.

Ice is a unique material. With a density of 917 kg/m^3 it is lighter than its liquid form. It is a non-Newtonian fluid, so its viscosity depends on stress, and when compiled into a large body, it will flow under its own weight. Ice is anisotropic, and therefore easier to deform in one direction than another. This preferred deformation direction, which is along the base of an ice crystal, can be ten times less viscous than other directions (Alley 1988). Due to these properties, there are three crucial aspects of ice that can change how a glacier deforms and flows: 1) the temperature of the ice, 2) the orientation of the ice crystals and 3) the interactions the ice has with the bed. While there are of course many other factors that increase the complexity of glacial flow, I will focus on

these three aspects for the rest of this study to isolate their specific influence on the flow of an ice body.

1.2 Temperature

Temperature can affect glacial flow in many ways, from basal warming creating a wet-bed hydrological scenario to higher temperatures softening ice. Basal warming can come from frictional heating as the ice slides over the bed, deformational heating as the ice contacts the rock, or from the conduction of geothermal heat from the earth (Bjornsson et al. 1996; Engelhardt 2004). Because glaciers flow, there is also the potential to advect warm or cold ice. For example, cold ice from a higher-elevation can advect to a lower-elevation and cause the ice to freeze to the bed in an overall warmer ice regime, or vice versa if warmer ice is advecting down glacier (Bjornsson et al. 1996). When ice is above -10˚C, which is a common occurrence in mountain glaciers, deformation rates are increasingly dependent on temperature as the ice gets closer to melting (Mellor and Testa 1969).

Glaciers usually follow a pattern of colder ice at the surface where there is contact with a cold atmosphere, and warmer ice below where there is strain and geothermal heating. In summer months, there can be an inverse of this pattern as warmer air temperatures heat up the surface of the ice, though ice temperatures at the bed stay relatively constant. Occasionally, a polythermal effect takes place, where a glacier is temperate in the accumulation area due to snow cover insulation (latent heat from refreezing meltwater and increasing pressures keeping the ice warm), and then is colder in the ablation area where there is less insulation and heat travels through conduction only (Bjornsson et al. 1996). The smaller the glacier, the less heat is insulated in the ice, and the colder the glacier can be in the accumulation area, causing localized meltwater patterns

where water only reaches the bed through moulins and crevasses (Maohuan 1990; Bjornsson et al. 1996). But no matter the thermal regime of these mountain glaciers, we generally see temperatures from -10˚C in the coldest regions to 0˚C in the warmest regions, with temperate glaciers staying above -1˚C (Maohuan 1990; Bjornsson et al. 1996).

1.3 Fabric

Ice crystal orientation, known as fabric and referenced as such from here on, is determined by the direction of the ice crystal's c-axis, or the axis normal to the basal plane of the crystal. If ice is isotropic, it means the fabric is the same no matter what orientation you look at it: the c-axes point in all directions. However, ice is often anisotropic, and the c-axes will align in specific ways depending on strain. Three common fabric expressions are isotropic, single-maximum and girdle (Figure 1.2). Isotropic fabrics occur usually on the surface of ice bodies where the ice has not deformed, maximum fabrics occur when simple shear is the dominant form of deformation, small circle fabrics (or maximum fabrics with a gap in the center) occur through vertical compression, and girdle fabrics occur when there is extension (Hooke and Hudleston 1981; Alley 1992). As a rule of thumb, c-axes will rotate toward compression, away from tension and perpendicular to shear (Alley 1992). The development of these fabrics are a feedback loop wherein the crystals preferentially slip on the basal planes perpendicular to the c-axis. The more deformation that occurs, the more the crystals align, which can in turn increase the flow (Pimienta et al. 1987). To disrupt the feedback loop, ensuring glaciers don't run away from themselves, the crystals deform so stresses are transferred to a stronger direction of the grain (Duval et al. 2010). This concept, known as work hardening, can change the viscous deformation patterns of ice at the individual-crystal scale and shows the complexity of modeling large ice bodies, as discussed in section 2.1.

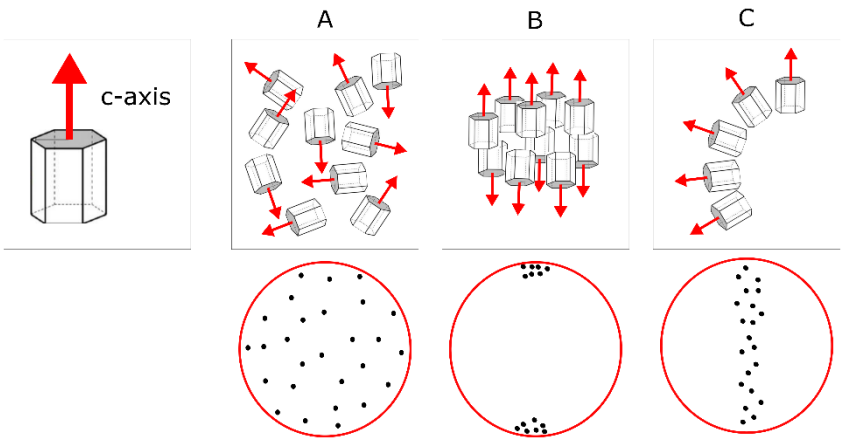

Figure 1.2: Schematic of three possible ice fabrics. Shown are (A) an isotropic fabric, (B) a single-maximum fabric and (C) a girdle fabric. The top row is a representation of the ice crystals while the bottom row is the diagrammatic way to record the c-axis orientation according to the fabric above.

In ice sheets, where much of our *in situ* knowledge originates from, fabric patterns usually become more concentrated with depth, often trending to vertical single-maximum fabrics near the bed (Gow and Williamson 1976; Herron and Langway 1982; Thorsteinsson et al. 1997; Wang et al. 2002; Gillet-Chaulet et al. 2005). These concentrated fabrics can be caused by shear along the base of the ice body (Pimienta et al. 1987). In temperate glacier flow-line studies, single maximum fabrics develop as well but are less concentrated because the ice is closer to the melting point (Gow and Williamson 1976).

Occasional studies appear in which the site is not aligned with a flow line and results suggest that marginal ice crystals orient to the shear zone, whether that zone is caused by bedrock features like mountains (Azuma et al. 1985), from the ending of an ice sheet (Hudleston 1980), or from the lateral transition of an ice stream to an ice sheet (Jackson and Kamb 1997; Minchew et al. 2018). Nevertheless, these studies still underrepresent mountain glaciers, perhaps the ice bodies most affected by bedrock.

1.4 Bed Interactions

Just as the flow of toothpaste is determined by its tube, so is a glacier's flow determined by its surrounding valley. Rock type, temperature and pressure can all lead to different relationships between a glacier and its bed. If the rock is easily deformable, then till at the bed of the glacier can be the weakest link relating to the system's flow. If there is water in the system, the water acts as a lubricant that reduces the coefficient of friction at the bed, causing the ice to slide (Bindschadler 1983; Raymond et al. 2001). With water, there can also be fluid between the grain boundaries assisting in deformation (Duval 1977). If the bed is hard, climate is cold, and geothermal heat flux is low, then a glacier can freeze to the hard bed and cause the ice to take up all of the deformation instead of the surrounding environment. Depending on how much water reaches the lateral margins and bed of the glacier, the ice can exhibit different velocity patterns; in a frozen-bed scenario, the velocity gradients often extend into the ice, whereas in a wet-bed scenario, the velocity gradient concentrates at the margin or bed (Figure 1.3).

While ice flow is possible because of gravitational driving stresses, much of the flow can be resisted by the lateral margin of the ice body (Raymond et al. 2001). While lateral margins and beds may have similar properties, the importance of lateral margins is that they are adding an additional dimension to the effects on flow: instead of just looking at deformation from the bottom of the ice, we are now looking at deformation from three sides. Since oriented fabrics, increased temperatures and slip can change the behavior of ice in these regions, correct parameterization of the lateral margins in glacier models has the potential to change the predicted outcome of the whole glacier. Including margins in mechanical models allows us to better quantify how much these parameters change flow in a natural setting.

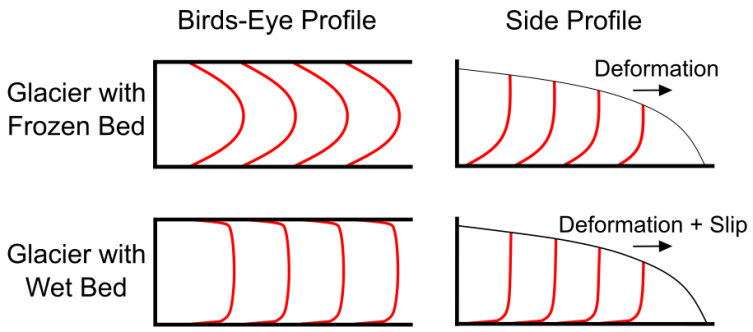

Figure 1.3: Flow patterns in ice. When glaciers have frozen beds, their flow is from internal deformation. For ice with a wet bed, flow is from both internal deformation and sliding.

1.5 Flow Laws

Historically, Glen's Flow Law has been the dominant flow relationship for many glaciologists:

$$\dot{\varepsilon} = (A * e^{-\frac{Q}{RT}}) * \sigma^{n} \quad (1)$$

where σ is stress, $\dot{\varepsilon}$ is strain rate, n is a constant, A is a material parameter, Q is the activation energy, R is the gas constant, and T is temperature (Glen 1955). A and Q both vary based on the temperature placed in the equation (Mellor and Testa 1969; Goldsby and Kohlstedt 2001), usually by an order of magnitude for A and double for Q between -20˚C and 0˚C (Cuffey and Paterson 2010). This leads to a softening of the ice with increased temperatures. Other parameters to include in this flow law are grain size, water content, impurities and deformation type (Goldsby and Kohlstedt 2001), however those factors are not considered in this project. Instead, I focus exclusively on temperature and fabric to create an in-depth sensitivity analysis specifically for those two parameters.

Glen's Flow Law is generalized to isotropic ice where there is little strain (Budd et al. 2013). To make this truer to actual ice bodies, scientists often apply enhancement factors to the

equations to conform the isotropic ice of the flow law to natural ice, as concentrated fabrics can vary deformation by an order of magnitude (Pimienta et al. 1987). Data collection has been plentiful at the divides of ice sheets and the flow lines of ice streams and glaciers (Haefeli 1952; Colbeck and Evans 1973; Gow and Williamson 1976; Hooke 1981; Herron and Langway 1982; Pimienta et al. 1987; Lipenkov et al. 1989; Thorsteinsson et al. 1997; Wang et al. 2002), so when scientists are choosing an enhancement factor, they are often based on these locations. However, a single factor cannot represent flow changes throughout the whole ice body (Alley 1992; Graham et al. 2017).

Navier-Stokes equations are another way to calculate the movement of the ice as a viscous fluid:

$$\Delta\rho \frac{\partial v}{\partial t} = \nabla P + \Delta\rho g - \mu\nabla^2 v \quad (2)$$

where ρ is density, v is velocity, t is time, P is pressure, g is gravity, and μ is the viscosity. Navier-Stokes equations can be more accurate than Glen's Flow because of the attention to viscosity, but this of course becomes difficult to model when we're talking about non-Newtonian fluids like ice. Once you add boundaries to the system where stresses can vary by orders of magnitude as the ice interacts not just with itself but also the surrounding bedrock, modeling accuracy decreases (Vaughan and Arthern 2007). The solution to this has, like Glen's Flow Law, been to assume enhancement factors or linear relationships to the viscosity, forcing rheological properties to the ice based on either what we expect would occur there or simplified versions of reality (Zwinger et al. 2007). Given these issues with Glen's flow law and Navier-Stokes equations, we needed a new solution to accurately model the viscosity of flowing ice based on its rheological properties. Scientists working with the modeling software Elmer/Ice came forward with a solution in the early 2000's (Gillet-Chaulet et al. 2005; Gillet-Chaulet 2006), which is

elaborated on in the next chapter and is the basis for my modeling. With this anisotropy-based solution and specific properties applied to the lateral margin of a mountain glacier I attempt to answer the question: how much do the temperature and fabric of lateral margins effect glacial flow?

CHAPTER 2

MODELING METHODS

2.1 Current Models

The numerical modeling of ice began with individual properties, like fabric, and was useful in comparing observations in ice cores to experimental results (Azuma and Higashi 1985; Alley 1988). Azuma and Higashi modeled fabric rotation under strain and then compared their simulations to Greenland ice cores (Azuma and Higashi 1985). Alley then went to model different types of flow and the subsequent fabrics that can form, relating it back to polar ice sheets (Alley 1988). With increased computing power in the following decades, numerical modeling has taken a turn to the macro: the scientific community now often looks beyond specific properties and instead to the flow of the whole ice body. Those ice bodies include ice sheets (Seddik et al. 2012), domes (Seddik et al. 2011; Passalacqua et al. 2016), ice streams (Payne et al. 2004; Haseloff et al. 2018), and mountain glaciers (Zwinger et al. 2007; Zhao et al. 2014; Collao-barrios et al. 2018). These models are certainly valuable, but they all neglect the smaller-scale properties that began ice modeling.

Two commonly used methods of modeling ice bodies are Shallow Ice Approximation (SIA) and full-Stokes. SIA, a zero-order model that is mainly applied to ice sheets, is computationally inexpensive but neglects much of the stress tensor and is therefore less accurate for situations with rough bedrock, steep slopes, or with lateral shearing (Le Meur et al. 2004; Zhao et al. 2014). Because SIA assumes the ice body has no longitudinal strain (fabric is vertically oriented and there are no bedrock interactions), as soon as the ice deviates from that assumption, flow does not behave as predicted in the flow laws used. Ice streams and glaciers, therefore, require

a different approach (Azuma et al. 1985; Gillet-Chaulet et al. 2005; Hudleston 2015; Bons et al. 2018). Full-Stokes, or a model that applies all orders of Navier-Stokes, is better suited for these locations because of its attention to the stress tensor, but it is very computationally extensive and still simplifies much of the rheology, as discussed in section 1.5. A solution to these issues began forming several decades ago and requires a trip to the roots of ice modeling: the behaviors of individual grains.

In the late 90's and early 2000's, scientists looked back at the mechanics modeled in the 80's and defined ice sheets based on the smaller scale anisotropy of the grains (Gagliardini and Meyssonnier 1999; Gillet-Chaulet et al. 2005). This micro-macro approach has grown since then, carried into current literature beyond just ice sheets and static fabrics, with fabric evolution introduced in 2006 (Gillet-Chaulet 2006) and grounded ice – ice shelf interactions in 2010 (Ma et al. 2010). This anisotropic modeling method is the approach taken in this project to accurately assess and predict glacial flow at the lateral margins of an ice body and is unique in its application to a mountain glacier. While scientists have spent increasing time on the accuracy of ice sheet modeling since the mid 2000's (Gagliardini et al. 2013), mountain glaciers and their rheological properties at the lateral margins are underrepresented in the modeling literature.

2.2 A Solution to Better Predict Glacial Flow

The goal of this project is to model 3D glacial flow based on the anisotropy of ice and margin properties, so we can better understand the impact lateral margins have on glaciers. To achieve this, a combination of programs was employed: COMSOL Multiphysics (www.comsol.com) to build the geometries, MATLAB (www.mathworks.com) to assign property variation, Elmer/Ice (http://elmerice.elmerfem.org/) for the flow modeling, and ParaView

(https://www.paraview.org/) for the visualization. Some are open-sourced (Elmer/Ice and Paraview), some have copywrites (COMSOL and MATLAB), and most have graphic user interfaces, or GUIs (the only one that does not is Elmer/Ice). This combination of programs allows me to select areas of the ice body and assign specific fabrics and temperatures to those areas prior to running my geometry through Elmer/Ice (Figure 2.1).

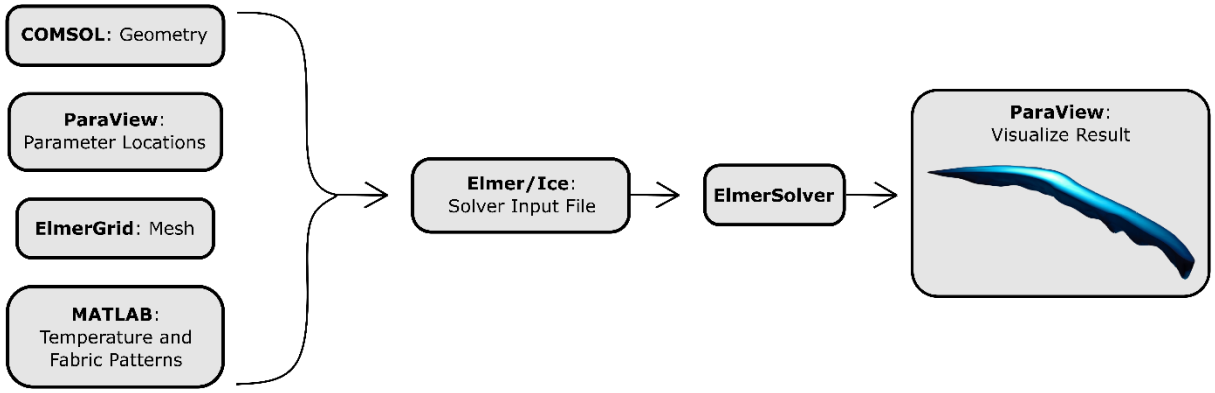

Figure 2.1: Simplified flowchart of methods. ElmerSolver produces the results which I view in ParaView. The workflow diagram in its entirety is found in Appendix A.

2.2.1 Elmer/Ice

Elmer/Ice is an open-source, full-Stokes modelling software with the capabilities of solving 3D glacier flow (elmerice.elmerfem.org). What makes Elmer/Ice unique is the ability to define the crystallographic orientation fabric of the ice (i.e. single-maximum like in Figure 1.2) using tensor notation and determine the strength of the ice according to that fabric. The anisotropic flow solver, or AIFlow, uses a general orthotropic flow law (GOLF) to determine the deformation response of ice based on crystal orientations, and therefore the viscosity of the glacier (Gillet-Chaulet et al. 2005). It first began as a linear flow law, but has since been modified to include non-linear components (Martin et al. 2009; Ma et al. 2010; Martín and Gudmundsson 2012):

$$\sum_{r=1}^{3}[\eta_r tr(M_r \cdot \dot{\varepsilon})M'_r + \eta_{r+3}(\dot{\varepsilon} \cdot M_r + M_r \cdot \dot{\varepsilon})'] = 2A\sigma_{eq}^{n-1}\sigma' \quad (3)$$

where η_r and η_{r+3} are the dimensionless anisotropic viscosities (functions of the eigenvalues of the fabric tensor), M_r is the structure tensor (a product of the eigenvectors of the fabric tensor), A is the Glen enhancement factor, and σ and $\dot{\varepsilon}$ are the stress and strain rate. To introduce the non-linearity (i.e. non-Newtonian nature) of the model, viscosity is altered based on the strain rate:

$$\eta_0 = \frac{1}{2} A^{-\frac{1}{n}} (D^2)^{\frac{1-n}{2n}} \tag{4}$$

where D is the strain rate tensor, n is the rheological index, and all other parameters are as listed above (Martin et al. 2009). When the ice is isotropic, this law defaults back to Glen's Flow Law (Montagnat et al. 2014) (Equation 1), as that is the condition under which Glen's Flow Law is based.

AIFlow defines fabric orientation by six numbers in symmetric tensor notation, with the diagonal acting as the orthogonal fabric intensity (the eigenvalues, always summing to 1), and the rest orienting the fabric reference frame (Equation 5). Fabric 1 in the tensor describes the x component of the orientation, Fabric 2 the y component, and 1 – (Fabric 1 + Fabric 2) the z component. For an example fabric, a purely isotropic glacier would have equivalent values for all three diagonals (all one third, or 0.333) and would have no need of a reference frame rotation because of the fabric's isotropy. Single-maximum fabrics have an eigenvalue close to 1 in the direction of the maximum and girdles have eigenvalues close to 0.5 for the two directions of the girdle's plane. This fabric tensor is then used in Elmer/Ice to determine the direction-dependent viscosity throughout the glacier (Gillet-Chaulet et al. 2005), as described in Equation 3.

$$\begin{bmatrix} Fabric\ 1 & Fabric\ 3 & Fabric\ 5 \\ . & Fabric\ 2 & Fabric\ 4 \\ . & . & 1 - (Fabric\ 1 + Fabric\ 2) \end{bmatrix} \tag{5}$$

2.2.2 Geometries

The three geometries of this project range from simple to complex: the simplest tests the program and results while the more complex models test realistic shapes with rough beds and curves (Figure 2.2). The two complex models incorporate bed elevation data from Jarvis Glacier, Alaska, the case-study glacier used in this project. Jarvis has a 90˚ curve at the head of the glacier, which I straightened out in one of the geometries and left in the other. There are many ways to create geometries usable in Elmer/Ice, including the export and conversion of a COMSOL Multiphysics software mesh. I chose this method for geometry creation for the ease at which I can import our bed data (in a text file format) into the graphic user interface, convert it to a solid form and mesh it with a user-chosen grid size. The first geometry, similar to half a cylinder, is 8 km long, 550 m wide and 330 m deep. This simple geometry tested the program capabilities and initial sensitivities. The second one, a "straightened Jarvis", uses the coordinates and elevation of Jarvis's bed, but without Jarvis's characteristic curve, to act as an intermediate between the first and last geometries. The final geometry has Jarvis's bed data, as is (Figure 2.3). There is some variation in these last two files, due to COMSOL's interpolation of the points. In both of these glaciers the depth is greater than in the true Jarvis so the bed files could be converted to the base of a 3D solid; if a complex bed is too close to the surface, COMSOL is unable to accept it as part of the shape. I exported these geometries as COMSOL mesh files, and then converted them into a format readable by ElmerSolver, using ElmerGrid. This conversion provides a mesh based on a series of points, or nodes, each with x, y and z coordinates and a specific node number. Throughout this project, directions are referenced as longitudinal, transverse and vertical (Figure 2.4). This wording especially comes into play when discussing single-maximum fabrics and their respective orientations, as addressed in chapters 3 and 4.

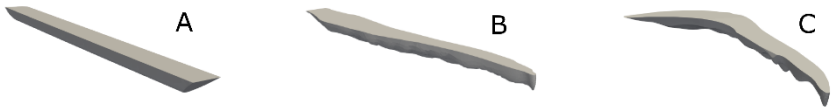

Figure 2.2: The three geometries used in the model. A) the half-cylinder, B) the straightened Jarvis glacier, and C) Jarvis.

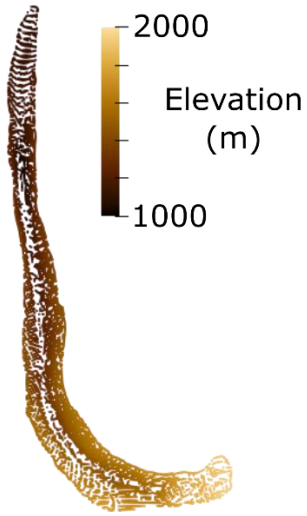

Figure 2.3: Bed elevation of Jarvis. Each node (represented here with points) in the glacier has Easting, Northing and elevation-based coordinate points.

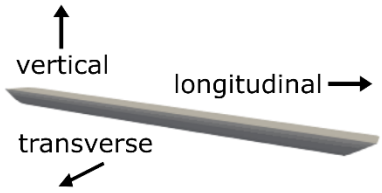

Figure 2.4: Axis directions referenced in this project. Vertical is based on the elevation and depth, longitudinal is along the length of the glacier and transverse is across the width of the glacier.

2.2.3 Components of a Solver Input File

A Solver Input File, or .sif, is the code that goes into ElmerSolver to produce results. This file includes temperature, fabric and boundary conditions, as well as computational parameters. All inputs to this model (including geometry) feed through Solvers, or the equations that define

what the program will calculate, such as 3D velocities, stress and strain rate. AIFlow is the Solver that incorporates the anisotropy of ice into flow calculations. Carlos Martín at the British Antarctic Survey and I created two other Solvers for this project, InitializeFabricWithNumberOfNode and InitializeTempWithNumberOfNode. Both Solvers assign fabric or temperature values to individual nodes within the geometry, thereby allowing me to choose specific locations for a fabric to exist, like the 10 m of ice closest to the boundary of the glacier.

To assign fabric or temperature to the glacier, I create a table in MATLAB with the node number in the first column and any wanted parameters in the following columns. For example, if I want a single-maximum fabric in all the ice 100 m from the boundary, I select all the nodes residing within that border and assign the single-maximum fabric to those nodes while assigning a different fabric to the rest of the nodes in the ice body. The Solver reads this table as it initializes, and the fabric patterns are brought into the Solver Input File.

2.2.4 Visualization of Outputs

ParaView, an open-source visualization software views the results and extracts data from the 3D flow model. For easy comparison of flow through the glacier, I slice each geometry at a transect in the upper third of the body (Figure 2.5). Measured output variables are velocity (m/a), stress (MPa) and strain rate (a^{-1}), and are represented in blues, purples and reds (Figure 2.6). When I mention ice flux (m^3/a) in my results, it is the yearly flow through the slice, integrated from the 3D velocity magnitude using ParaView's IntegrateVariables function.

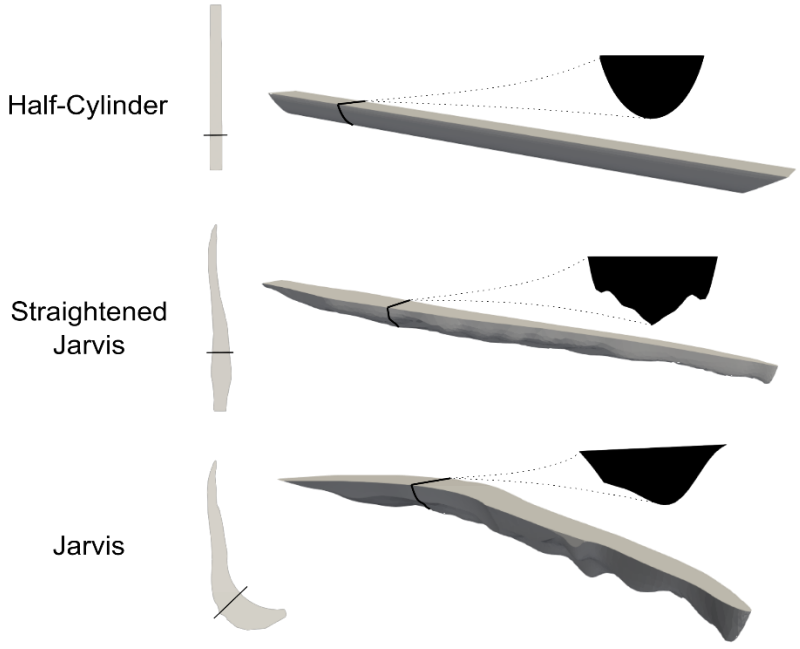

Figure 2.5: The three geometries and transect slices. Slices are at 7040000 Northing, the field site on our case-study glacier, Jarvis. All three geometries flow north. The surface slope visible in the Jarvis slice is due to the 45˚ angle at which the slice is cut to keep it perpendicular to the margin; the western edge is at a higher elevation than the eastern edge in this transect.

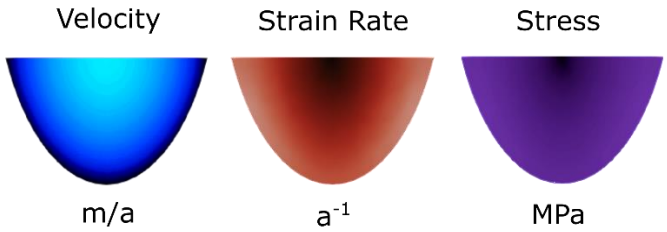

Figure 2.6: Variables measured and visualized in ParaView. Colors continue throughout this project: velocity magnitude is blue, the effective strain rate (second invariant of the strain rate tensor) is red, and the effective stress (second invariant of the stress tensor) is purple.

CHAPTER 3

SYNTHETIC MODEL RESULTS

3.1 Model Sensitivities

Elmer/Ice solves the 3D flow of the three geometries (Figure 2.5) with various temperature and fabric patterns. Through the development of the node solvers mentioned above, I tested several parameters to determine sensitivity of the model to variations in each run. The mesh grid size and the tabulated viscosity files are both building blocks of the model rather than being a specific ice condition. These can provide a significant flux increase when varied (Figure 3.1) but were kept the same in all following sections of this project to avoid this variation. Parameters relating to the ice itself, such as the number of crystals in a sample and the concentration and distribution of the fabric (cone angles and characteristic angles), can increase ice flux by five times the lowest value (Figure 3.1). I explain details of the model sensitivity to each of these five variables below in the following sections.

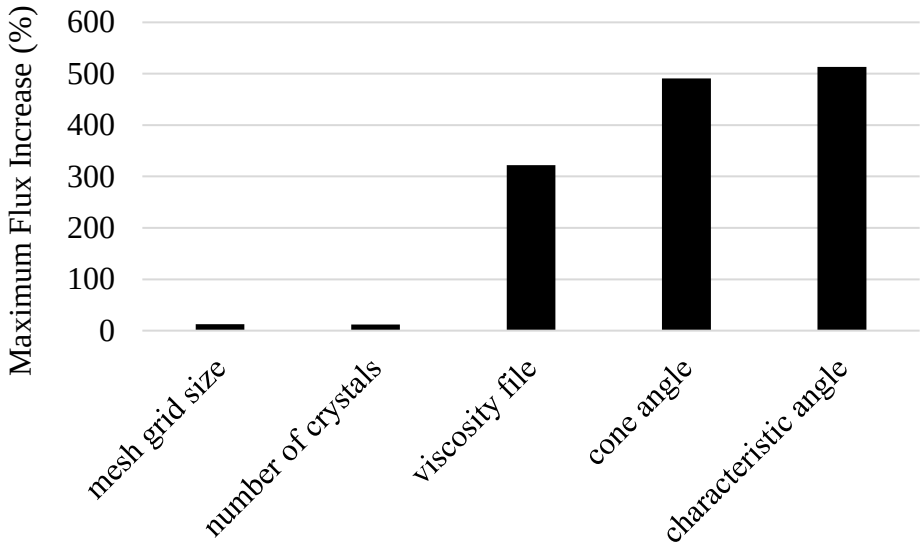

Figure 3.1: Model sensitivities based on five variables. Each of these variables is explained in detail below.

3.1.1 Mesh Grid Size

The smaller the distance between the points in the mesh, the slower the calculated flow velocity. When the Jarvis geometry runs with a grid size up to 300 m, flux was, on average, 8% greater than when the geometry runs with a grid size up to 50 m (sizes are specified in COMSOL when creating the mesh). I use the smaller grid to accommodate for specialized fabric patterns. The grids do decrease in size around corners and bedrock bumps, where it is important to refine 3D flow, so the minimum length between points is 10 m, and the maximum length is 50 m (Figure 3.2).

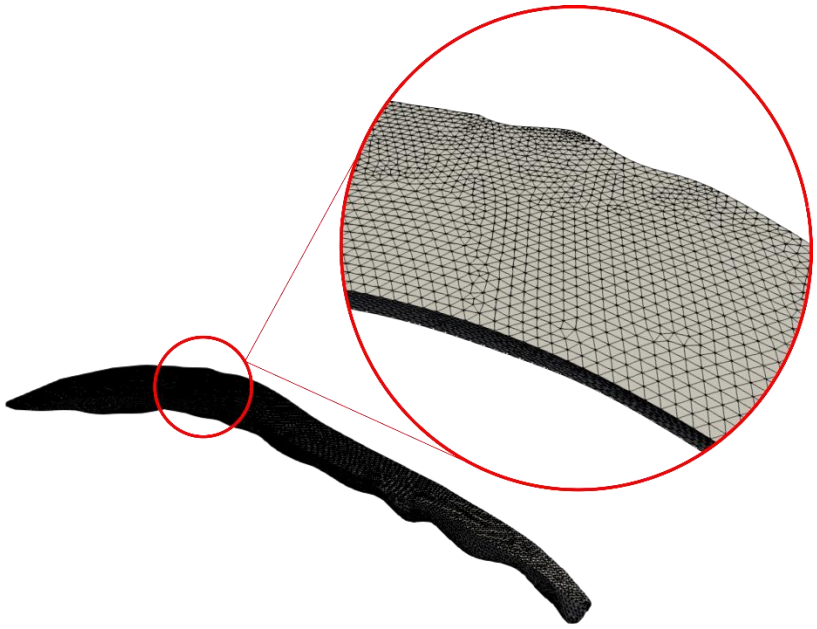

Figure 3.2: Mesh cells of the Jarvis geometry. Each intersection is a node with x, y and z coordinates.

3.1.2 Number of Crystals

Variation in fabric, and thus flow, increases when the number of crystals in a sample decreases because the orientation of an outlier is more likely to skew the average. If an outlier is present, the Fabric values (the tensor shown in Equation 5) change and can cause overall fabric to be more or less favorable to flow. In isotropic fabrics, this variation in flow stays under 5% unless

there are only 10 c-axis points (also known as grains or crystals) to sample from (Table 3.1). This corroborates with what Gillet-Chaulet, *et al*. (2005) discovered when they were testing response of the flow law used in this project (Equation 3): there needs to be at least twelve grains in a sample to accurately define the viscosity of an isotropic fabric. To minimize variation from flow in generated fabrics below even 5%, all synthetic fabrics in this project have 1000 points, unless otherwise specified. This reduces flux variation to 0.01%, ensuring that when I define isotropic and anisotropic fabrics in multiple model runs, they are indeed the same fabric.

Fabric	Number of Points	Variation in Flux (%)	Variation in Maximum Velocity (%)
Isotropic	10	6.15	6.52
	50	1.41	1.78
	100	3.74	4.50
Longitudinal single-maximum (10˚ angle)	10	7.96	9.99
	50	8.78	11.68
	100	1.92	2.53
Longitudinal single-maximum (30˚ angle)	10	10.27	10.35
	50	5.52	7.20
	100	5.86	7.17

Table 3.1: Analysis of the variation in flow due to the number of fabric points used to define a fabric. I calculated percentages between the smallest and largest flow values for each case, between the three runs completed for each fabric's set number of points. The longitudinal single-maximum shown here represents an anisotropic fabric end-member because of its production of high flow values. I ran these single-maximum fabrics both in concentrated (10˚ cone angle) and broader (30˚ cone angle) forms.

3.1.3 Tabulated Viscosity Files

Tabulated viscosity files determine how dependent flow is on the fabric of the ice based on a series of parameters, like grain anisotropy and the stress exponent, and are brought into this project's flow equation in η_r (Equation 4). Elmer/Ice's website (elmerfem.org/elmerice) provides fifty-one viscosity files for the user, with different anisotropy parameter combinations in each. I ran all fifty-one viscosity files on the simplest geometry with a frozen bed and show representative files below (Figure 3.3). Variation is only high with oriented fabrics. With isotropic fabrics, the

difference in maximum velocities between the runs is $4x10^{-5}$ m/a. The file chosen for all subsequent runs in this project provides a velocity close to the average velocity of all the tabulated viscosity files and has grain anisotropy parameters equal to 0.04 (β) and 1.0 (γ), and a stress exponent equal to 1. Beta and gamma are determined by the following ratios:

$$\beta = \frac{shear\ viscosity\ parallel\ to\ the\ basal\ plane}{shear\ viscosity\ in\ the\ basal\ plane} \quad (6)$$

$$\gamma = \frac{viscosity\ in\ compression\ or\ tension\ along\ the\ c\ axis}{viscosity\ in\ compression\ or\ tension\ along\ the\ basal\ plane} \quad (7)$$

as described in the equations for the GOLF model (Gillet-Chaulet et al. 2005).

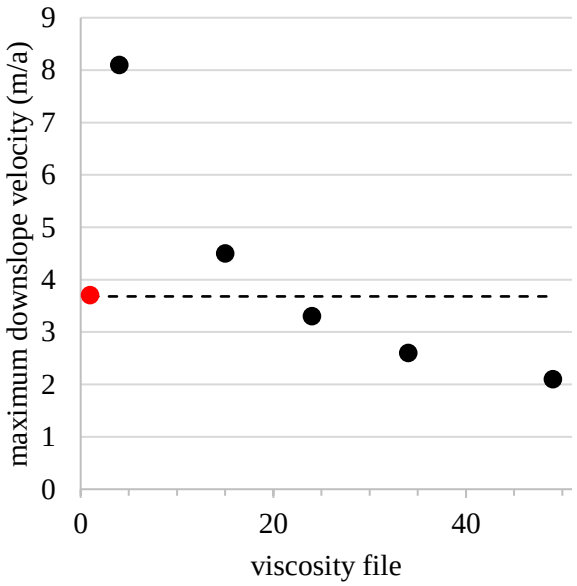

Figure 3.3: Velocity from six representative tabulated viscosity files. The Elmer/Ice website provides 51 file options. The dotted line is the average of all runs and the red dot is the file used for this project. These runs have a longitudinal single-maximum fabric and a frozen bed. Data on files is in Appendix A.

3.1.4 Cone Angle of Fabrics

As the distribution, or cone angle, of the fabric spreads from a concentrated pattern to isotropic, flux changes accordingly, but not in a linear fashion (Figure 3.4). As expected, longitudinal single-maximum fabrics have the greatest velocity change with increasing cone angles

because they have the highest velocities with concentrated fabric. All fabrics with some component of a longitudinal single-maximum have higher velocities, like girdles in x-z and x-y planes. Single-maximum fabrics in the z direction have a slower flux than an isotropic fabric because they have no component of longitudinal fabric. All data are from the simplest geometry with a frozen bed.

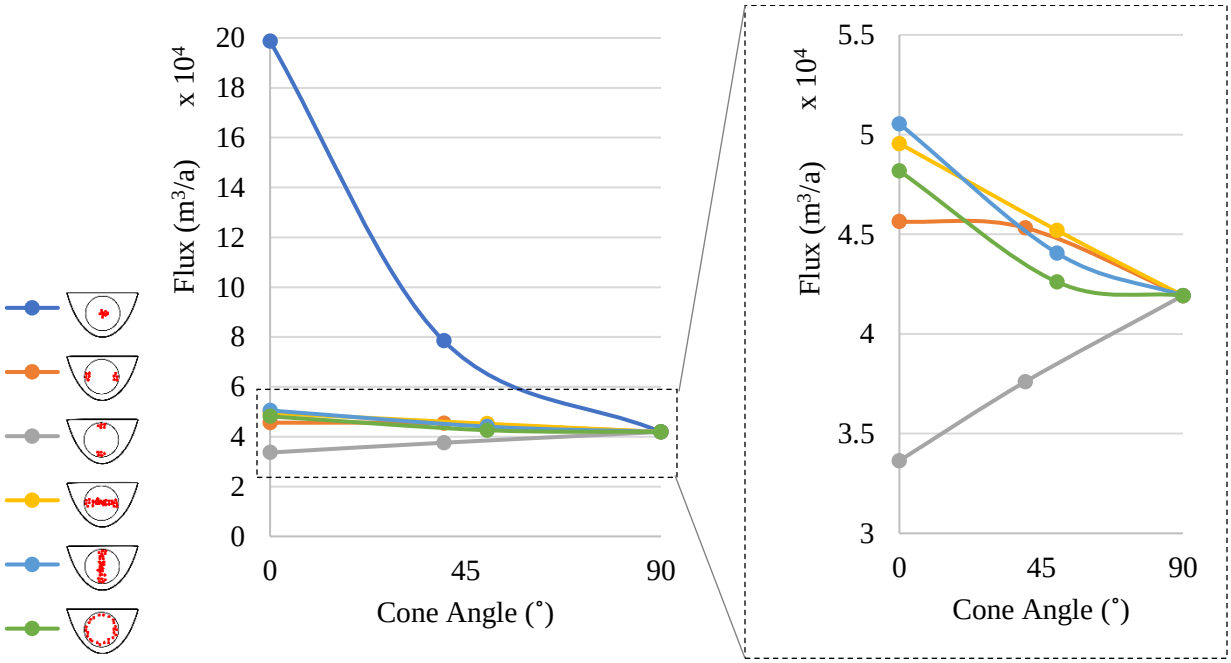

Figure 3.4: Flux versus the cone angle of the fabric. I varied the cone angle of the fabric, or band width of fabric distribution, in each of the six major fabric patterns. Fabric from top down in the key are: longitudinal single-maximum (x direction), transverse single-maximum (y direction), vertical single-maximum (z direction), girdle in the x-y plane, girdle in the x-z plane and girdle in the y-z plane. These coresond to the fabric patterns at 0˚. Each fabric becomes less concentrated until they reach an isotropic fabric (90˚). All were run in the simplest geometry with non-slipping boundary conditions.

3.1.5 Angle of Fabric Axes

To assess the flux of fabrics with angles off the x, y and z axes, the characteristic angle of fabrics was varied between the six major fabric patterns (Figure 3.5). Like cone angle, flux varies most when the characteristic angle of the fabric has some component of a longitudinal single-

maximum, however to create a more extreme flux change, the characteristic angle must be within 45˚ of the longitudinal single-maximum.

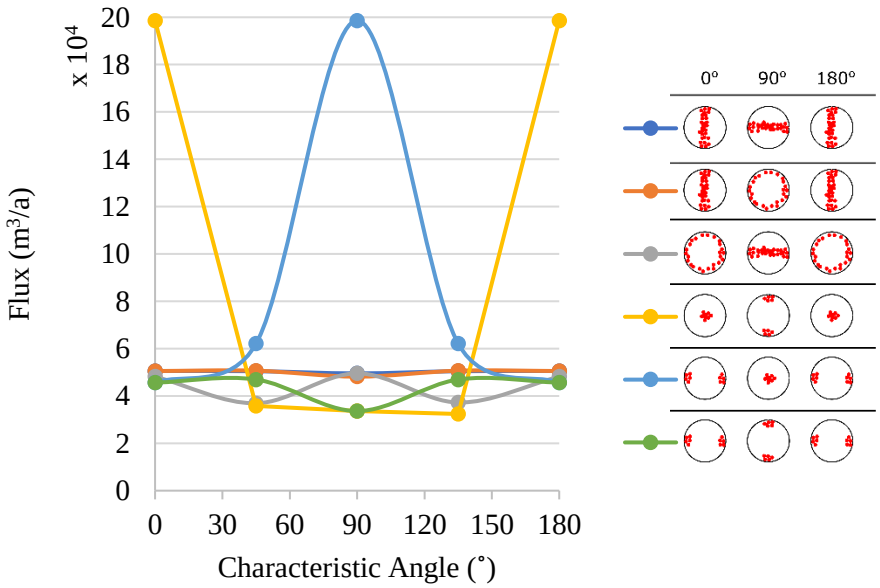

Figure 3.5: Flux versus characteristic angle. Each of the six major fabrics rotate toward a different x, y, z axis or plane. Fabrics begin at a specific axis or plane (first column in key) and then rotate 45˚ toward the axis or plane in the second column of the key. The third point on each line of the graph is the fabric at that new axis or plane (second column in the key), and the fourth and fifth points are the fabric rotating back to the original orientation. These runs have the half-cylinder geometry and non-slipping boundary conditions.

3.2 Changing Fabrics, Temperatures and Slip Conditions

To test the sensitivity of my model further, I completed reference runs with fabrics and temperatures assigned over the whole ice body. I set these parameters to the extreme to determine end-members for the rest of the sensitivity analysis. At these extremes, fabric provided the greatest variation in flow, and a single-maximum fabric at 0˚C flowed the fastest, as expected (Figure 3.6).

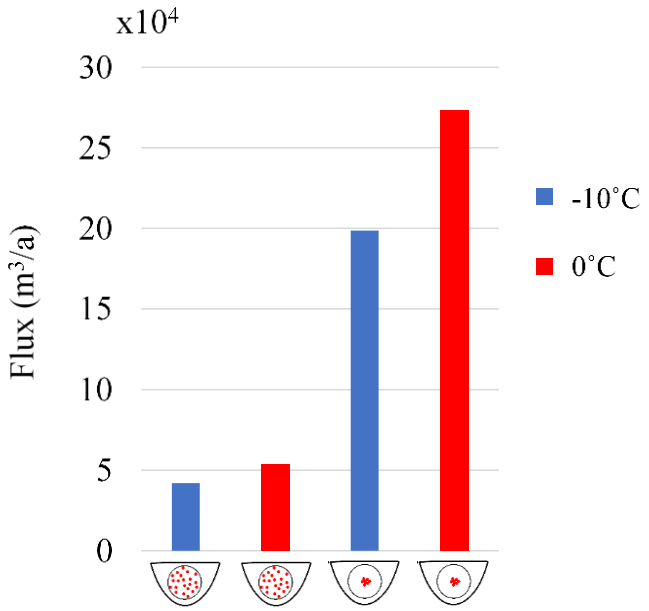

Figure 3.6: Flux based on fabric and temperature. Data from the half-cylinder with a frozen bed. The first two columns are isotropic and the second two are single-maximum. Color corresponds to temperature.

3.2.1 Fabric

Single-maximum fabrics in this project are longitudinal (x), transverse (y) and vertical (z), unless otherwise specified. Girdle fabrics exist in the planes of these directions: x-y, x-z and y-z. I ran these fabrics in all geometries and show the flux results of the half-cylinder below (Figure 3.7). Single-maximum fabrics have the starkest contrast between their orientations, with an order of magnitude difference between a single maximum in the z (vertical) direction and in the x (longitudinal) direction.

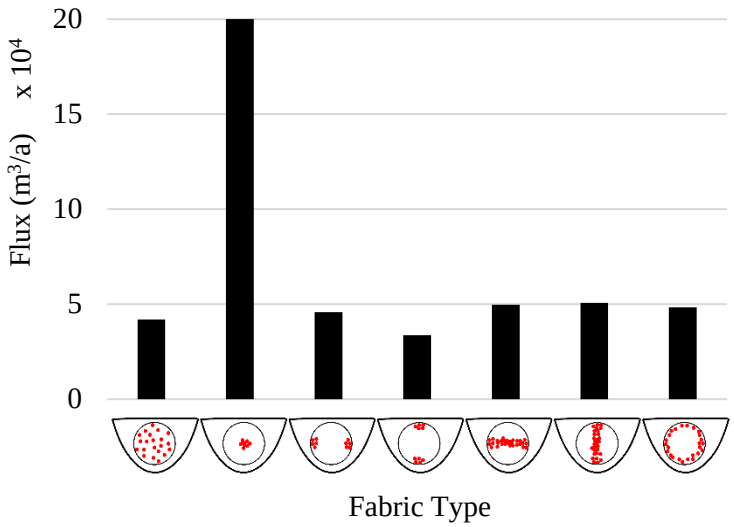

Figure 3.7: The seven general fabric patterns used in this study. These are extreme cases for a natural scenario to provide end-members for the sensitivity tests. From left to right, the fabrics are isotropic, longitudinal single-maximum (oriented to the x-axis), transverse single-maximum (oriented to the y-axis), vertical single-maximum (oriented to the z-axis), an x-y girdle, an x-z girdle and a y-z girdle.

Strain rates are highly dependent on glacier processes and ice body type. Shear strain rates measured on a Swiss Alps glacier moving 35 m/a (half of which was from deformation and half was from sliding) were found to be 10^{-1} a^{-1} (Gerrard et al. 1952). In Alaska, glaciers have been measured with surface strain rates between 10^{-3} a^{-1} (Warner and Cloud 1974) and 10^{-1} a^{-1} (Wu and Christensen 1964). In the Greenland Ice Sheet, surface strain rates are 10^{-5} a^{-1} (Wang et al. 2002). In my model, I found strain rates close to the lower bound of those found in Alaska, around 10^{-3} a^{-1} (Figure 3.8). In this frozen bed scenario, strain rates are highest along the lateral margins, as expected.

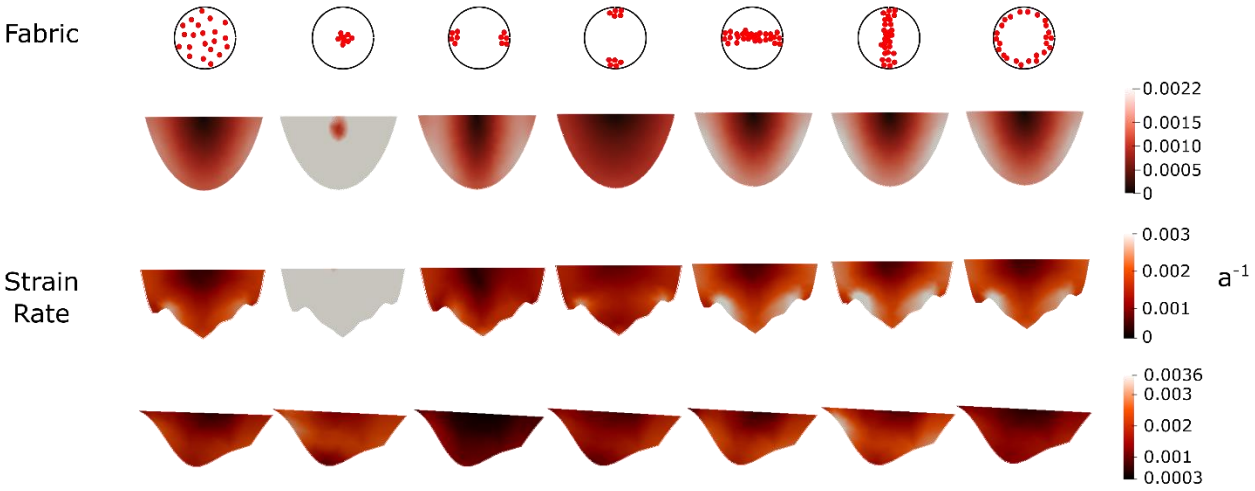

Figure 3.8: Effective strain rates of the non-slipping models. Views through the slices are down glacier and fabric orientations are as well. The first column is the isotropic case and following cases are a longitudinal single-maximum (x), transverse single-maximum (y), vertical single-maximum (z) and girdles in the x-y, x-z, and y-z planes respectively. In the half-cylinder, the maximum value in the longitudinal single-maximum is 0.012 a^{-1}. In the straightened Jarvis geometry, this fabric has a maximum value of 0.014 a^{-1}. Both have patterns similar to the girdles of those geometries.

3.2.2 Temperature

As expected with temperature, the warmer the ice the faster the velocity. Though a temperate glacier will rarely reach temperatures colder than -10˚C, I ran a -20˚C case for each model to see how the program treats ice with a different activation energy. Flux increases from ice temperatures at -20˚C to 0˚C for the half-cylinder, straight Jarvis and Jarvis are 64%, 72% and 76% respectively. From -10˚C to 0˚C, the flux increases are 28%, 31% and 32% respectively (Figure 3.9).

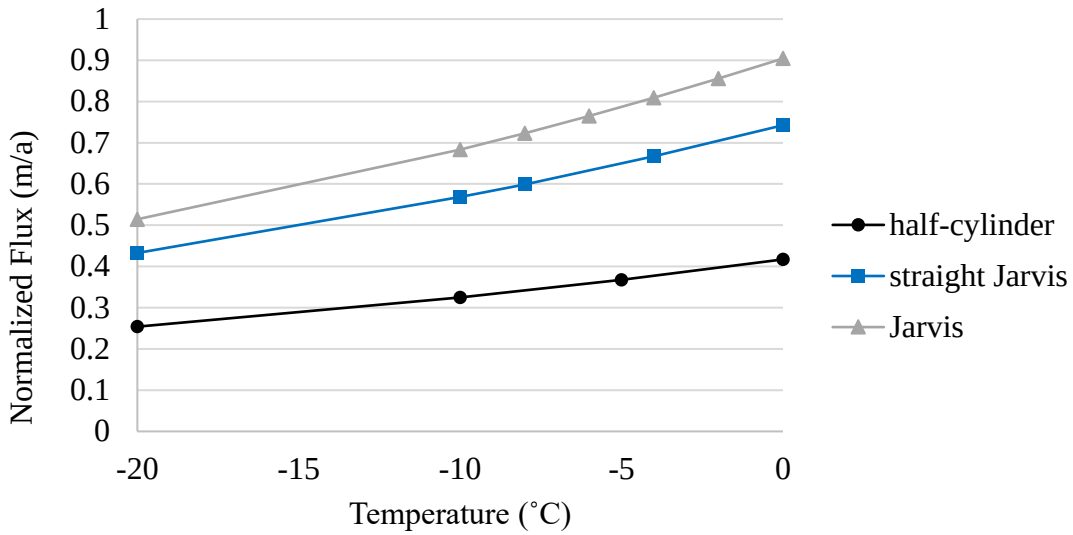

Figure 3.9: Flux versus temperature for all three geometries. All runs have an isotropic ice body between -20 and 0˚C and have non-slipping boundary conditions. Flux is normalized to slice area.

3.2.3 Slip

When using a "frozen bed" or non-slipping model, fluxes and velocities isolate the deformation component of the flow, but as there is often water at the bed involved in temperate glacier flow patterns, it is important to assess how a slipping bed changes the dynamics. To address slip in this model, the Elmer/Ice user applies a variable within the Solver Input File. When the glacier has a frozen bed, the slip coefficient is 1.0. When the ice body is temperate and would have a slipping bed, the coefficient is 0.01, a value based on the linear friction law programmed into Elmer. This friction law employs basal shear and basal velocity: the ice slides perfectly when the coefficient is 0 and doesn't slide when the coefficient goes to infinity (Gagliardini et al. 2013). For the case of this project, frozen boundary conditions exist when the slip coefficient is 1, and I apply transverse and longitudinal slip to my models but not slip normal to the bed. Allowing slip can increase flux by an order of magnitude. For the end-member fabrics (isotropic and longitudinal single-maximum) at -10˚C, flux increases by an average factor of eleven between the non-slip and

slipping runs (Figure 3.10). For isotropic end-member temperatures (-10˚C and 0˚C), the flux increases by an average factor of fourteen between the non-slip and slipping runs.

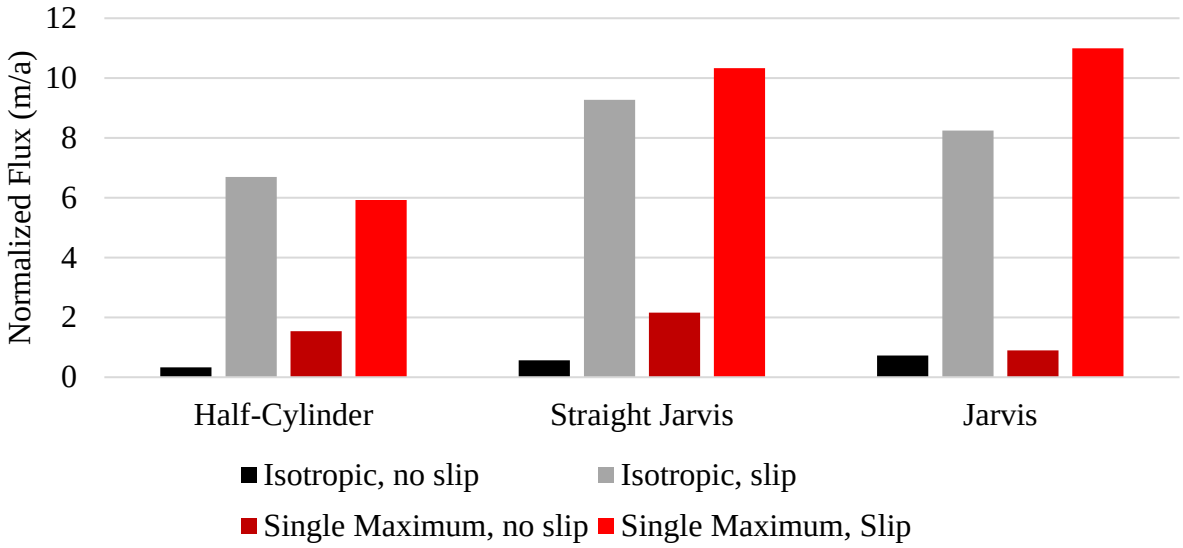

Figure 3.10: Flux for all three geometries in slipping and non-slipping cases, for isotropic and single-maximum fabrics. Black and grey are isotropic fabrics while reds are single maximum fabrics. Flux is normalized to slice area.

When I apply slip to all fabrics, the variation between the longitudinal single-maximum fabric and the rest of the fabrics (Figure 3.11) changes from the non-slip runs. Where the single-maximum fabric is clearly the fastest in the non-slip model, here the longitudinal single-maximum is the fourth fastest and is even slower than the isotropic case. The location of high strain rates is also more dependent on fabric orientation here than the runs without slip (Figure 3.12). In the half-cylinder and straightened Jarvis single-maximum fabrics, the high strain rate areas are along the basal planes of the crystals: along the lateral margins for transverse fabrics and at the bed and surface for the vertical fabrics. This is complicated in the Jarvis geometry when the curve comes in to change the interaction of fabric direction and the lateral margins, but some of this pattern is still preserved, especially in the vertical single maximum. The girdles,

which distribute the c-axes in a plane, and the isotropic case have lower strain rates in all three geometries than the single-maximums (Figure 3.12).

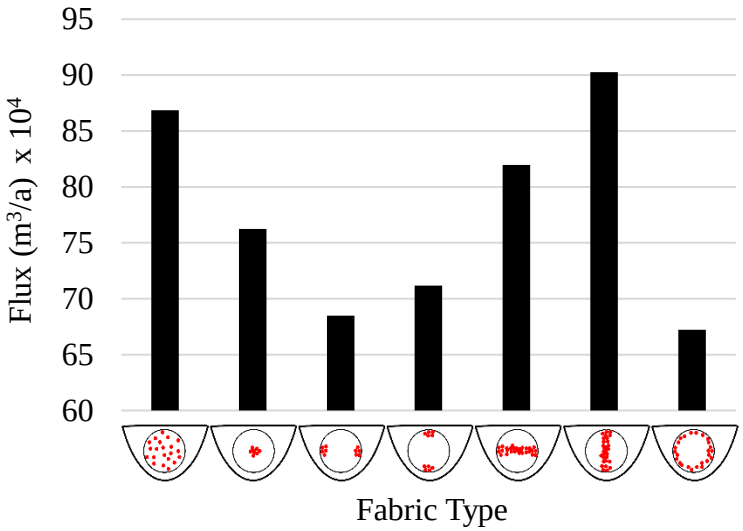

Figure 3.11: Flux versus fabric with temperate slip boundary conditions. From left to right the fabrics are isotropic, longitudinal single-maximum (x), transverse single-maximum (y), vertical single-maximum (z) and girdles in the x and y, x and z, and y and z directions.

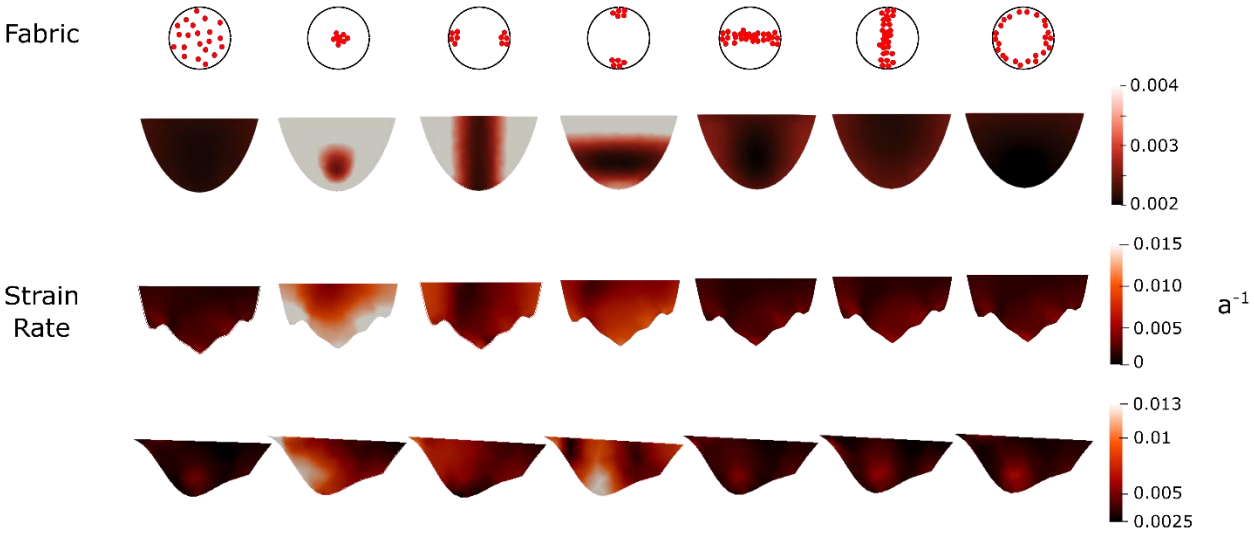

Figure 3.12: Effective strain rates of the slipping models. Views through the slices are down glacier and fabric orientations are as well. The first column is the isotropic case and following cases are a longitudinal single-maximum (x), transverse single-maximum (y), vertical single-maximum (z) and girdles in the x-y, x-z, and y-z planes respectively. In the half-cylinder, the highest strain rate recorded (above the scale shown) is 0.008 a^{-1} in the longitudinal single-maximum.

Slip can also vary based on distance from the head of the glacier (in this case, based on longitude as my geometries are south-north flowing) (Figure 3.13). In the isotropic case, when I apply a frozen bed south of the slice transect and a slipping bed north of transect, the fluxes normalized to area are 1.57, 1.85 and 1.03 m/a for the half-cylinder, straight Jarvis and Jarvis. These values are all between the isotropic slip and no-slip fluxes for each geometry.

Figure 3.13: Surface velocity with varied slip locations. The left quarter of the geometry is frozen to the bed and the right three-quarters are slipping.

3.3 Borders Along the Lateral Margins

To represent fabric along the lateral margins of the glacier, I assign an internal border to the glacier, between 10 m and 100 m (Figure 3.14). I then give this border and the center of the ice body two separate fabrics or temperatures. To provide end-member boundaries for subsequent natural-parameter tests, fabric is either isotropic or longitudinal single-maximum and temperature is either -10˚C or 0˚C.

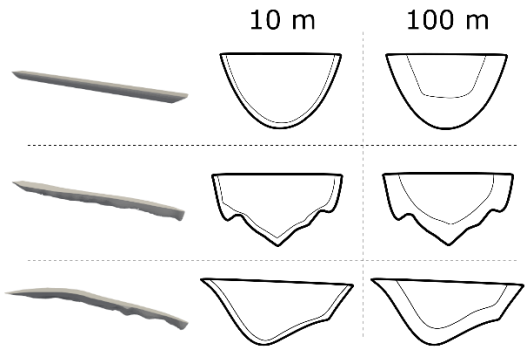

Figure 3.14: Geometries and border assignment. From top to bottom: the half-cylinder, the straitened Jarvis, and Jarvis. Slices of each geometry show a 10 m internal border and 100 m internal border.

In the fabric border model, the half-cylinder and straightened Jarvis geometries provide the largest increases in flux between the all-isotropic and all-anisotropic runs (Figure 3.15). In the straightened Jarvis, just 10 m of a longitudinal single-maximum fabric at the border of an isotropic glacier increases flux by 26%. In this geometry and the half-cylinder, there are also reductions in flux when a stiff-ice border exists on a weak-ice body, as seen around 50% area in the straightened Jarvis and between 60 and 90% area in the half-cylinder (Figure 3.15). The effect that stiff and weak-ice fabric borders have on the velocity distribution throughout the glacier is shown in Figure 3.16, with the weak ice causing the greatest increases in velocity. For these border runs, the flux measurements of the straight glaciers have steeper slopes while the curved Jarvis geometry has a more moderate slope.

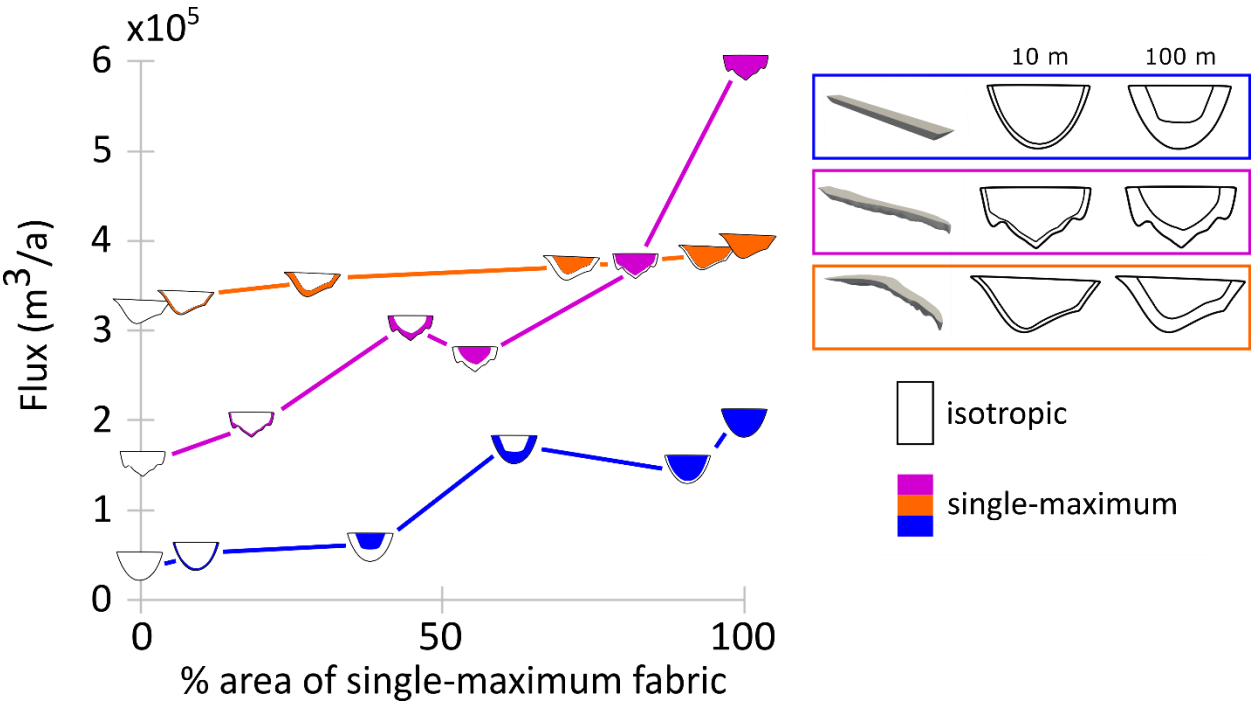

Figure 3.15: Fabric border runs without slip. The three geometries have varying amounts of isotropic and longitudinal single-maximum fabrics. The half-cylinder is reperesented in blue, the straightened Jarvis in magenta and Jarvis in orange. Differences in y-intercepts are due to geometry size differences.

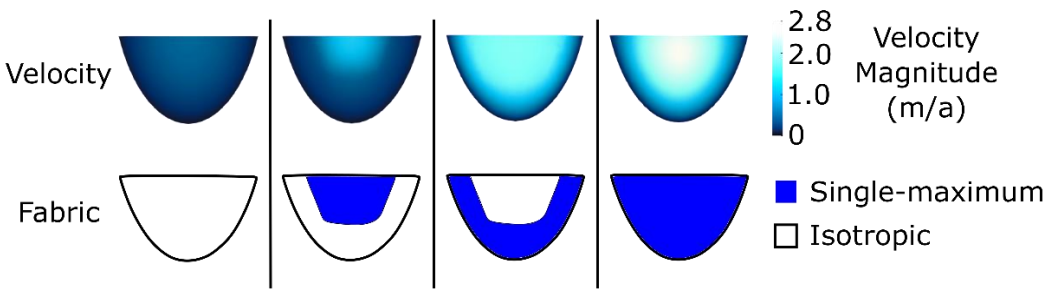

Figure 3.16: Fabric border velocity patterns in the half-cylinder. The top row is the velocity of each run in m/a and the bottom row is the fabric assigned to the glacier prior to the run. The first column is the fully isotropic case, the second the 100 m isotropic border, the third is the 100 m longitudinal single-maximum border and the final column is the fully longitudinal single-maximum case.

Changing temperatures provide similar patterns, though to a lesser extreme than that of synthetic fabrics. In the case of the straightened Jarvis geometry, the 10 m 0˚C border increases flux by 7.6%. This geometry is also the only one that shows the flux decrease when the border flips from weak ice to stiff ice, as is characteristic with the fabric border runs. However, even if the other two geometries don't clearly show this flux drop, there is still a change in slope when the border changes from weak to stiff. For example, despite an increase in the amount of warm ice in the system between the two center points in the Jarvis geometry, the flux is almost the same (Figure 3.17).

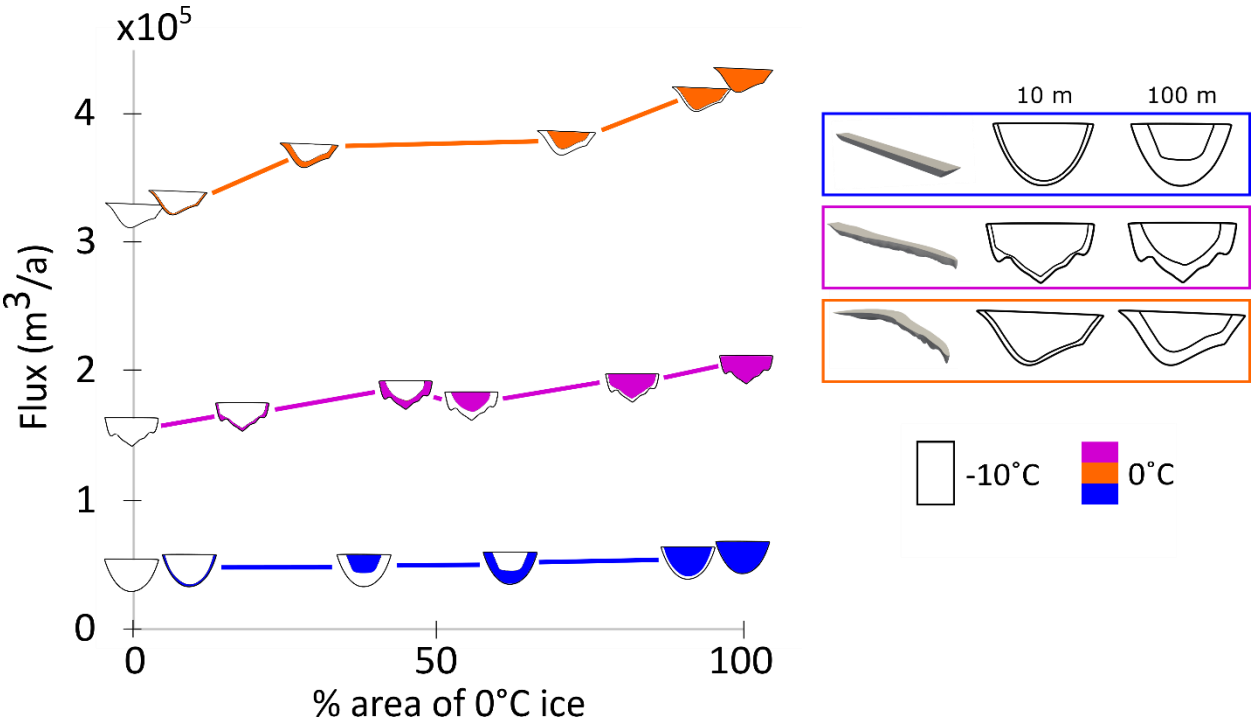

Figure 3.17: Temperature border runs without slip. The three geometries have varying amounts of cold (-10˚C) ice and warm (0˚C) ice. The half-cylinder is reperesented in blue, the straightened Jarvis in magenta and Jarvis in orange. Differences in y-intercepts are due to geometry size differences.

When slip is added to the border runs, we see a pattern with the fabric similar to the patterns in the non-slip temperature runs, but with even more of a lasting decrease in flux during the isotropic borders. The less deformable ice holds back flow in both the 100 m and 10 m border cases, not just one (Figure 3.18). Temperature borders with slip behave almost identically to those without slip, just an order of magnitude faster (Figure 3.19).

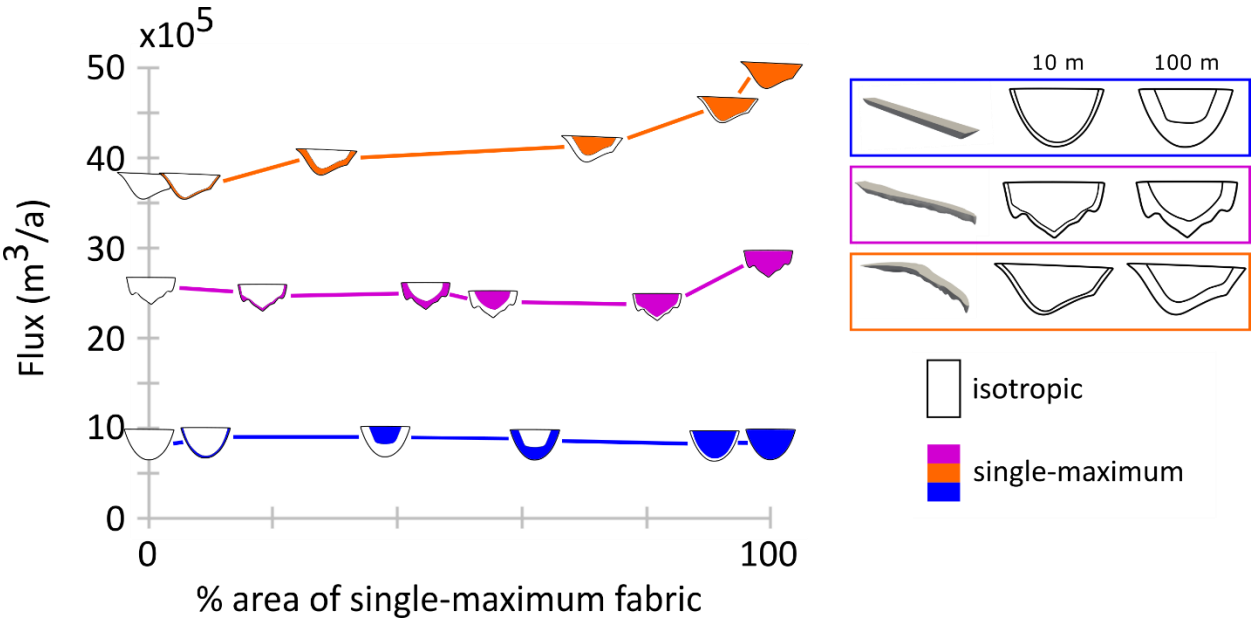

Figure 3.18: Fabric border runs with slip. The three geometries have varying amounts of isotropic and longitudinal single-maximum fabrics. The half-cylinder is reperesented in blue, the straightened Jarvis in magenta and Jarvis in orange. Differences in y-intercepts are due to geometry size differences.

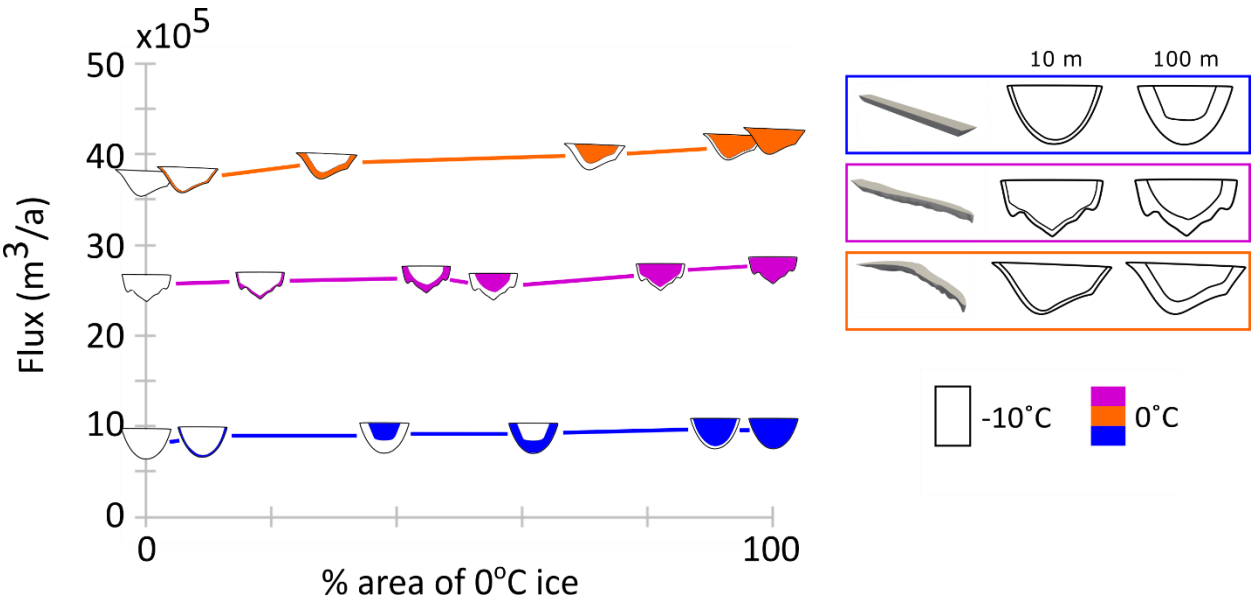

Figure 3.19: Temperature border runs with slip. The three geometries have varying amounts of cold (-10˚C) ice and warm (0˚C) ice. The half-cylinder is reperesented in blue, the straightened Jarvis in magenta and Jarvis in orange. Differences in y-intercepts are due to geometry size differences.

3.4 Rotating Fabrics

Deviatoric stresses in my model average $2x10^{-3}$ MPa. This is around one order of magnitude smaller than deviatoric stresses recorded in glaciers (Pfeffer et al. 2000), two orders of magnitude smaller than basal shear in glaciers (Cohen et al. 2005), and two orders of magnitude smaller than stresses estimated in ice sheets (Russell-Head and Budd 1979; Azuma et al. 1985). Margin glacier models in simple parabolic channels found horizontal shear to be a maximum of $6.3x10^{-2}$ MPa (Adhikari and Marshall 2012), still an order of magnitude higher than stresses in my model. These lower stresses can be attributed to the underestimation of deviatoric stresses in the AIFlow Solver, as the Solver overestimates the concentration of the c-axes along the vertical (Gillet-Chaulet et al. 2005). Despite this underestimation though, comparing the magnitudes of these stresses across the different model variations is valuable to assess fabric interaction with the bed. Effective stress (σ_e), or the second invariant of the stress tensor, represents the overall magnitude of deviatoric stresses:

$$\sigma_e = \sqrt{\sigma'^2_{xy} + \sigma'^2_{yz} + \sigma'^2_{zx} - \sigma'_{xx}\sigma'_{yy} - \sigma'_{yy}\sigma'_{zz} - \sigma'_{xx}\sigma'_{zz}} \quad (8)$$

where σ' is the deviatoric stress in the direction of the subscripts. The same equation applies when considering the second invariant of the strain rate tensor, or effective strain rate. Depending on the orientation of the fabric in each run, the effective stress is higher in different areas (Figure 3.20).

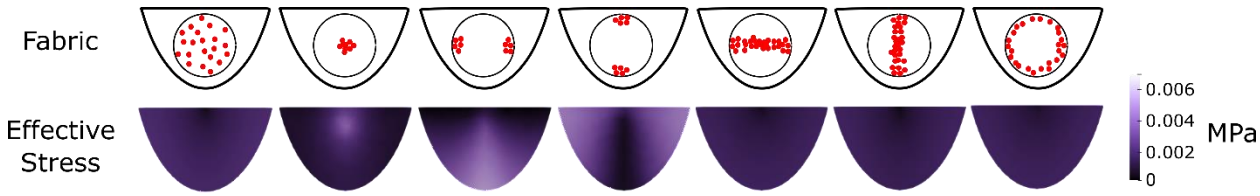

Figure 3.20: Effective stress based on fabric. Views through the slices are downglacier. The first column is the isotropic case and following cases are a longitudinal single-maximum (x), transverse single-maximum (y), vertical single-maximum (z) and girdles in the x-y, x-z, and y-z planes respectively.

The two fabric cases with the greatest effective stress are the vertical and transverse single-maximums. In the vertical single-maximum, effective stress is lowest when the fabric is close to perpendicular with the bed, and it is the same with the transverse single-maximum. When these two fabrics combine, rotating the single-maximum so it is always perpendicular with bed, an overall reduction of stress and increase in velocity occurs (Figures 3.21 to 3.24).

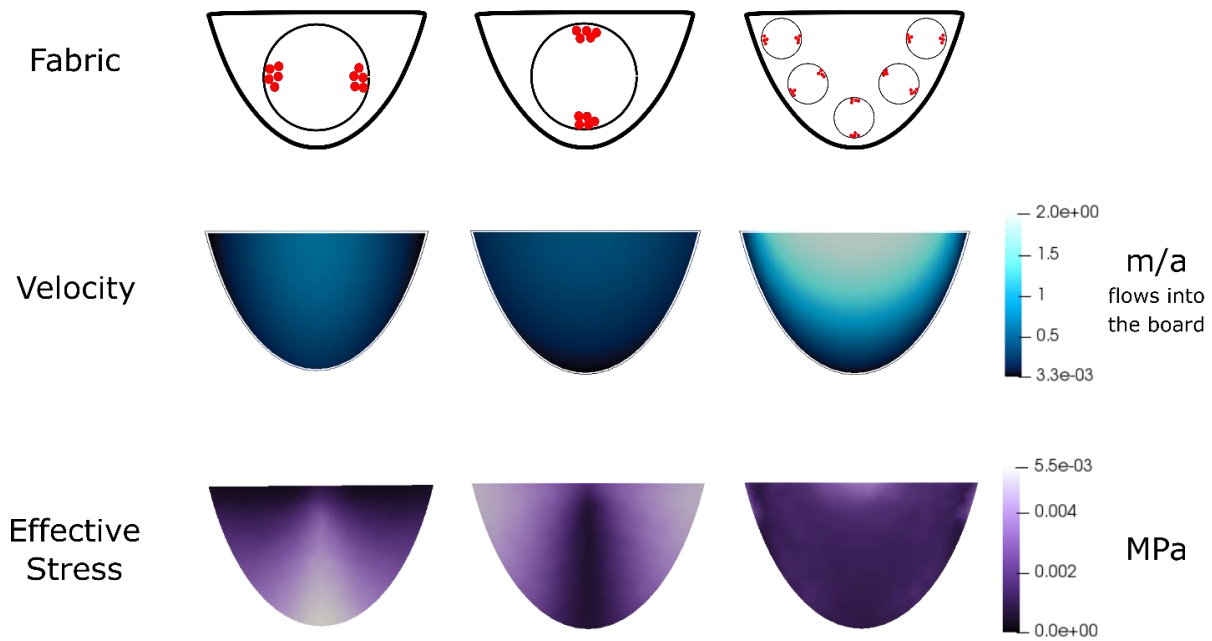

Figure 3.21: Velocity and stress based on rotating fabric in the half-cylinder. The first column is a transverse single-maximum fabric, the second a vertical single-maximum, and the third a single-maximum fabric that rotates to stay perpendicular to the bed. When the fabric rotates, stress is reduced and velocity increases.

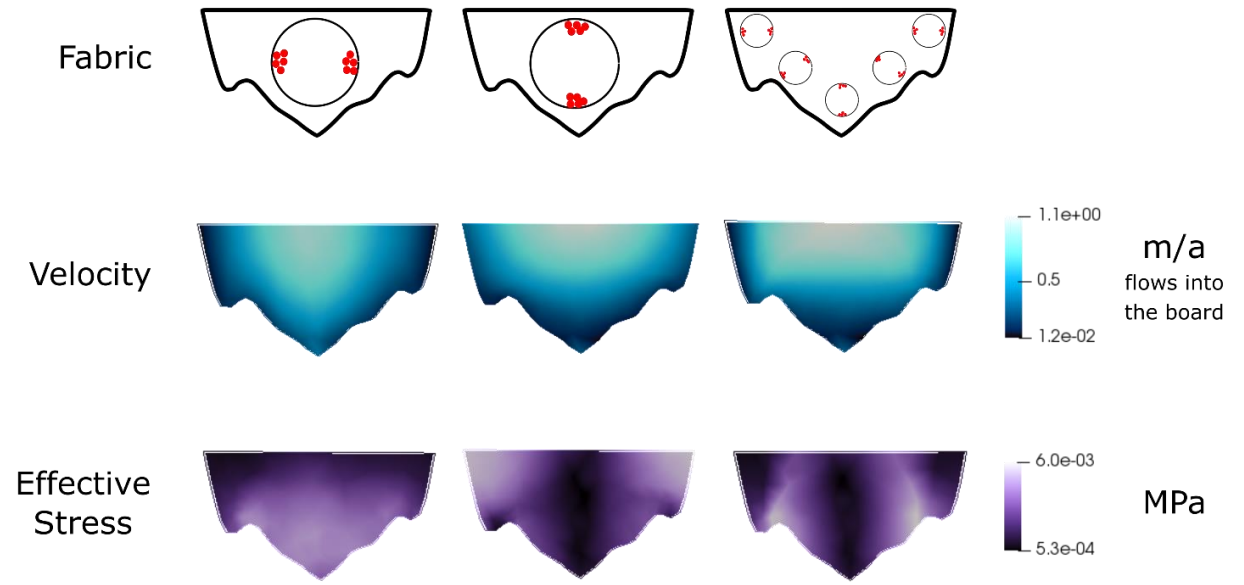

Figure 3.22: Velocity and stress based on rotating fabric in the straight Jarvis. When the fabric rotates throughout the glacier to stay perpendicular to the bed, overall stress is reduced and velocity increases, even though bed roughness still causes high stress in some locations. The first column is a transverse single-maximum, the second column a vertical single-maximum, and the third is the rotating fabric.

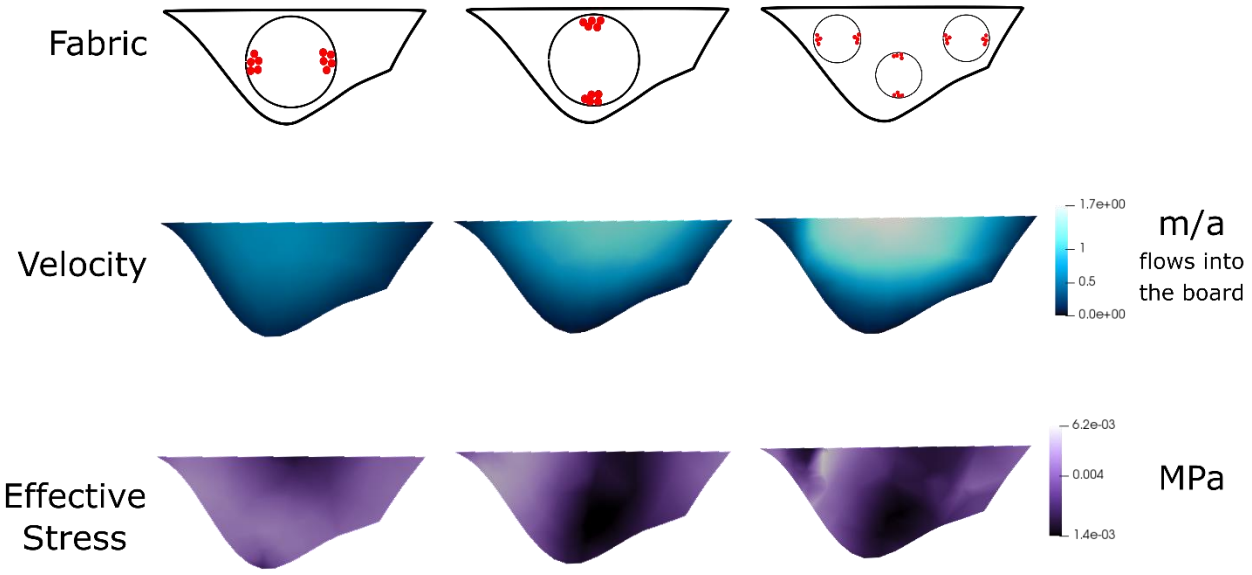

Figure 3.23: Velocity and stress based on rotating fabric in the Jarvis geometry. When the fabric is rotated throughout the glacier to be perpendicular to the bed (even around the curve), stress is reduced and velocity increases. The first column is a transverse single-maximum, the second column a vertical single-maximum, and the third is the rotating fabric.

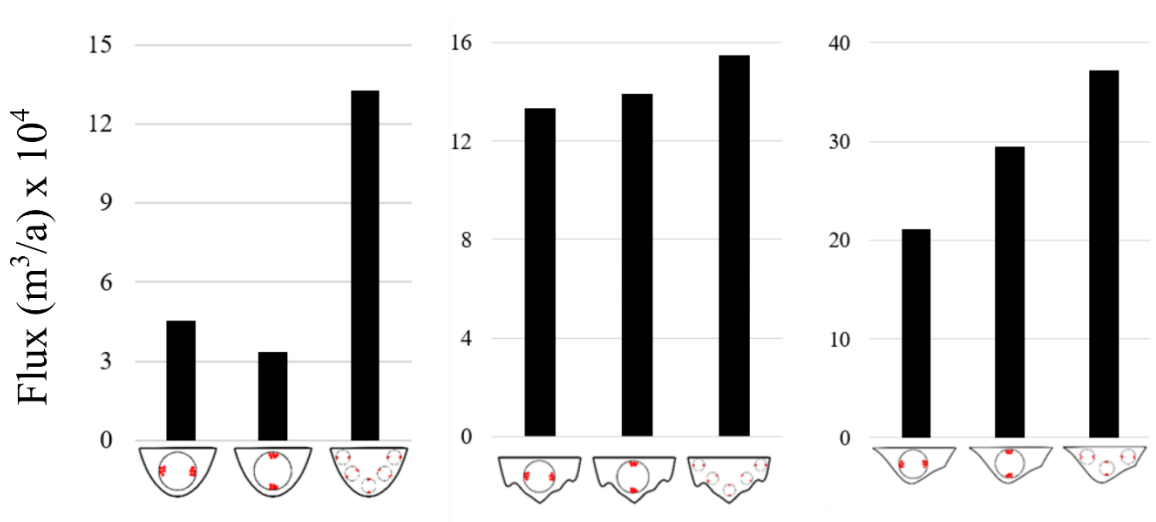

Figure 3.24: Flux in the rotating single-maximum fabrics. Each plot has flux for the transverse single-maximum, vertical single-maximum and rotating single-maximum fabrics. The first panel is the half-cylinder, the second panel is the straightened Jarvis and the third panel is the Jarvis geometry.

3.5 Realistic Temperate Glacier Scenario

To begin adressing the applicability of these extreme cases to natural scenarios, models were run on the straightened Jarvis geometry at temperatures of -1˚C for both frozen bed and slipping conditions. Fabric in these models was rotated so the maximum is perpendicular to the bed and the concentration of the fabric was decreased to a cone angle of 45˚, or half as concentrated as the runs above (Figure 3.25). This coinsides with fabric found in Jarvis Glacier, discussed in the next chapter. In these scenarios, the rotating fabric has a lower flux than the isotropic fabric because the single-maximum fabrics in the vertical and transverse directions have fluxes lower than the isotropic case, though the rotation reduces these differences. With a frozen bed, flux normalized to area for the rotating fabric is 0.71 m/a and 0.72 m/a for the isotropic case. With slip, normalized flux is 9.87 and 9.89 m/a, respectivly. This means that the average flow variation between isotropic and less concentrated rotating fabrics for both slipping and non-slipping cases is only 3.8% (Figure 3.26).

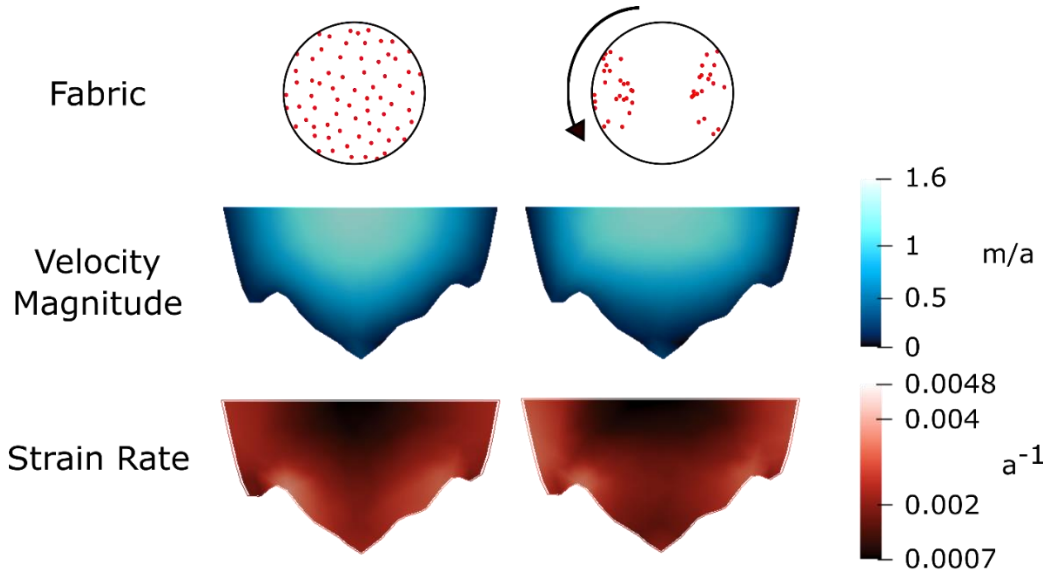

Figure 3.25: Velocity and strain rate in a weak maximum fabric. The velocity and effective strain rate (second invariant of the strain rate tensor) for the isotropic straight Jarvis is compared to a run with a weak maximum rotated to the bed. Both have a non-slipping bed and the ice is at -1˚C.

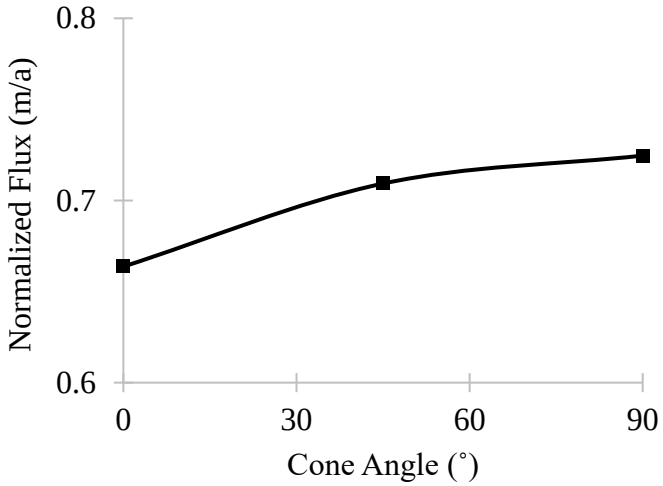

Figure 3.26: Rotating fabric flux versus cone angle. Flux for the rotating fabric, from highly concentrated to isotropic, is normalized to area. Run without slip at -1˚C.

3.6 Discussion on the Synthetic Model

It is important to asses this part of the project with a mindset of "this is the most extreme scenario." While many fabrics and temperatures modled here may not occur naturally in temperate mountain glaciers, they provide bookends for comparison to the natural scenarios. For example,

flux differences are stark with concentrated fabrics and warm temperatures (Figure 3.6), but for fabrics occuring naturally in temperate mountain glaciers, fabric may not be as great a factor as suggested by end members, as seen in Figure 3.25. Geometrically, it is also rare for glacial flow to be perfectly straight, emphasising the results found in the Jarvis geometry rather than the half-cylinder and straightened Jarvis; the effect of the bend in Jarvis is clearly visible in the fabric studies. In most cases, fabric was assigned based on general downglacier (longitudinal) direction, rather than to be parallel to flow at all times, and because there is a 90-degree turn in the flow of the Jarvis geometry, at the head of the glacier the fabric is misoriented from flow. This could relate to fabric inheritance in flowing ice (Ma et al. 2010), and is the cause of the shallower slope exhibited by the Jarvis model in Figure 3.15, a relationship that is perhaps more realistic than those exhibited in the other geometries. However, in this case, it is also important to note that inherited fabrics exists in low-strain environments, which a lateral margin is not (Wilson and Sim 2002). Because temperature-related deformation in this case is not reliant on flow direction, we see similar flux increases in all three of the geometries with increasing temperatures (Figure 3.9). This provides a threshold in these and further models where fabric can either have a greater or lesser influence overall on glacial flow than temperature.

3.6.1 Fabric-caused Flux Differences

The fabric that causes the fastest flow in this project is one where the c-axes are longitudinally oriented (Figure 3.7). This is due to the body forces of the model: flow is gravity driven so more deformation is pushed onto the non-basal plane of the crystal, similar to compression favoring deformation when c-axes are pointed in the direction of flow (Alley 1992). This fabric alignment is only feasable instantaneously in a natural scenario though, because of

the rotation, recrystallization and evolution that occurs when stress is applied to ice (Wilson and Sim 2002). However, when considering this project, this causes an interesting relationship where fabrics oriented with their c-axes perpendicular to the bed actually have a slower flow than the isotropic models (Figure 3.26). Despite the reduction of stress at the margins that rotating fabric provides (Figure 3.21), an isotropic fabric is still partially made up of longitudinal c-axes due to its random nature, and so that component overshadows the stress reduction of a rotating fabric. The key to viewing the relationship between fabrics aligned to the bed and deformation in the basal plane is to not have any component of longitudinal fabric within the orientation (Figures 3.21 to 3.23). For example, with highly concentrated fabrics in the half-cylinder, the two fabric cases with the greatest effective stress are the vertical and transverse single-maximums because the c-axes are sometimes parallel to the bed (Figure 3.21). When the fabric rotates, the areas of higher stress disappear from the geometry as all the ice can preferentially deform along the basal plane.

When comparing isotropic to anisotropic fabrics in both natual settings and models, it has been observed that anisotropic fabrics can actually be stiffer than isotropic fabrics. When the AIFlow Sover is used to model ice sheet - ice shelf dynamics, single-maximum and girdle fabrics are stiffer than the isotropic case because of the stress changes between the ice streams feeding the shelves and the shelves themselves (Ma et al. 2010). When stepping into a measured (rather than modeled) scenario, anisotropic fabrics collected in the lateral margin of Ice Stream B in West Antarctica also show a strenghtening relationship when compared to isotropic ice (Jackson and Kamb 1997). Jackson and Kamb (1997) suggest that this could be from a misorientation of the c-axes to the margin, but it is more likely that the anisotropic version of the flow law they

deduce from the ice is just more accurate than the isotropic one. This further validates the need to include anisotropy into flow laws, as done in this project.

3.6.2 Effects of Borders on Flow

When considering fabric borders, even 10 m of a single-maximum fabric in an otherwise isotropic glacier can change the flow of the glacier. In the straight Jarvis model, adding 10 m of single maximum fabric to the isotropic ice body increases flux by 26% (Figure 3.15). We can also see that there is a decrease in flux when the border changes from 100 m of single-maximum fabric to 100 m of isotropic fabric. Even though there is a larger area of single-maximum fabric in the isotropic border run, because the isotropic fabric is harder to deform, it holds back the flow of the glacier (Figure 3.16). If the border fabric is easier to deform (longitudinal single-maximum fabrics), then there is less resistance on the sides of the glacier and the ice flows faster. When I add slip to the model, the impact of a weak border decreases as strain rates concentrate to specific locations in the margin based on the shape of the bed, rather than being distributed throughout the ice (Figures 3.8 and 3.12). This connects to different flow types based on bed conditions, as described in Figure 1.3.

When end-member fabric and temperature borders combine, it is apparent that fabric determines the flow patterns more than the temperature at the extremes prescribed in this model. In the cases where I apply the single-maximum fabric to the border, most of the deformation occurs just at the border. In the isotropic border cases, flow mostly concentrates in the central regions where there is single-maximum fabric (Figure 3.27). When fabrics and temperatures are working together, i.e. the single-maximum border is also at 0˚C, flux increases by 18.4% from the fabric border model that is entirely -10˚C, or 100.4% from the temperature border model that is entirely

isotropic. The results that fabric is a greater determinant in flow could also be intensified in a natural scenario, as more aligned fabrics reduce shear heating, decreasing the temperature gradient at the margin (Minchew et al. 2018).

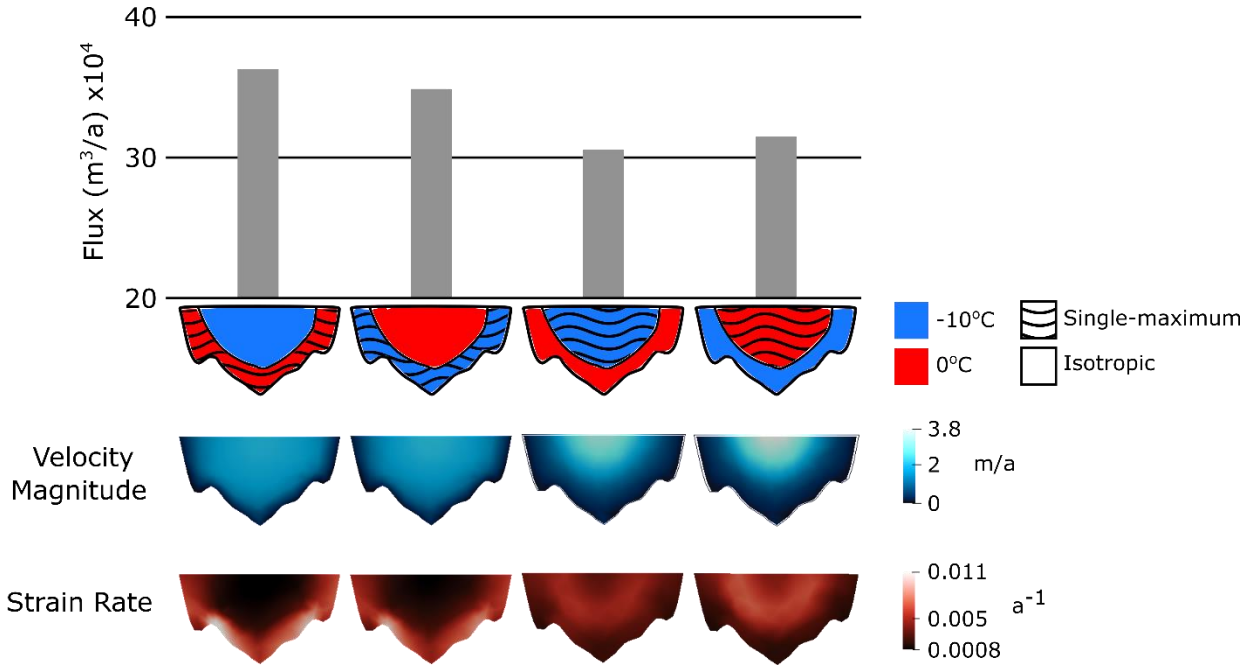

Figure 3.27: Combining fabric and temperature borders. These borders are 100 m thick and are the end members of the synthetic models. Flux, velocity magnitude and effective strain rate are above and below the border assignment patterns. Anisotropic fabric is a longitudinal single-maximum like in the border runs above.

3.6.3 Flux vs. Maximum Velocity

It is also important to acknowledge in this project that flux as shown here is just capturing one slice in an upper section of the glacier, which is usually just at the start of where the ice body speeds up (Figure 3.28). Flux is a useful measurement for comparison of an ice body that is moving in three directions, but it does not always give the scientist a full picture of the glacier. In the case of modeling slip, when we look at maximum velocity magnitude instead of flux, we get a very different picture of flow (Figure 3.29), which is ultimately more like the picture we obtain when

measuring the flux of the non-slip cases. Here, a longitudinal single-maximum fabric (x) is the fastest flowing again, though not to the extreme that it is in the non-slip model (Figure 3.18).

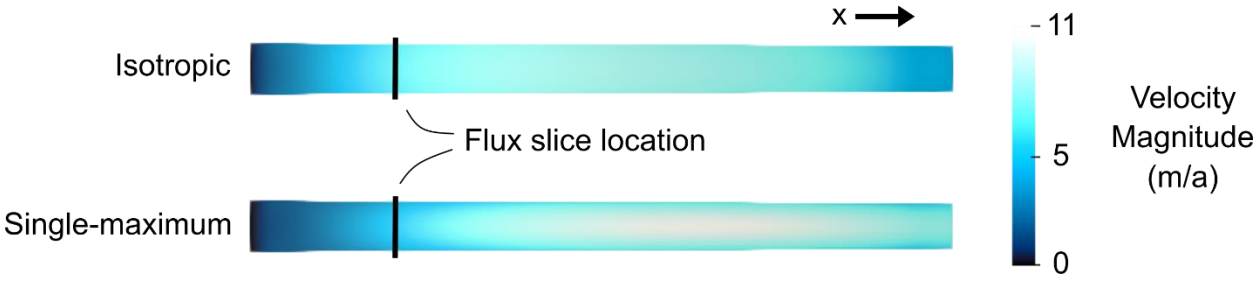

Figure 3.28: Surface velocity patterns for isotropic and longitudinal single-maximum runs. Though the velocity is lower in the single-maximum case at the flux slice location, the overall maximum velocity of this case is higher than the maximum velocity of the isotropic model.

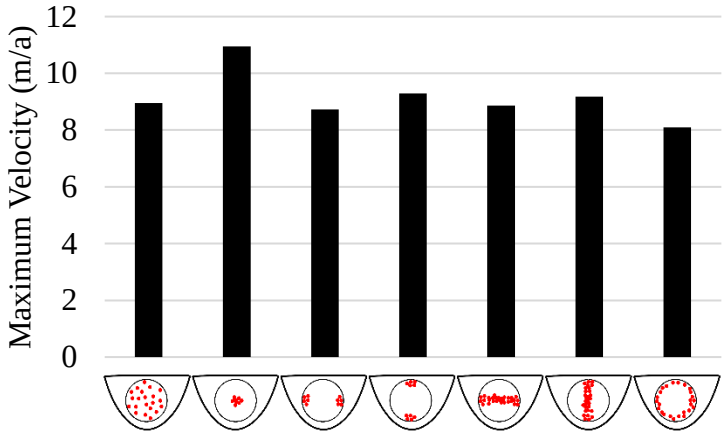

Figure 3.29: Maximum slipping velocities of the seven major fabric types. Maximum velocity magnitudes are for the whole ice body in the half-cylinder model with slipping boundary conditions.

3.6.4 Bed Roughness

To test the impact of bed roughness on the model, one can compare the half-cylinder model and the straightened-Jarvis model. Interestingly, the geometry with the rough bed has faster speeds than the smooth bed geometry (Figure 3.30), but this can be attributed to geometry size rather than the bed. Previous studies have found that anisotropic ice can form areas of stagnation around bedrock rises (Mangeney et al. 1997), and in the two models we can see a possible effect of this

stagnation. With the single-maximum fabric, there is a 40% increase in flux from the half-cylinder to the straight Jarvis geometries. With the isotropic case, the increase in flux is 75%. If the bed change affected both fabrics similarly, we would expect to see similar flux increases. Instead, we see a greater flux increase in the isotropic case, meaning the anisotropic case might have pockets of ice with lower velocities, causing a smaller increase in flux. While this may not mean much for these synthetic end-member cases, in a natural system this stagnation could change a glacier from slipping to frozen-bed regimes.

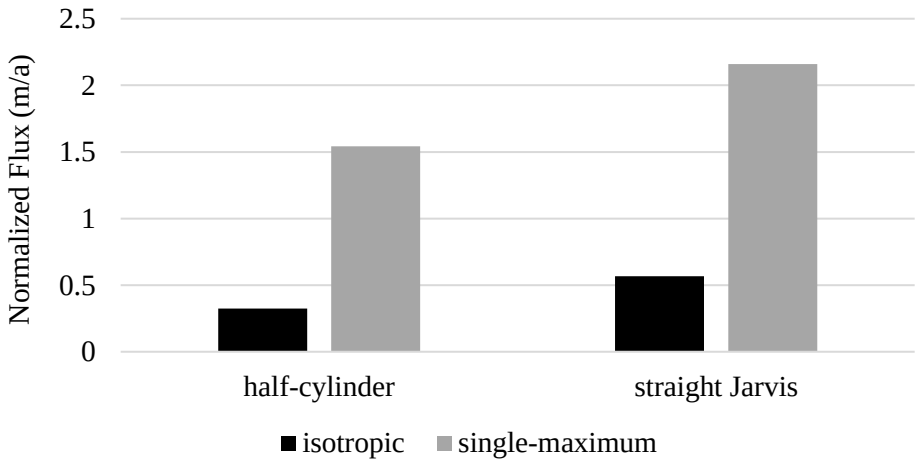

Figure 3.30: Flux versus fabric in the two simplest geometries. Both have isotropic and longitudinal single-maximum fabrics. I divide the flux of the slice by the area to normalize it.

3.7 Synthetic Model Conclusions

An important point to note when comparing the influence of fabric versus temperature is that my temperature model is bound by the values I prescribed. With fabric, it is impossible to get the c-axes more concentrated than all of them pointing in the exact same direction. But with temperature, my imposed bounds are -10˚C and 0˚C, even though it is possible for ice to get much colder, depending on the surrounding environment and movement of the ice. This model also leaves out other variables important to flow, such as water content and till, in order to isolate the impact that fabric and temperature have on the flow of my glaciers.

In this synthetic study, the longitudinal single-maximum fabric can increase flux by 375% from the isotropic case while temperature only has the ability to increase flux by 32% from -10˚C to 0˚C. When I extend the temperature bound to -20˚C, the flux increase doubles to 76%, but that is still much lower than the variation synthetic fabric can provide to flow. However, when fabric concentration decreases and patterns are changed to a more realistic formation, the impact fabric has on flow is drastically reduced.

Regarding borders along the lateral margins and bed, when the border is easily deformable (such as a single-maximum fabric or warm ice), the flow of the glacier speeds up. When the border is hard to deform (such as isotropic or cold ice), the flow of the glacier is held back. This is apparent even when there is just 10 m of different ice at the border, a distance from the margin that scientists would often not survey even in a project specifically for marginal properties because of debris and crevassing.

Slipping boundaries with certain fabrics in my model also show a high strain rates along the margins, suggesting the velocity gradient of a sliding glacier concentrates to these locations (Figure 1.3). In a glacier that is only deforming under its own weight, the velocity gradient (and therefore strain rates) is more distributed throughout the ice body. We can see this change in the strain rates of my model. We can also see a reduction in effective stress when the fabric is perpendicular to the bedrock, as would happen in a realistic scenario. Ice crystals turn so c-axes are perpendicular to the stressing factor when shear is present so they can slip on the basal plane (Alley 1992), and the results of this stress-reducing behavior are visible in my model when separated from longitudinal single-maximum fabrics. A strengthening relationship between this rotated fabric and isotropic cases is also present, due to isotropic fabric having some component of a longitudinal single-maximum. This relationship is not unheard of though, and scientists in the

past have suggested it shows how models based on aligned fabrics are more realistic than isotropic models (Jackson and Kamb 1997).

Despite a deviation from reality that comes from testing end-member parameters, there is valuable information that has come out of this study: 1) the model is more sensitive to longitudinal fabric than transverse and vertical fabrics, but 2) stresses and strain rates show expected patterns so my model is valid and the conditions at which longitudinal single-maximums increase flow just might not occur naturally in glaciers. Also, 3) lateral margin parameters do matter in 3D glacial flow, especially when considering the end-members of fabric and temperature that I tested, and 4) the sensitivity of temperature stays relatively constant throughout different ice bodies while the sensitivity of fabric is wildly dependent on bed conditions and the geometry of the glacier. To relate these sensitivity tests back to a more moderate natural scenario, we will travel to Jarvis Glacier, Alaska in the next chapter and dive into how much the lateral margins matter with naturally occurring fabrics and temperatures.

CHAPTER 4

JARVIS GLACIER: A CASE STUDY

4.1 Characteristics of Jarvis Glacier, Alaska

Jarvis is a mountain glacier in the Eastern Alaska Range, Alaska, 175 km southeast of Fairbanks. It is approximately 8 km long and 1 km wide at the widest point (Figure 4.1). It has a surface slope of about 5˚ and flows from south to north, with the accumulation mostly coming from shadowed snow pack in the south, though Jarvis has had a negative mass balance for the last several years (Miner et al. 2018). Jarvis exists around 1500 m elevation, just north of the Denali Fault, with surrounding mountains reaching between 2000 and 3000 m. These mountains host several hanging glaciers that feed water into the Jarvis system, which takes a 90˚ turn from the head to the toe. In the southwest corner there is a small feeder glacier which joins the flow of the main Jarvis arm at this turn. The bed and margins of Jarvis are primarily a mica-schist, which fractures as the glacier flows over it. The rock weathers once it reaches the surface. The glacier valley is v-shaped, suggesting the landscape development of the Jarvis system is in its early stages where subglacial shear and erosion are high (Braedstrup et al. 2016).

At the margin in the southwest corner, a team of scientists from University of Maine and Dartmouth College joined together for a multi-year study of the shear margins of a mountain glacier. Jarvis's southwest corner provided a location where scientists could access a shear margin without placing themselves and equipment in hazardous situations, and where flow could be measured both near the margin and toward the center of the glacier. This field site (Figure 4.1) acted as a base camp for the study of Jarvis Glacier in 2017 and 2018.

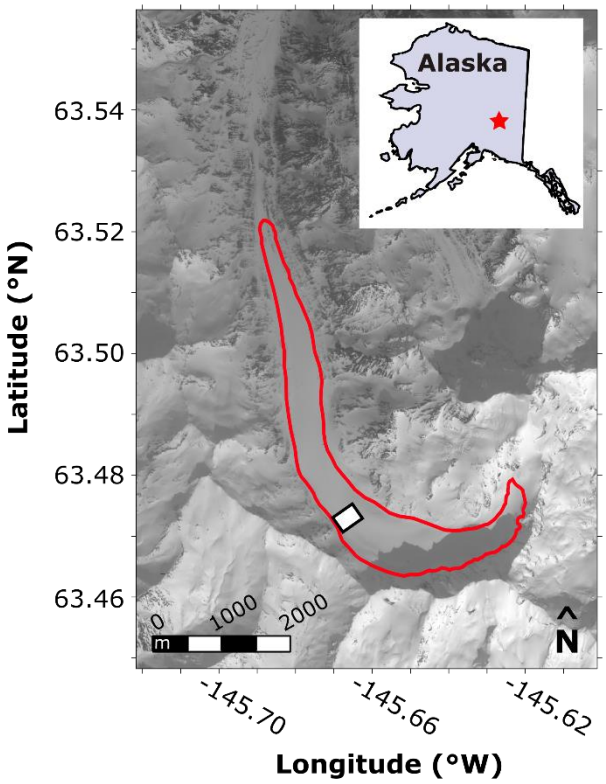

Figure 4.1: Jarvis Glacier, Alaska. The red outline is the extent of the ice and the white box is the field site visited in 2017 and 2018.

During the 2017 field season, our team drilled five 8.2 cm-diameter cores toward the margin of the field site, two of which I will focus on in this study (Figure 4.2). We shipped the cores back to Maine, where they stayed in the -23˚C freezer at the University of Maine while the analysis occurred. A scanning electron microscope modified to hold ice recorded c-axis direction of the crystals for use in this project (Gerbi, 2018). Back on the glacier, scientists froze ST 3D magnetometers (www.st.com/en/mems-and-sensors/lsm303c) into the boreholes to measure deformation and temperature throughout the following year. In addition to the cores, the team placed thirty-three stakes on the surface of the field site in 2017 and measured the GPS positions of those stakes in July. Returning to the glacier in August 2018, we rerecorded the GPS positions of those stakes, allowing us to calculate a surface velocity for the field site by subtracting the

second position from the first and dividing by the time that had past. Through these data, we can see a visible velocity gradient as the ice comes closer to the western margin of the glacier, with the velocity decreasing by 3.6 m/a in about 125 m. From that 125 m point out into the center of flow (another 90 m), velocity only increases by 1.2 m/a, showing a concentration of the velocity gradient along the margin (Figure 4.3). Using the surface velocity field generated by the stake measurements, I calculated vorticity of the ice using Surfer software (www.goldensoftware.com) (Figure 4.4), and there is a clear divergence between clockwise and counterclockwise curl (Figure 4.5). This divergence marks a region rich in moulins, a feature prevalent on the western margin from our field site to the toe of the glacier. Our surface strain rates corroborate with values others have found in Alaskan glaciers (Wu and Christensen 1964).

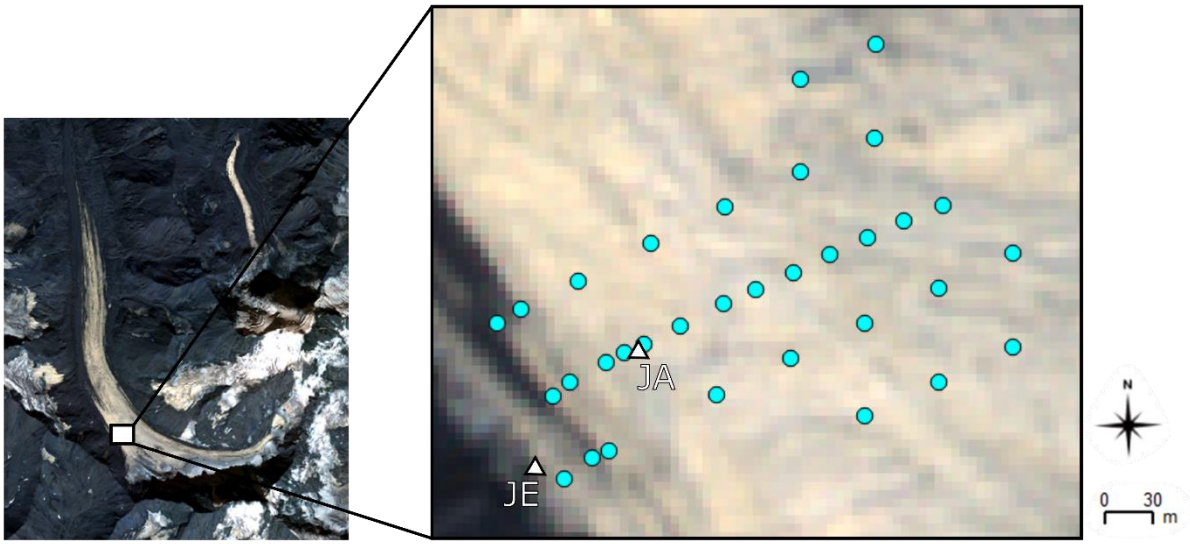

Figure 4.2: Jarvis field site with velocity stake and core locations. Cyan circles mark stakes and white triangles mark the JA and JE cores. JE reached bed at 18 m and JA reached bed at 80 m. Satellite imagery is from Planet (2017) and has a 5 m resolution.

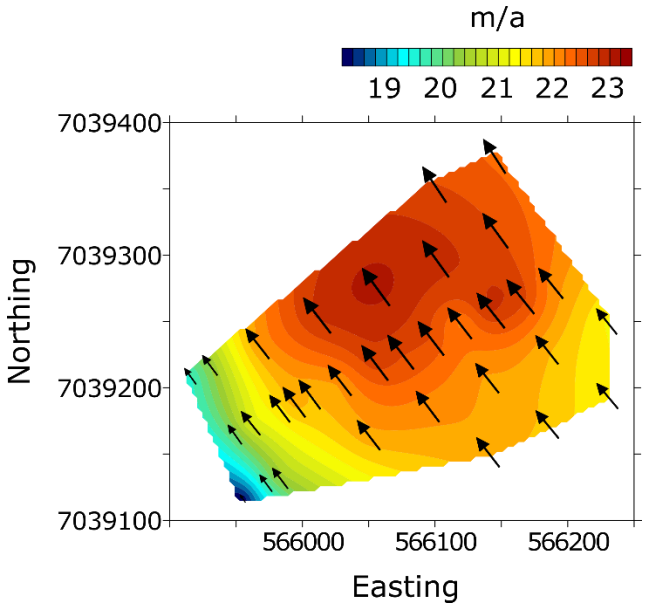

Figure 4.3: Surface velocity of the Jarvis Glacier field site. Black arrows are the velocity vectors for each stake, scaled between 18 m/a and 24 m/a to show velocity decrease at lateral margin. Colors are the 2D magnitude of the stakes, expanded throughout the area with a Kriging interpolation. GPS points of the stakes are from July 2017 and August 2018.

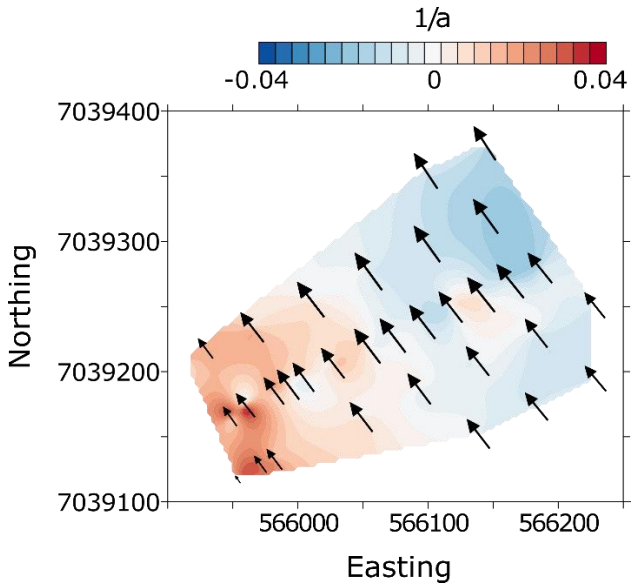

Figure 4.4: Surface vorticity of the Jarvis Glacier field site. Black arrows are the velocity vectors for each stake, scaled between 18 m/a and 24 m/a to show velocity decrease at lateral margin. Color is the vorticity calculated from the velocity data and interpolated with a Kriging method. Red is counter-clockwise curl, blue is clockwise curl, and white is no curl.

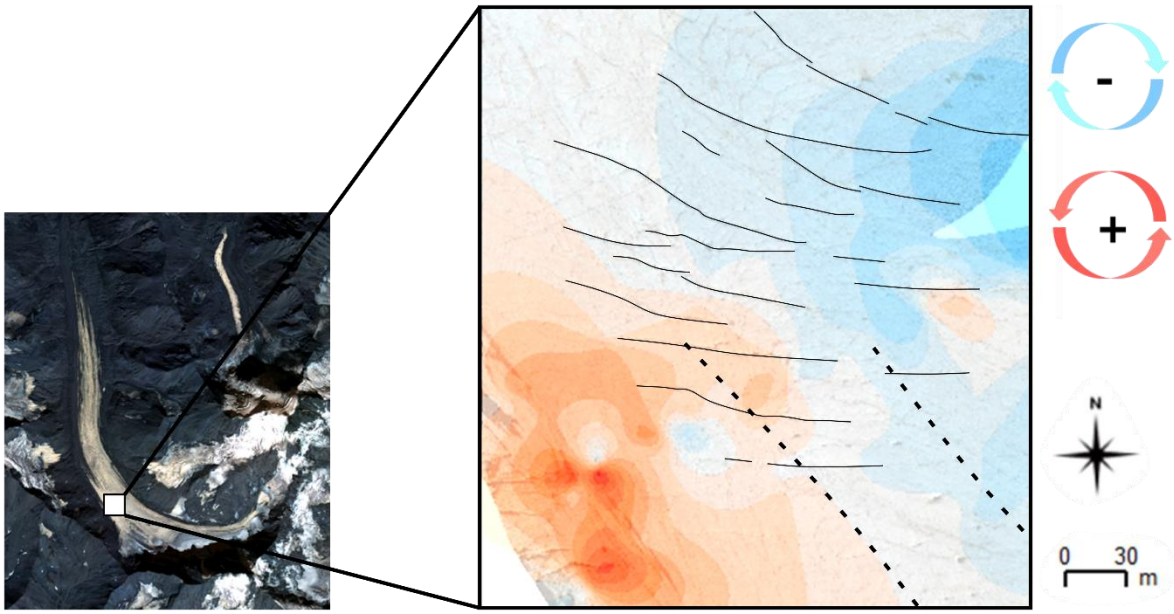

Figure 4.5: Evidence of flow patterns at the field site. Red is counter clockwise vorticity and blue is clockwise vorticity. Dotted lines mark the region rich in moulins. Solid lines highlight major crevasses. Vorticity overlays drone imagery from the 2018 field season and the satellite image is from Planet (2017). Maximum positive vorticity is 0.04 a^{-1}, maximum negative vorticity is -0.02 a^{-1}, and the white portion of the image, where divergence is occurring and characterized by the moulins, is a vorticity of 0. More data on strain rates are in figure B2 in Appendix B.

In 2018, while remeasuring the GPS positions of the velocity stakes, we mapped surface features along two transects in the field site: one to the north and one to the south. These marked the locations of the crevasses and moulins (marked in Figure 4.5), and recorded the strike and dip of debris-highlighted bedding planes flowing from the feeder glacier (Figure 4.6). On the lateral margin side of our field site, these bands dipped at around 55˚ to the northeast. Crossing the field site, you reach the other side of the flow contribution from the feeder glacier and encounter bands that dip around 47˚ to the southwest. The margin deforms these bands as they are advected downglacier.

Figure 4.6: Bedding planes in the field site. These debris-highlighted bedding planes are sourced from the feeder glacier in the southwest corner of Jarvis. Red arrows highlight planes. The first image looks to the south, the second to the west, and the third looks inside a crevasse to see the debris band with depth.

In the JA and JE cores, a general grain analysis of horizontal thin sections shows large cuspate grains (probably assisted in their expansion by fluid in the ice and pinned by impurities), shearing indicated by regions of smaller grains and elongated bubbles, and healed fractures where smaller grains have recrystallized (Figure 4.7). 10 samples in JA and 5 samples in JE determine the average fabrics in the cores, with JA showing increasing orientation with depth and JE fabric aligning to a broad single-maximum (Figure 4.8). All measurements were made on samples with more than 12 grains, so modeling error for the AIFlow Solver is low (Gillet-Chaulet et al. 2005). However, most samples had less than 100 grains, which others have encountered high deformation variation in due to the prevalence of outlier grains changing the fabric tensor (Treverrow et al. 2015). In this project, c-axis placement in an isotropic fabric produces a 3.74% variation in flux and 4.50% variation in maximum velocities of the model (Table 3.1).

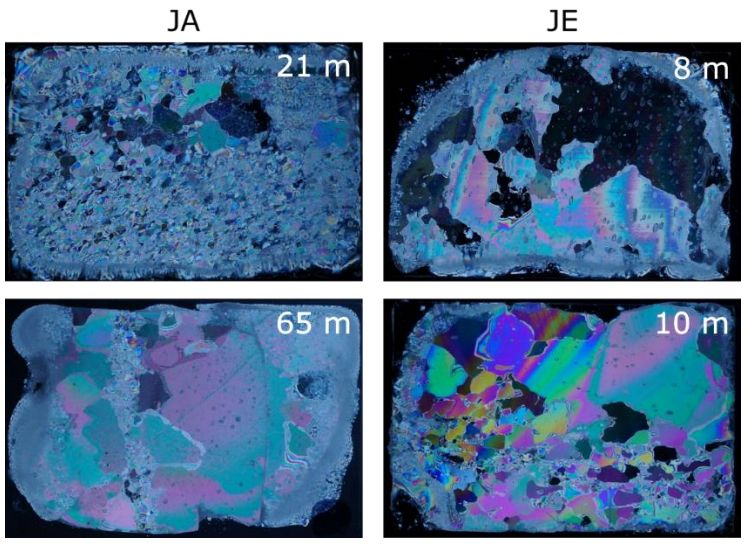

Figure 4.7: Thin sections from different depths in the two ice cores. Depth is in the upper right corner of each thin section. From upper left traveling clockwise, we have: shear zone denoted by grain size reduction and foliation, large cuspate grains and bubble elongation, shear zone denoted by grain size reduction and bubble elongation, and a fracture with smaller recrystallized grains inside.

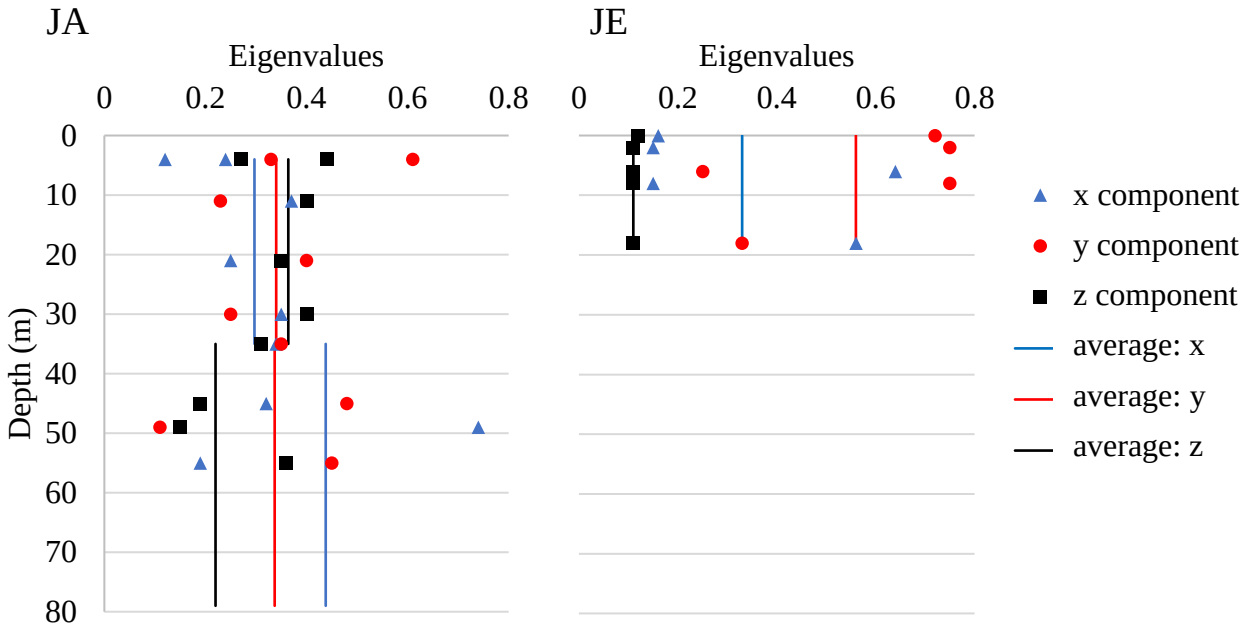

Figure 4.8: Fabric eigenvalue points and averages for the JA and JE cores. Blue triangles are Fabric 1, red circles are Fabric 2, and black squares are 1 – (Fabric 1 + Fabric 2) as described in section 2.2.1. Lines express average eigenvalues. I chose 35 m as the place to shift the average in JA because the fabric is closest to isotropic in that location. The closer the average lines are to each other, the more isotropic the fabric is. The farther apart the lines are, the closer the fabric is to a single-maximum.

ST sensors frozen into the JA and JE boreholes recorded ice temperature every 6 hours from July 28th, 2017 to August 7th, 2018. Ian Lee from Dartmouth College retrieved the data from these sensors during the 2018 field season. Borehole temperature doesn't vary much with proximity to the margin, and instead varies with depth. Annual temperatures between the two cores average at -0.09˚C, with JE's average being 0.12˚C colder than JA's average (Figure 4.9). There is seasonal variation in the upper 20 m of the core due to atmospheric temperature changes, but below 20 m, patterns are consistent throughout the year (a monthly temperature plot is in Appendix B).

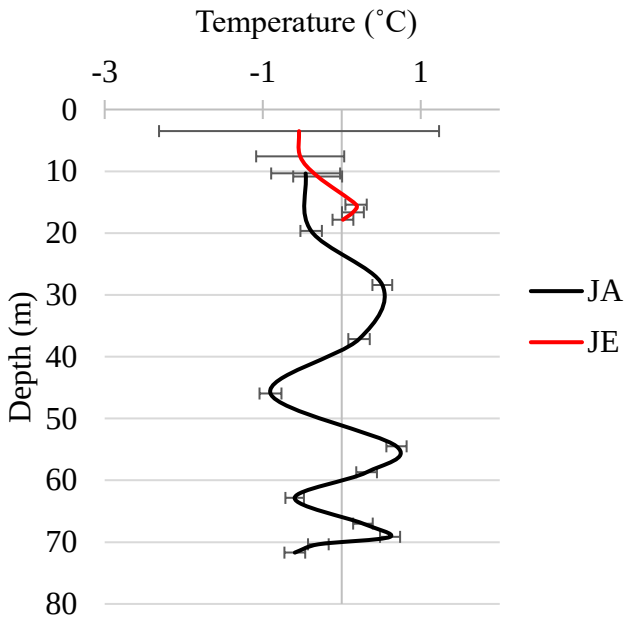

Figure 4.9: Annual temperature profiles through the JA and JE cores. Values plotted here are averages throughout the study period with depth. Error bars are standard deviation and mark sensor placement. Data from Lee 2019.

4.2 Application of Anisotropic Border Model to Jarvis Glacier

In this section of the project, I combine the border model and data recorded in Jarvis. For fabric-related models, all slipping and non-slipping cases have a temperature of -0.09˚C, the average temperature of Jarvis's cores. For temperature related models, the fabric is isotropic. I

tested several versions of the border model, varying the width of the border and the placement of specific fabrics. The first version takes the placement of the cores into account. Since JE is 25 m from the margin, the model has a 50 m border, placing JE in the center of that fabric pattern. The rest of the model has fabric based on JA's upper and lower average fabrics. The second version accounts for the insight our vorticity data gave us (Figure 4.4), that the margin could be influencing ice flow up to 175 m into the glacier. In this run, a border of JE fabric (fabric more oriented to the margin) is assigned 175 m into the glacier, and the rest of the ice has fabric from JA. The third version of this model has JE fabric rotated to the general direction of the margin and bed, and with JA fabric in the core (Figure 4.10). None of these models in their totality vary flow much from the isotropic case. However, when comparing the individual fabrics to each other, flow can vary up to 9%.

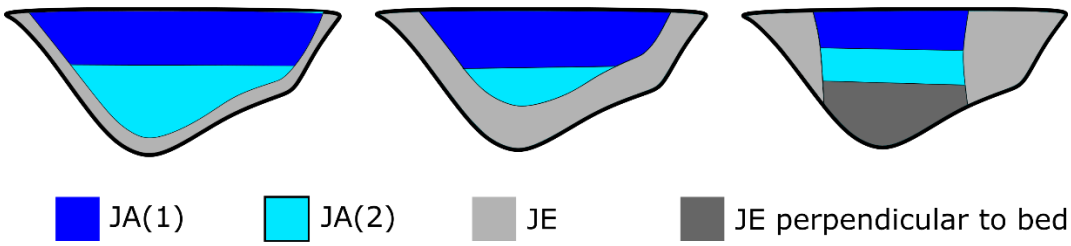

Figure 4.10: Core fabric locations assigned to the Jarvis geometry. JA(1) and JA(2) are from the upper and lower portion of JA, respectively. JE is the average fabric in that core and "JE perpendicular to bed" is rotated so that JE's primary fabric direction is now oriented to the bed.

The first model, with a 50 m JE border and an upper and lower central fabric based on JA, has a 1.4% slower flow than the isotropic case. Flux values are similar with the addition of slip, but an order of magnitude higher. Maximum velocities in each case are 2.40 m/a when isotropic and 2.42 m/a with Jarvis's fabric. These values are also not vastly different from each other, though this measurement does favor the Jarvis model (Table 4.1). When the JE border extends 175 m into the ice to reach where the lateral margin no longer influences the flow pattern, maximum velocity

increases to 2.62 m/a and flux increases by 2.5% from the isotropic model. However, with the addition of slip, flux drops below the isotropic case again, with a decrease of 1.03%. Even when the JE fabric rotates to be perpendicular to the bed we don't see a vast difference in flux or maximum velocity (Table 4.1), with a 1.5% increase in flux from the isotropic case in the frozen-bed scenario and a 1.5% decrease in flux in the slipping scenario. JA has an average of 98 grains per sample and JE has an average of 58 grains per sample. When I account for fabric variation (addressed in section 3.2.1), I cannot confidently say there is a difference between the models using Jarvis's fabric and an isotropic model; with 100 grains per sample, variation in the isotropic model's flux is 3.74%.

	Flux (m^3/a)	**Maximum Velocity Magnitude (m/a)**
Jarvis Fabric, 50 m border	420862.5	2.42
Jarvis Fabric, 175 m border	437508.8	2.62
Jarvis Fabric, JE rotated	433161.8	2.54
Isotropic	426813.5	2.40

Table 4.1: Flux and maximum velocities for the Jarvis fabric models. Listed here are the three fabric patterns and the isotropic case. These values are for the frozen-bed conditions.

Despite this overall similarity with the isotropic model, when comparing the three averaged fabrics from Jarvis's cores to each other, there is a 9% increase in flux from the slowest case, the bottom of JA, to the fastest case, JE (Figure 4.11), showing the impact individual fabrics can have on flow.

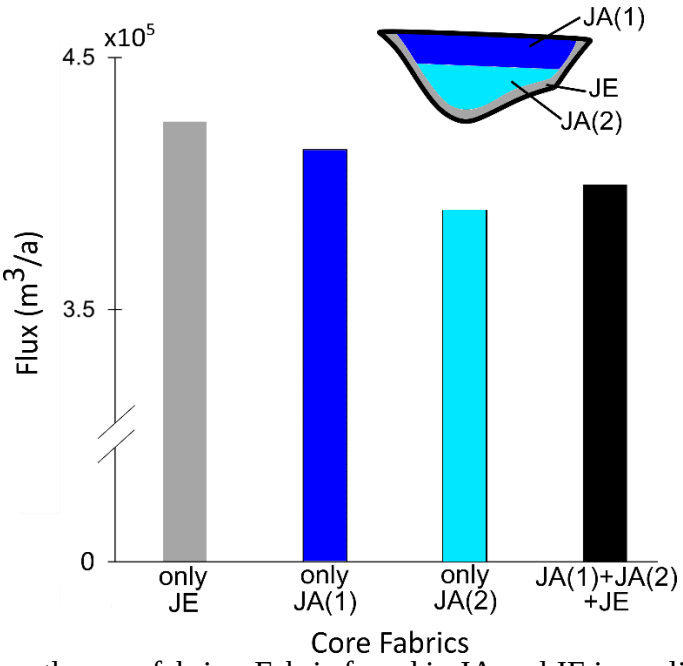

Figure 4.11: Flux versus the core fabrics. Fabric found in JA and JE is applied to the non-slipping model. The first three columns are the fabric found in each location: JE, the top half of JA and the bottom half of JA. The fourth black bar is the combination of all three fabrics, placed as seen in the schematic at the top of the graph. These runs have the average ice temperature from July 11th, 2017 to July 28th, 2017, -1.959˚C.

Jarvis's average annual temperature ranges from a minimum of -0.90˚C to a maximum 0.69˚C throughout the two cores, with an average between the cores of -0.09˚C. While flux doesn't increase much between -0.90˚C and -0.09˚C, once temperatures increase above 0 to 0.69˚C, flux increases by 28% from the colder ice for the non-slipping case and 13% for the slipping case (Figure 4.12). Jarvis's recorded temperature does not vary much with proximity to the lateral margin, as shown in Figure 4.9, but instead with depth. Temperature changes with depth would still be of importance when considering glacier flow, however that is outside the scope of this project. Instead, to test the impact these recorded temperatures have on lateral margin resistance (if those temperatures had differed at the margin), I apply Jarvis's warm and cold ice to the 50 m and 175 m border models. When borders of Jarvis's warmest temperature, 0.69˚C, exist in a body of Jarvis's coldest temperature, -0.9˚C, the glacier speeds up. With a 50 m warm border, flux

increases by 8.5% in the non-slip model and 2.6% in the slipping model. With a 175 m warm border, flux increases by 26.8% in the non-slip model and 8.2% in the slipping model.

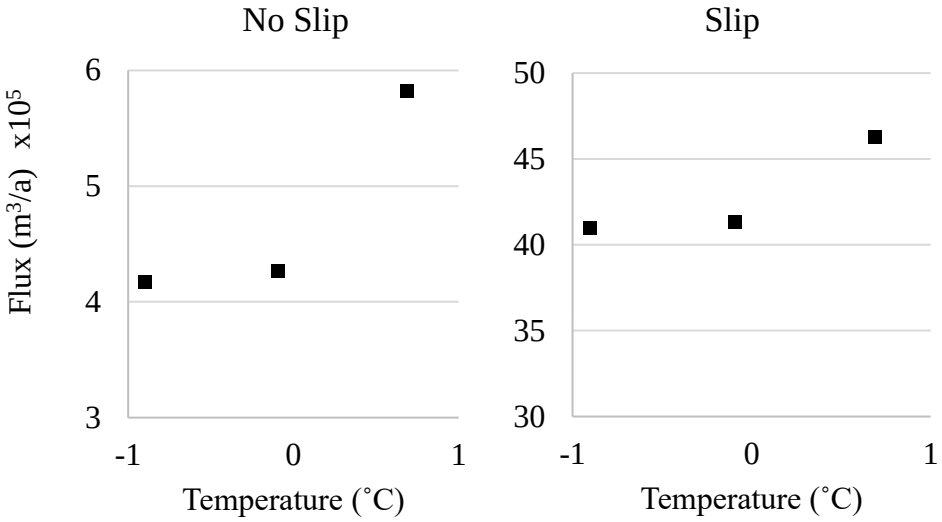

Figure 4.12: Flux versus the core temperatures. **N**on-slipping and slipping runs are shown here with the low, high and average temperatures from Jarvis's two cores.

The fourth, and final, border model applies different fabrics to just the lateral margins, keeping the fabric of the bed and center the same, to separate the influence of the margins from the influence of the bed. I split the 175 m border into three sections: the left margin, the right margin and the bed. In this model, the bed is kept at a rotated JE fabric while the margins are a generated single-maximum perpendicular to the bed with varying cone angle (Figure 4.13). None of the slipping runs have a velocity change higher than 3.74%, the variation that can come from the creation of a fabric. In the non-slip runs, if a rotating single-maximum fabric is more concentrated than a 70˚ cone angle, it reduces flow enough to put fluxes outside that variation (Table 4.2).

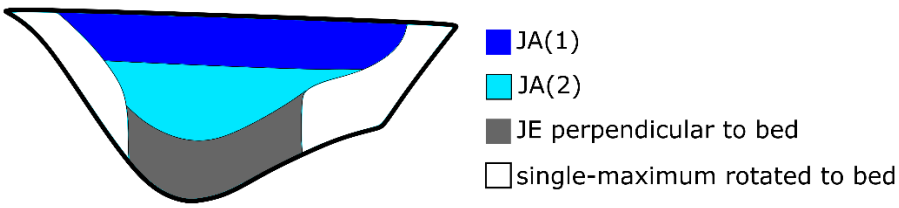

Figure 4.13: The lateral margin border model. Blue, teal and dark grey areas stay consistent throughout the runs. White fabric is a rotating single-maximum perpendicular to the bed; the cone angle of this fabric was varied from concentrated to isotropic.

	No Slip		Slip	
	% Decrease		% Decrease	
Lateral Margin Cone Angle	**From Lateral Margin Isotropic**	**From All Isotropic**	**From Lateral Margin Isotropic**	**From All Isotropic**
1	18.59	17.38	1.53	2.14
15	17.01	15.78	1.52	2.13
30	13.26	11.98	1.70	2.31
45	9.66	8.32	1.35	1.96
70	3.63	2.20	0.60	1.22
90		-1.48		0.62

Table 4.2: Variation in flux between lateral margin models. In the non-slip models, the anisotropic runs almost always have a lower flux than the all-isotropic case. In the slip models, more of the anisotropic runs have higher fluxes than the isotropic case, but variation overall is less. Lateral margin fabric has a greater variation in flux when there is no slip than when there is slip.

4.3 Modeled Flow vs. Measured Flow

Surface velocities of the slipping 175 m Jarvis fabric border model reach a peak of 16 m/a to the north of the field site (Figure 4.14). This peak is 7.4 m/a slower than the maximum velocity measured at our field site. At the field site in the model, downslope velocity is around 8 m/a, or 10 m/a slower than the average measured downslope velocity, though a clear region of deformation occurs along the western lateral margin of the model as the ice flows around the bend (Figure 4.15). When looking into this margin at the horizontal shear strain rate (du/dz) through the JA and JE cores (Lee 2018), we can see that my model is missing some component of basal shear (Figures 4.16 and 4.17). Modeled profiles are within some of the errors, but not all, and fit most closely

with the upper portions of JA, the area of the glacier that has the least basal or lateral margin shearing.

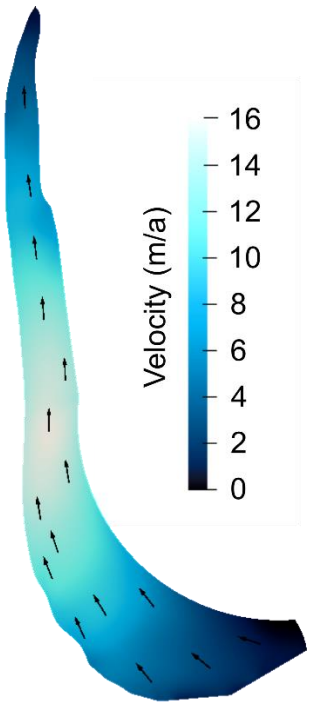

Figure 4.14: Surface velocities of the slipping 175 m border model. Vectors are 2D flow direction and colors are the 3D magnitude.

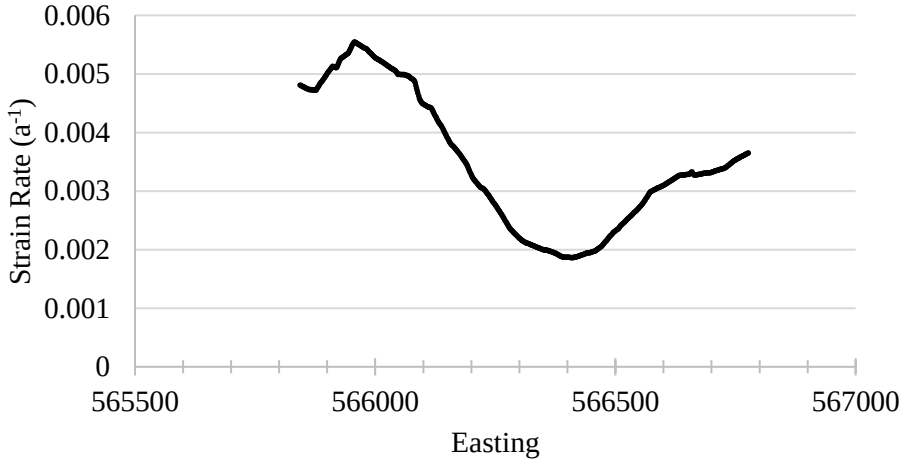

Figure 4.15: Effective strain rate across the surface of the glacier at the field site. These data come from the slipping 175 m border model and a temperature of -0.09˚C.

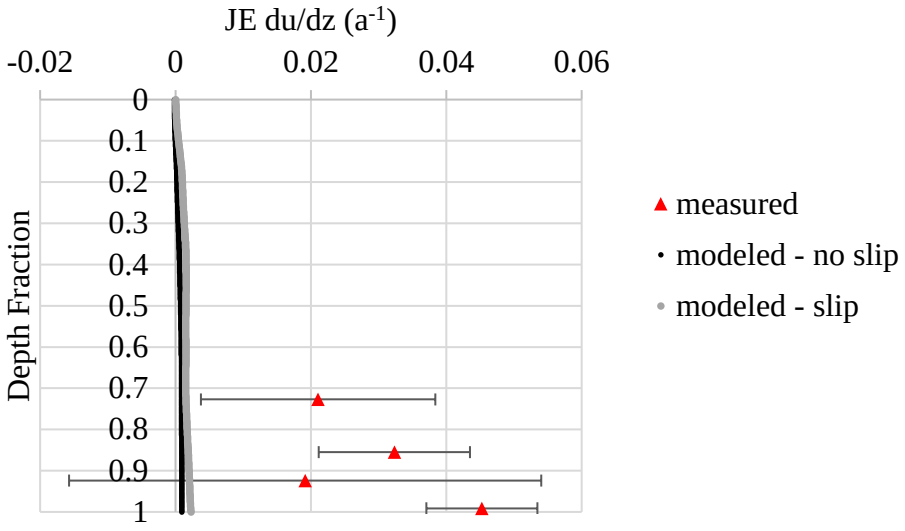

Figure 4.16: Horizontal shear strain rate of JE. Measurements from the JE core are compared to the 50 m border model.

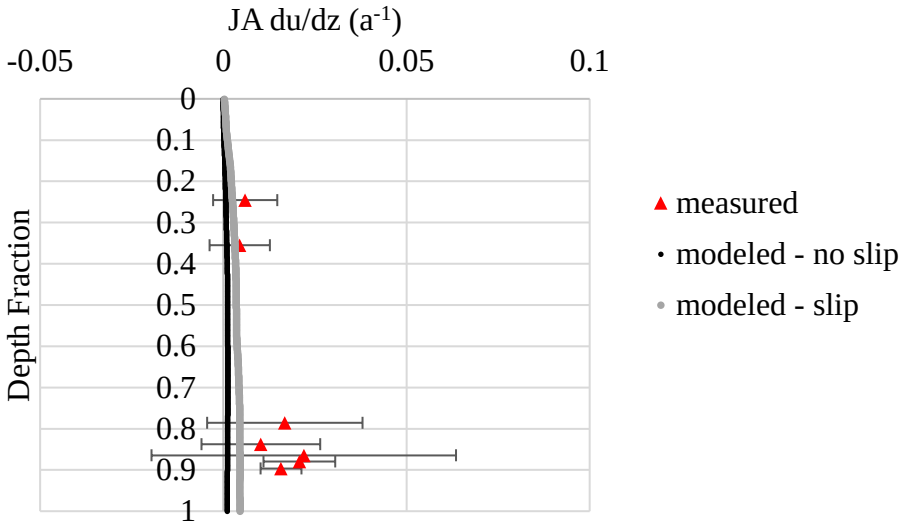

Figure 4.17: Horizontal shear strain rate of JA. Measurements in the JA core are compared to the 50 m border model.

4.4 Discussion on Modeling Jarvis Glacier

Jarvis is a wet, anisotropic, temperate mountain glacier resting on till with a feeder glacier coming into our field site. Because of the water content and bed, Jarvis flows at faster rates than what my model captures. This is apparent in the horizontal shear comparison between my model

and the measured rates: basal deformation is occurring in Jarvis not seen in the model. That said, it is clear from the vorticity measured at the field site that Jarvis's western lateral margin does still impact flow. Changes in the vorticity of our field site align with a row of moulins that starts upglacier and continues downglacier of our field site, highlighting a divergence in flow (Figure 4.5). This vorticity change, which is the part of the field site with the highest velocity, could be a combination of the margin ice held back by contact with the valley wall, and the main flow having its highest velocities on the western side because of the curve. Through this assumption, when the vorticity changes to a counter-clockwise rotation, we see evidence of where the margin begins to influence ice flow, about 175 m from the western side of the field site. In this area we also see a connection between measured velocity and modeled strain rates. The strongest velocity gradient exists between Easting 565900 and 566000 at the field site. This location in the model is also where a shear zone has developed at the surface, characterized by a peak in the effective strain rate (Figure 4.15). This suggests that while my model doesn't account for till deformation or water content, it is still capturing regions affected by the geometry of the glacier, especially as ice flows around Jarvis's bend and forward motion is resisted by the margin.

When it comes to the temperatures and fabrics of Jarvis, there are clear patterns, but these patterns could be caused by several different variables. Temperature variation is greatest in the upper 20 m of the core from atmospheric influence, but there are also fluctuations present in the ice throughout the year as we travel deeper into the ice. These fluctuations could be from water access or shear heating, but we do not have enough knowledge of the Jarvis system or enough measurements to be able to form a conclusion about this based on the data we have. When modeling these different temperatures though, expected patterns arise where the warmer the ice

the faster the glacier flows as warm ice allows for more deformation to occur (Mellor and Testa 1969).

Like temperature, there is a clear heterogeneity in the fabric with depth, which could also be caused by water access and shear zones, as well as recrystallization, grain boundary migration, or impurities in the ice (Hudleston 2015). However, unlike temperature, there is a distinction between the fabric of JA and the fabric of JE. This this ties into a larger issue in the scientific community when considering studies that have only cored in one location: there could be fabrics nearby that would show a faster or slower modeled flow due to inheritance or deformation (Wilson and Sim 2002). This would become most important in locations with a more concentrated fabric than what was measured on Jarvis, such as cold polar ice (Gow and Williamson 1976), or places where shear margins have significantly altered crystal orientation (Wilson and Sim 2002). Differences between JA and JE could incorporate some fabric inheritance from upglacier: the upper portions of JA that are closest to an isotropic fabric could suggest little deformation (and therefore the fabric has not been overwritten), but it is important to note that this fabric could also be coming from the feeder glacier rather than the main arm of Jarvis, which shortens the inheritance distance even more. Fabric is more concentrated in JE and the bottom of JA, where shearing at the margin and bed would cause single-maximum fabrics to form (Alley 1992), but it is still a weak orientation. This anisotropy does not differentiate flow from an isotropic model, at least not while we are measuring fabrics with less than 100 grains per sample. If fabric were to become more concentrated and temperatures were low enough to freeze Jarvis to the bed, lateral margin fabric could have a strengthening effect, as seen in Table 4.2 and discussed in the previous chapter. Ultimately, for Jarvis's fabric to overcome the deformation influence of its warm

temperatures, it would have to be a much larger glacier (Minchew et al. 2018) in a much different environment.

4.5 Case Study Glacier Model Conclusions

Taking my anisotropic border model and comparing it to data collected on Jarvis Glacier in 2017 and 2018 allows us to see how accurate my model is for realistic fabrics and temperatures, and to see if there are other factors besides these that are contributing to Jarvis's flow. Modeled deformation in the upper 85% of JA is within the margin of error for the recorded deformation within the core, but there is additional deformation happening close to the bed that my model is not capturing. This leads to surface velocities that are almost twice as fast on Jarvis as they are in my model, despite the application of slipping boundary conditions. This additional deformation could be due to water in the ice (Duval 1977) or Jarvis's mica-rich till, variables that my model does not take into account.

Between fabric and temperature in this case-study scenario, temperature has the greater effect on flow. In Jarvis, the 1.59˚C increase from Jarvis's lowest recorded temperatures to its highest recorded temperatures increases flux by 28%. Natural fabrics do not vary flow from an isotropic fabric in this setting though, because of the weak c-axis concentrations and low number of grains per sample, even at the lateral margins. For fabrics to differ flow from the isotropic case, and assuming c-axes are oriented normal to the lateral margin, the glacier must either be frozen to its bed or have more than 100 grains per fabric sample (Table 3.5). We did not observe these scenarios at our Jarvis field site.

CHAPTER 5

PROJECT DISCUSSION AND CONCLUSIONS

5.1 Including Lateral Margins in Glacier Models

Defined fabric and temperature in the lateral margins of glacier models can change how a glacier flows. Generally, the more aligned a fabric is, the more it deviates from isotropic flow patterns, and this alignment can come from margins and shear zones (Hudleston 1980; Azuma et al. 1985; Jackson and Kamb 1997). Margins can also have increased temperatures as deformational, frictional and geothermal heating warms the ice (Bjornsson et al. 1996; Engelhardt 2004). Longitudinally aligned fabrics and warmer ice flow faster, while transverse fabrics and cold ice flow slower. The scope and placement of these parameters determine whether the whole glacier speeds up or slows down, an effect that is emphasized at the lateral margins more than it is in the center of the ice. Even if marginal aligned ice has a lesser area than the isotropic parts of an ice body, it can increase flux more than a greater amount of central aligned ice (Figures 3.15 and 3.16). This margin relationship to flow is similar with temperature as well. If this were not the case, the slopes of the border model figures (3.15 to 3.19) would be linear. In short, within the bounds of this project, lateral margins matter in glacial flow models.

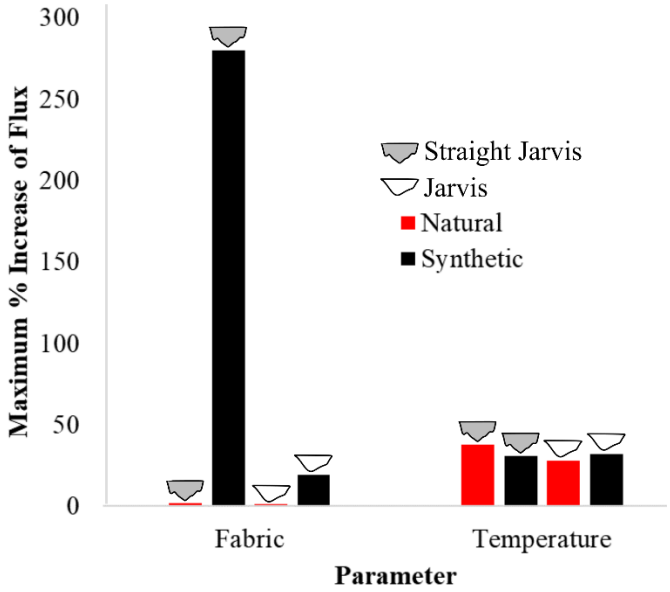

Figure 5.1: Flux differences in synthetic and natural end-members. Percent increase in flux from the lower end-member to the higher end-member is shown here for straight Jarvis and Jarvis geometries. These values are the highest possible flow change within my prescribed fabric and temperature variations in the non-slipping model.

Results of the synthetic model show the potential at which flow can change based on fabric and temperature as I have defined them (Figure 5.1). It is unlikely for a temperate glacier to have entirely aligned fabrics at -10˚C, but if this were to occur then we could see flow increases as much as triple that of an isotropic model, with fabric varying flow more than temperature. By adding just 10 m of highly oriented crystals to the sides of an ice body, flow increases by 26% and that number rises the farther into the glacier I assign the oriented fabric. The model produces similar patterns with temperature changes, though not to the same extreme. In these anisotropic border models (Figures 3.15 through 3.19), we also see an interesting phenomenon where, if I apply an isotropic or cold border to the model, there is a resistance to flow. This flattens out or reverses the slope of the property area vs. flux relationship, until there is enough easily-deformable ice in the system to dominate flow again, usually around 60-70% of the area.

When modeling natural fabrics and temperatures, we see a flip of importance in the two conditions: temperature causes a greater change in flow than fabric because of the weaker fabric concentrations. Including the less oriented lateral margin fabrics of Jarvis into the model does not deviate flow significantly from the isotropic case. Others have determined that in non-temperate settings, temperature is more influential to flow on smaller spatial scales, while fabric is more influential on larger spatial scales (Minchew et al. 2018). Therefore, even if Jarvis were a polar system, its short 8 km length is still more likely to be affected by temperature unless a highly concentrated fabric existed within the ice. However, while it is not necessary to include weakly oriented fabric into the Jarvis Glacier model, more concentrated fabrics in other systems could still impact flow.

Increased fabric concentrations do become more likely when we are discussing cold polar ice, like those of ice sheets or ice streams. When temperatures are far from the melting point, fabrics can concentrate to as much as 30% of c-axes per 1% area, or three times as concentrated as fabrics in temperate ice (Gow and Williamson 1976). Also, the colder the ice, the less of an ability it has to slip, meaning there is more influence from deformational heating on flow (Clarke et al. 1977). While there are feedback loops between fabric and deformational heating (Minchew et al. 2018), as well as many other environmental variables, it is apparent that glacial flow in these cold-ice regions could be significantly affected by marginal properties, as this project shows with the synthetic frozen-bed models. Consequently, polar regions like Greenland and Antarctica are also where ice sheets that will produce meters of sea level rise exist, and where flow can be the cause of half of ice mass loss into the oceans (Rignot and Kanagaratnam 2006). Currently, West Antarctica is dominating that continent's ice loss because of the acceleration of Pine Island and Thwaites Glaciers (Rignot et al. 2008; Pritchard et al. 2012). Once ice shelves thin and their

buttressing effect is gone from these glaciers, the only thing holding back ice flow will be bed and lateral margin stresses, and when it comes to ice streams, lateral margin resistance is what determines flow (Jackson and Kamb 1997; Raymond et al. 2001).

5.2 Looking to the Future

Research on the Greenland Ice Sheet has shown increasing mass loss over the past decades, half from melt and half a result of increasing velocities (Krabill et al. 2004; Rignot and Kanagaratnam 2006). In systems where dynamics are a significant player in flow, if only melt and mass balance are accounted for then models would be underestimating impacts of disappearing ice (Krabill et al. 2004; Rignot et al. 2008). This project has shown that, when modeling those dynamics, there are common assumptions made (like isotropy) which could be detrimental to our predictions. While lateral margins may be negligible for bodies as large as ice sheets, the polar ice streams and glaciers draining those ice sheets are still greatly impacted by their margins (Echelmeyer et al. 1994). Since ice is anisotropic, specific properties at the margins such as fabric can change glacial flow. If we are getting our current flow predictions wrong because of an assumption, how can we expect to accurately predict the future of these ice bodies?

Elmer/Ice and GOLF consider the nuances of anisotropy and are therefore a valid method to replace traditional flow equations. However, scientists and programmers could put further work into this model's compatibility with other aspects of the Elmer/Ice system. Currently, the AIFlow Solver does not communicate with others in the library, like the heat transfer solver, and the connection of these solvers would be valuable when answering questions regarding deformational heating at the margins. Broadening the capabilities of AIFlow would allow a user to include more variables and parameters seen in natural systems (such as water content and till deformation), rather than restricting themselves to just temperature and fabric, elevating this model into a more

realistic realm. However, while my model is unable to communicate with all aspects of the greater Elmer/Ice interface, it still can capture some feedback loops and deviations that happen in natural systems, like rough beds creating pockets of stagnant ice and aligned-fabric margins concentrating velocity gradients to the lateral edges of the ice body. The two solvers created for this project enhance these, allowing the user to choose the locations of specific fabrics and temperatures within the ice body, meaning we no longer need to apply enhancement factors to models. Instead, we can directly apply observations to their locations within the ice. I will make tutorials for these solvers and the methods of this project available online for those who are interested in furthering this work or using this method in their own research or classes.

With the ability to model ice as a non-Newtonian, anisotropic material specific to *in situ* observations, it is clear we need more lateral margin data to create a wider base for modeling. While our *in situ* Jarvis data do not immediately shout the importance of lateral margin properties, others have found that ice at the lateral margins does behave differently than ice at the center of flow (Jackson and Kamb 1997), and the synthetic aspects of this project show that as well. As scientists collect more data, we could determine the range of uniqueness of lateral margin properties and assess whether Jarvis is the outlier or the norm.

Thinking specifically about Jarvis, marginal fabric has little impact on its flow, so surrounding mountain communities can keep current predictions of drinking water availability and tourism for use in adaptation timelines. Margin temperatures do impact glacial flow, as seen with the overall variation in Jarvis's temperatures applied to the border model, but the placement of recorded temperatures varies with depth rather than with proximity to the lateral margin. Due to this, it is unclear whether there is a relationship between temperature and lateral margin flow resistance in Jarvis. To remedy this unknown, I would urge the scientists working on Jarvis to

collect more temperature measurements with depth throughout the glacier, both near and far to the margins, to see if the temperatures recorded at our field site are representative of the rest of the glacier or if warm margins do appear in the ice at other locations.

In conclusion, we can't discount lateral margins in modeling studies. Varying temperatures and concentrated fabrics increase or decrease flow from the isotropic case based on their mechanics: warm temperatures and concentrated longitudinal single-maximum fabrics increase flow while cold temperatures and concentrated transverse single-maximums decrease flow. If fabrics at the margins are less concentrated, i.e. small temperate mountain glaciers like Jarvis, then temperature influences the 3D velocity more than anisotropy. Either way, the scientific community needs more *in situ* data to know exactly what to expect at the margins regarding parameters such as temperature and fabric. With enhanced knowledge of lateral margins and the computing power of the 21st century, we can further our modeling practices to better predict how our home will change in the coming decades.

BIBLIOGRAPHY

Adhikari S, Marshall SJ. 2012. Parameterization of lateral drag in flowline models of glacier dynamics. 58(212):1119–1132. doi:10.3189/2012JoG12J018.

Alley RB. 1988. Fabrics in polar ice sheets: Development and prediction. Science (80-). 240(4851):493–495. doi:10.1126/science.240.4851.493.

Alley RB. 1992. Flow-law hypothesis for ice-sheet modeling. J Glaciol. 38(129):245–256.

Azuma N, Higashi a. 1985. Formation processes of ice fabric pattern in ice sheets. Ann Glaciol. 6(120):130–134. doi:10.1145/3209219.3209221.

Azuma N, Nakawo M, Higashi A, Nishio F. 1985. Flow pattern near Massif A in the Yamato Bare Ice Field estimated from structures and the mechanical properties of a shallow ice core. :173–183.

Bindschadler RA. 1983. The importance of pressurized subglacial water in separation and sliding at the glacier bed. J Glaciol. 29(101):3–19.

Bjornsson H, Gjessing Y, Hamran S-E, Olav Liestol JOH, Palsson F, Erlingsson B. 1996. The thermal regime of sub-polar glaciers mapped by multi-frequency radio-echo sounding. J Glaciol. 42(140):23–32.

Bons PD, Kleiner T, Llorens MG, Prior DJ, Sachau T, Weikusat I, Jansen D. 2018. Greenland Ice Sheet: Higher Nonlinearity of Ice Flow Significantly Reduces Estimated Basal Motion. Geophys Res Lett. 45(13):6542–6548. doi:10.1029/2018GL078356.

Bradley RS, Vuille M, Diaz HF, Vergara W. 2006. Threats to water supplies in the tropical andes. Science (80-). 312(5781):1755–1756. doi:10.1126/science.1128087.

Braedstrup C., Egholm DL, Ugelvig SV, Pedersen VK. 2016. Basal shear stress under alpine glaciers : insights from experiments using the iSOSIA and Elmer/Ice models. Earth Surf Dyn. 4:159–174. doi:10.5194/esurf-4-159-2016.

Budd WF, Warner RC, Jacka TH, Li J, Treverrow A. 2013. Ice flow relations for stress and strain-rate components from combined shear and compression laboratory experiments. J Glaciol. 59(214):374–392. doi:10.3189/2013JoG12J106.

Clarke GKC, Nitsan U, Paterson WSB. 1977. Strain heating and creep instability in glaciers and ice sheets. Rev Geophys. 15(2):235–247. doi:10.1029/RG015i002p00235.

Cohen D, Iverson NR, Hooyer TS, Fischer UH, Jackson M, Moore PL. 2005. Debris-bed friction of hard-bedded glaciers. J Geophys Res. 110(February):1–15. doi:10.1029/2004JF000228.

Colbeck SC, Evans RJ. 1973. A flow law. J Glaciol. 12(64):71–86.

Collao-barrios G, Gillet-chaulet F, Favier V, Casassa G, Berthier E, Dussaillant I, Mouginot J, Rignot E. 2018. Ice flow modelling to constrain the surface mass balance and ice discharge of San Rafael Glacier , Northern Patagonia Icefield. J Glaciol. 64:568–582. doi:10.1017/jog.2018.46.

Cuffey K., Paterson WSB. 2010. The Physics of Glaciers. Fouth. Elsevier.

Duval P. 1977. The role of the water content on the creep rate of polycrystalline ice. Int Assoc Hydrol Sci. 118:29–33. doi:10.1109/CDCS.2001.918692.

Duval P, Montagnat M, Grennerat F, Weiss J, Meyssonnier J, Philip A. 2010. Creep and plasticity of glacier ice: A material science perspective. J Glaciol. 56(200):1059–1068. doi:10.3189/002214311796406185.

Echelmeyer KA, Harrison WD, Larsen C, Mitchell JE. 1994. The role of the margins in the dynamics of an active ice stream. J Glaciol. 40(136):527–538.

Engelhardt H. 2004. Ice temperature and high geothermal flux at Siple Dome, West Antarctica, from borehole measurements. J Glaciol. 50(169):251–256. doi:10.3189/172756504781830105.

Gagliardini O, Meyssonnier J. 1999. Analytical derivations for the behavior and fabric evolution of a linear orthotropic ice polycrystal. J Geophys Res. 104(B8):17797–17809. doi:00118.2007 [pii] 10.1152/japplphysiol.00118.2007.

Gagliardini O, Zwinger T, Gillet-Chaulet F, Durand G, Favier L, De Fleurian B, Greve R, Malinen M, Martín C, Räback P, et al. 2013. Capabilities and performance of Elmer/Ice, a new-generation ice sheet model. Geosci Model Dev. 6(4):1299–1318. doi:10.5194/gmd-6-1299-2013.

Gerbi, C. 2018. Crystallographic orientations in the lateral margin of Jarvis Glacier, Eastern Alaska Range. American Geophysical Union Fall Meeting, December 2018.

Gerrard JA., Perutz M., Roch A. 1952. Measurement of the Velocity Distribution along a Vertical Line through a Glacier. Proc R Soc Lond A Math Phys Sci. 213(1115):546–558. doi:10.3318/has.

Gillet-Chaulet F. 2006. Flow-induced anisotropy in polar ice and related ice-sheet flow modelling. J Nonnewton Fluid Mech. 134(1–3 SPEC. ISS.):33–43. doi:10.1016/j.jnnfm.2005.11.005.

Gillet-Chaulet F, Gagliardini O, Meyssonnier J, Montagnat M, Castelnau O. 2005. A user-friendly anisotropic flow law for ice-sheet modelling. J Glaciol. 51(172):3–14. doi:10.3189/172756505781829584.

Glen JW. 1952. Experiments on the Deformation of Ice. J Glaciol. 2(12):111–114. doi:10.1017/S0022143000034067.

Glen JW. 1955. The Creep of Polycrystalline Ice. Proc R Soc Lond A Math Phys Sci. 228(1175):519–538.

Goldsby DL, Kohlstedt DL. 2001. Superplastic deformation of ice: Experimental observations. J Geophys Res. 106(B6):11017–11030. doi:10.1029/2000JB900336.

Gow AJ, Williamson T. 1976. Rheological implications of the internal structure and crystal fabrics of the West Antarctic ice sheet as revealed by deep core drilling at Byrd Station. Bull Geol Soc Am. 87(12):1665–1677. doi:10.1130/0016-7606(1976)87<1665:RIOTIS>2.0.CO;2.

Graham FS, Morlighem M, Warner RC, Treverrow A. 2017. Implementing an empirical scalar tertiary anisotropic rheology (ESTAR) into large-scale ice sheet models. Cryosph Discuss.(May):1–26. doi:10.5194/tc-2017-54.

Haefeli R. 1952. Observation on the quasi-viscous behaviour of ice in a tunnel in the Z'Mutt Glacier. J Glaciol.:94–99.

Haseloff M, Schoof C, Gagliardini O. 2018. The role of subtemperate slip in thermally driven ice stream margin migration. Cryosph. 12:2545–2568.

Herron SL, Langway CC. 1982. A comparison of ice fabrics and textures at Camp Century, Greenland, and Byrd Station, Antarctica. Ann Glaciol. 3(Mardia 1972):118–124.

Hooke R. 1981. Flow Law for Polycrystalline Ice in Glaciers: Comparison of Theoretical Predictions, Labratory Data and Field measurements. Rev Geophys Sp Phys. 19(4):664–672. doi:10.1029/RG019i004p00664.

Hooke RL, Hudleston PJ. 1981. Ice fabrics from a borehole at the top of the South Dome, Barnes ice cap, Baffin Island. Geol Soc Am Bull. 92(5 pt.1):274–281.

Hudleston PJ. 1980. The progressive development of inhomogeneous shear and crystallographic fabric in glacial ice. J Struct Geol. 2(1–2):189–196. doi:10.1016/0191-8141(80)90049-8.

Hudleston PJ. 2015. Structures and fabrics in glacial ice: A review. J Struct Geol. 81:1–27. doi:10.1016/j.jsg.2015.09.003.

Jackson M, Kamb B. 1997. The marginal shear stress of Ice Stream B , West Antarctica. J Glaciol. 43(145):415–426.

Kienholz C, Hock R, Truffer M, Bieniek P, Lader R. 2017. Mass Balance Evolution of Black Rapids Glacier, Alaska, 1980–2100, and Its Implications for Surge Recurrence. Front Earth Sci. 5(July). doi:10.3389/feart.2017.00056.

Krabill W, Hanna E, Huybrechts P, Abdalati W, Cappelen J, Csatho B, Frederick E, Manizade S, Martin C, Sonntag J, et al. 2004. Greenland Ice Sheet: Increased coastal thinning. Geophys Res Lett. 31(24):1–4. doi:10.1029/2004GL021533.

Lee IR, Hawley RL, Bernsen S, Gerbi CC, Clemens-Sewall D, Campbell SW, Waszkiewicz M, Kreutz KJ. 2018. Collection and analysis of shear strain data of polythermal ice from Jarvis Glacier, Alaska. American Geophysical Union Fall Meeting, December 2018. https://agu.confex.com/agu/fm18/prelim.cgi/Paper/365323

Lee I. 2019. Borehole tilt sensor data for Jarvis Glacier, Alaska (2017-2018). Arctic Data Center. doi:10.18739/A2348GG12

Lipenkov VY, Barkov NI, Duval P, Pimienta P. 1989. Crystalline texture of the 2083 m ice core at Vostok Station, Antarctica. J Glaciol. 35(121):392–398.

Ma Y, Gagliardini O, Ritz C, Gillet-Chaulet F, Durand G, Montagnat M. 2010. Enhancement factors for grounded ice and ice shelves inferred from an anisotropic ice-flow model. J Glaciol. 56(199):805–812. doi:10.3189/002214310794457209.

Mangeney A, Califano F, Hutter K. 1997. A numerical study of anisotropic, low Reynolds number, free surface flow of ice sheet modeling. J Geophys Res. 102(B10):749–764. doi:10.1029/97JB01697.

Maohuan H. 1990. On the temperature distribution of glaciers in China. J Glaciol. 36(123):210–216.

Martín C, Gudmundsson GH. 2012. Effects of nonlinear rheology, temperature and anisotropy on the relationship between age and depth at ice divides. Cryosphere. 6(5):1221–1229. doi:10.5194/tc-6-1221-2012.

Martin C, Gudmundsson GH, Pritchard HD, Gagliardini O. 2009. On the effects of anisotropic rheology on ice flow , internal structure , and the age-depth relationship at ice divides. J Geophys Res. 114:1–18. doi:10.1029/2008JF001204.

Mellor M, Testa R. 1969. Effect of temperature on the creep of ice. J Glaciol. 8(52):131–145.

Le Meur E, Gagliardini O, Zwinger T, Ruokolainen J. 2004. Glacier flow modelling: A comparison of the Shallow Ice Approximation and the full-Stokes solution. Comptes Rendus Phys. 5(7):709–722. doi:10.1016/j.crhy.2004.10.001.

Minchew BM, Meyer CR, Robel AA, Gudmundsson GH, Simons M. 2018. Processes controlling the downstream evolution of ice rheology in glacier shear margins : case study on Rutford Ice Stream , West Antarctica. J Glaciol. 64:583–594. doi:10.1017/jog.2018.47.

Miner KR, Campbell S, Gerbi C, Liljedahl A, Anderson T, Perkins LB, Bernsen S, Gatesman T, Kreutz KJ. 2018. Organochlorine pollutants within a polythermal glacier in the interior Eastern Alaska Range. Water (Switzerland). 10(9):1–14. doi:10.3390/w10091157.

Montagnat M, Castelnau O, Bons PD, Faria SH, Gagliardini O, Grennerat F, Griera A, Lebensohn RA, Moulinec H. 2014. Multiscale modeling of ice deformation behavior. J Struct Geol. 61:78–108.

Mountain Research Initiative EDW Working Group. 2015. Elevation-dependent warming in mountain regions of the world. Nat Clim Chang. 5. doi:10.1038/nclimate2563.

Passalacqua O, Gagliardini O, Parrenin F, Todd J, Gillet-Chaulet F, Ritz C. 2016. Performance and applicability of a 2.5-D ice-flow model in the vicinity of a dome. Geosci Model Dev. 9(7):2301–2313. doi:10.5194/gmd-9-2301-2016.

Payne AJ, Vieli A, Shepherd AP, Wingham DJ, Rignot E. 2004. Recent dramatic thinning of largest West Antarctic ice stream triggered by oceans. 31:1–4. doi:10.1029/2004GL021284.

Pfeffer WT, Humphrey NF, Amadei B, Harper J, Wegmann J. 2000. In situ stress tensor measured in an Alaskan glacier. Ann Glaciol. 31:229–235. doi:doi:10.3189/172756400781820354.

Pimienta P, Duval P, Lipenkov VY. 1987. Mechanical behavior of anisotropic polar ice. Phys Basis Ice Sheet Model (Proceedings Vancouver Symp.(170):57–66.

Planet Team (2017). Planet Application Program Interface: In Space for Life on Earth. San Francisco, CA. https://api.planet.com

Pritchard HD, Ligtenberg SRM, Fricker HA, Vaughan DG, van den Broeke MR, Padman L. 2012. Antarctic ice-sheet loss driven by basal melting of ice shelves. Nature. 484:502–505. doi:10.1038/nature10968.

Purdie H. 2013. Glacier Retreat and Tourism: Insights from New Zealand. Mt Res Dev. 33(4):463–472. doi:10.1659/MRD-JOURNAL-D-12-00073.1.

Radić V, Hock R. 2011. Regionally differentiated contribution of mountain glaciers and ice caps to future sea-level rise. Nat Geosci. 4(2):91–94. doi:10.1038/ngeo1052.

Raymond CF, Echelmeyer KA, Whillans IM, Doake CSM, Alley RB, Bindschadler RA. 2001. Ice stream shear margins. West Antarct ice sheet Behav Environ Antarct Res Ser. 77:137–155.

Rignot E, Bamber JL, van den Broeke MR, Davis C, Li Y, Jan van de Berg W, van Meijgaard E. 2008. Recent Antarctic ice mass loss from radar interferometry and regional climate modelling. Nat Geosci. 1:106–110. doi:10.1038/ngeo102.

Rignot E, Kanagaratnam P. 2006. Changes in the velocity structure of the Greenland Ice Sheet. Science (80-). 311(5763):986–990. doi:10.1126/science.1121381.

Ritter F, Fiebig M, Muhar A. 2012. Impacts of Global Warming on Mountaineering: A Classification of Phenomena Affecting the Alpine Trail Network. Mt Res Dev. 32(1):4–15. doi:10.1659/MRD-JOURNAL-D-11-00036.1.

Russell-Head DS, Budd WF. 1979. Ice-sheet flow properties derived from bore-hole shear measurements combined with ice-core studies. J Glaciol. 24(90):117–130. doi:10.1017/S0022143000014684.

Seddik H, Greve R, Zwinger T, Gillet-Chaulet F, Gagliardini O. 2012. Simulations of the Greenland ice sheet 100 years into the future with the full Stokes model Elmer/Ice. J Glaciol. 58(209):427–440. doi:10.3189/2012JoG11J177.

Seddik H, Greve R, Zwinger T, Placidi L. 2011. A full Stokes ice flow model for the vicinity of Dome Fuji, Antarctica, with induced anisotropy and fabric evolution. Cryosphere. 5(2):495–508. doi:10.5194/tc-5-495-2011.

Thorsteinsson T, Kipfstuhl J, Miller H. 1997. Textures and fabrics in the GRIP ice core. J Geophys Res Ocean. 102(C12):26583–26599. doi:10.1029/97JC00161.

Treverrow A, Warner RC, Budd WF, Jacka TH, Roberts JL. 2015. Modelled stress distributions at the Dome Summit South borehole, Law Dome, East Antarctica: a comparison of anisotropic ice flow relations. J Glaciol. 61(229):987–1004. doi:10.3189/2015JoG14J198.

Vaughan DG, Arthern R. 2007. Why Is It Hard to Predict the Future of Ice Sheets ? Science (80). 315(5818):1503–1504.

Wang Y, Thorsteinsson T, Kipfstuhl J, Miller H, Dahl-Jensen D, Shoji H. 2002. A vertical girdle fabric in the NorthGRIP deep ice core, North Greenland. Ann Glaciol. 35:515–520. doi:10.3189/172756402781817301.

Warner G, Cloud G. 1974. Measurement of Surface Strain Rates in Glaciers Using Embedded Wire Strain Gages. Exp Mech. 14(1):24–28.

Wilson CJL, Sim HM. 2002. The localization of strain and c -axis evolution in anisotropic ice. J Glaciol. 48(163):601–610.

Wu T, Christensen R. 1964. Measurement of surface strain-rate on Taku Glacier, Alaska. J Glaciol.

Zhao L, Tian L, Zwinger T, Ding R, Zong J, Ye Q, Moore JC. 2014. Numerical simulations of Gurenhekou glacier on the Tibetan Plateau. J Glaciol. 60(219):71–82. doi:10.3189/2014JoG13J126.

Zwinger T, Greve R, Gagliardini O, Shiraiwa T, Lyly M. 2007. A full Stokes-flow thermo-mechanical model for firn and ice applied to the Gorshkov crater glacier , Kamchatka. Ann Glaciol. 45:29–37.

APPENDIX A: SYNTHETIC MODELS

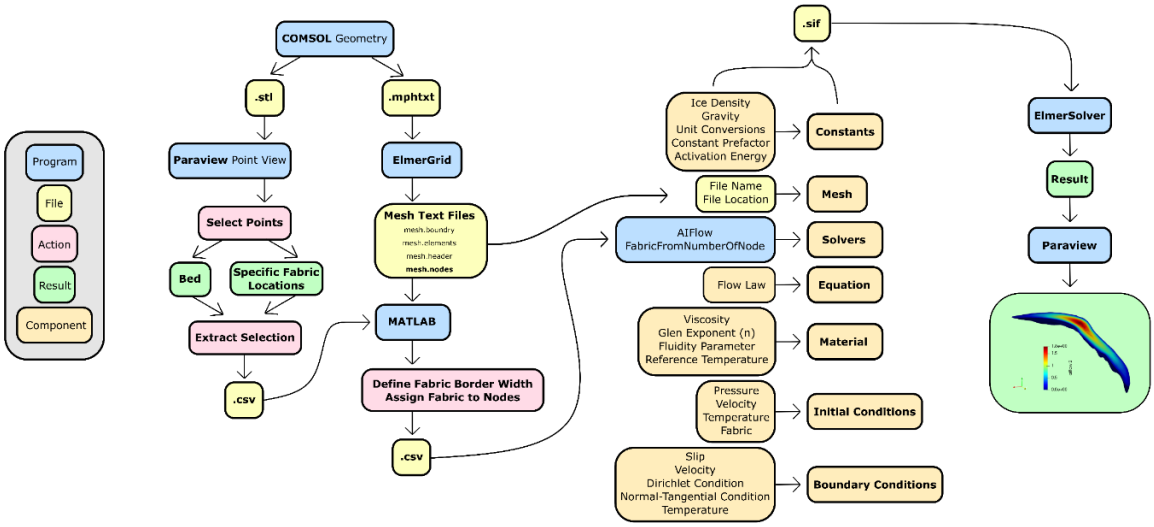

Figure A1: Workflow diagram for the modeling process.

Viscosity File	Beta	Gamma	Stress Exponent	Fabric	Maximum Velocity (m/a)
1	0.04	1	1	max, x	3.7
				max, z	0.461
4	0.01	1	1	max, x	8.1
				max, z	0.442
15	0.03	1	1	max, x	4.5
				max, z	0.455
24	0.05	1	1	max, x	3.3
				max, z	0.466
34	0.07	1	1	max, x	2.6
				max, z	0.476
49	0.1	1	1	max, x	2.1
				max, z	0.488

Table A1: Information on representative viscosity files. Files with different gammas were also tried, but beta causes a greater variation in velocity than gamma, so beta was chosen as the variable to change here.

Cone angle of single maximum perpendicular to the bed (˚)	Flux increase from isotropic case (%)
45	-2.1
30	-4.3
15	-8.4

Table A2: Cone angles of rotating fabric compared to the isotropic model. Run on the straightened Jarvis with a temperature of -1˚C.

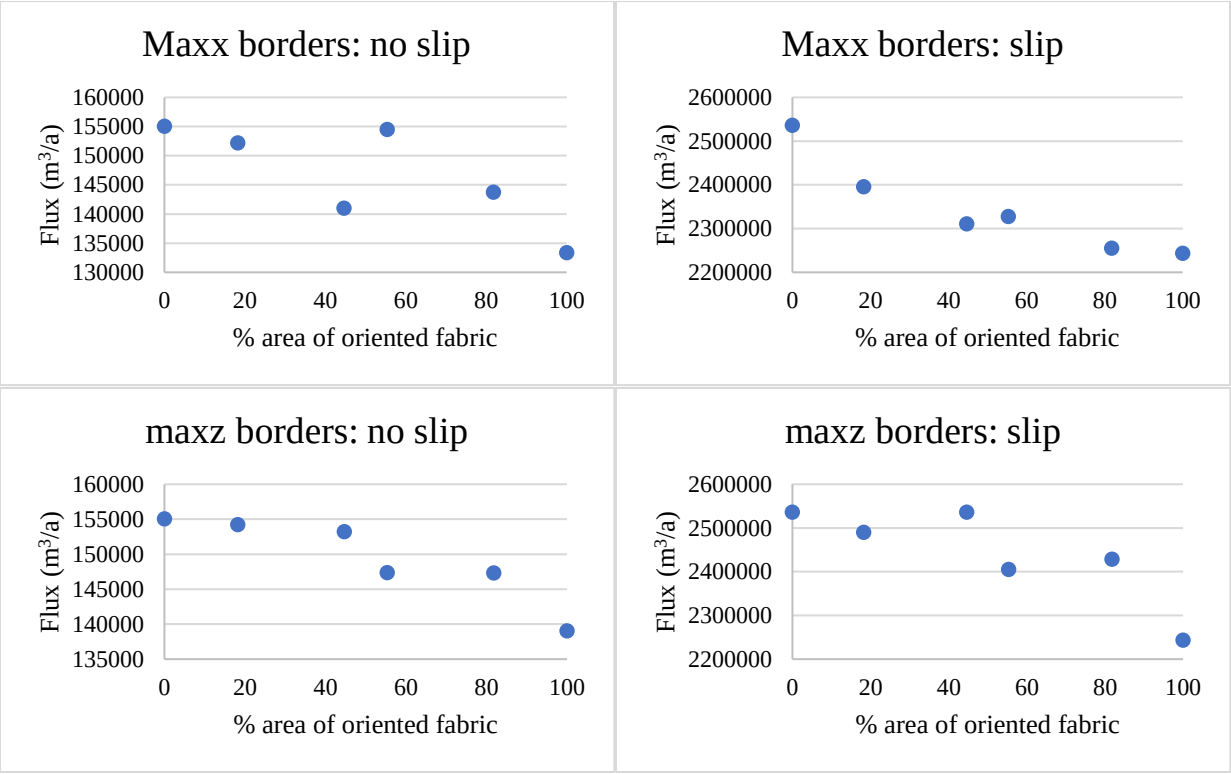

Figure A2: Border model fluxes for the off-longitudinal single-maximum runs. These are the transverse single-maximum (maxx) and vertical single-maximum (maxz) fabrics. Run on the straightened Jarvis without and with slip.

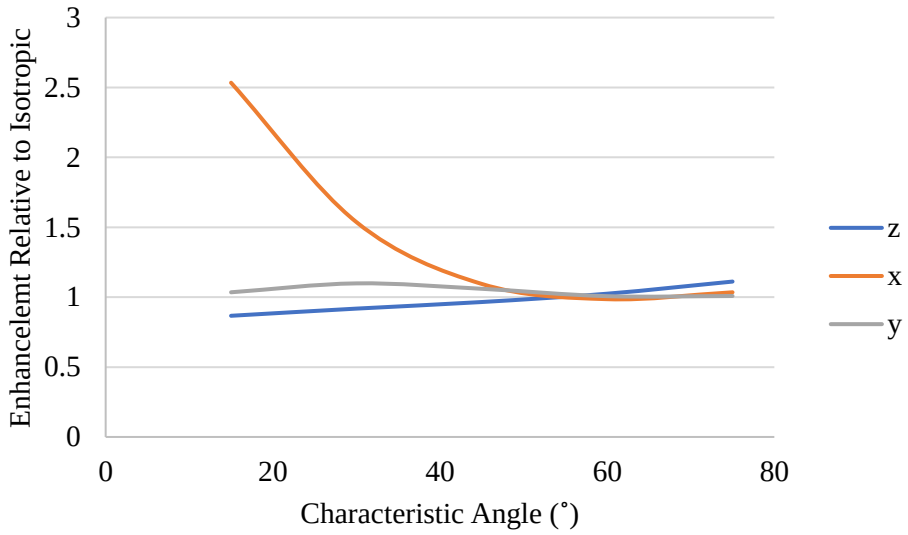

Figure A3: Small circle fabrics versus enhancement factor. Enhancement factor is the anisotropic flux over the isotropic flux. Colors record the axis the fabric circles. The width of each small circle band is 30˚. Run on the half-cylinder with no slip. Model is based on Hudleston, 2015 Figure 3 (Hudleston 2015).

APPENDIX B: CASE STUDY GLACIER DATA AND MODELING

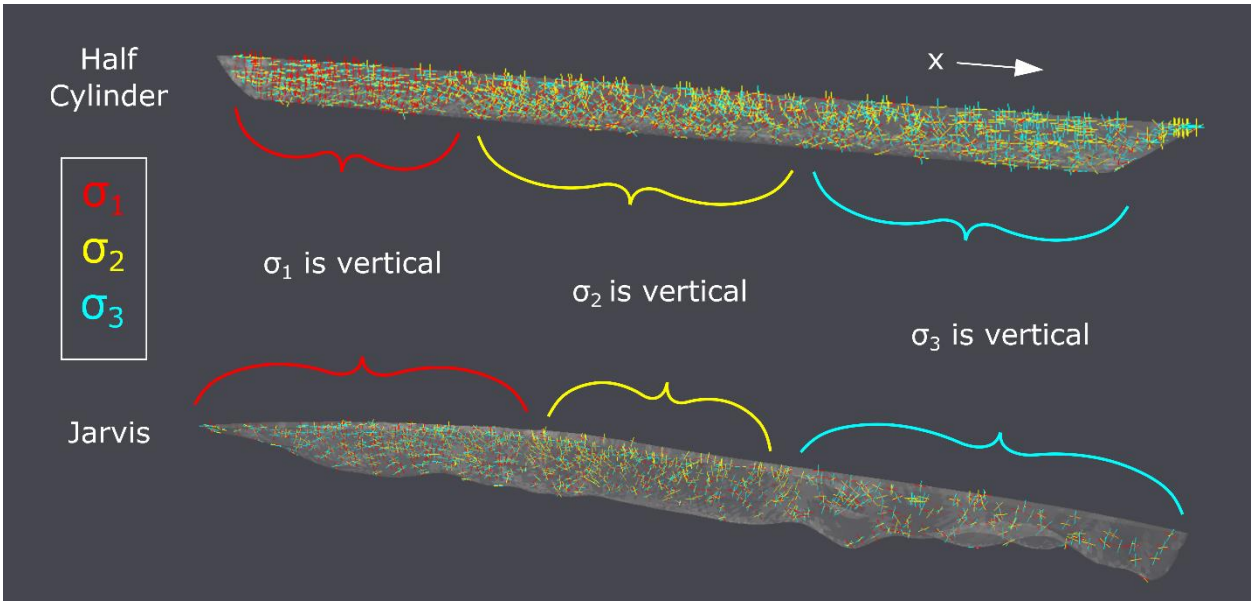

Figure B1: Principal stresses of a glacier. Depending on the distance from the accumulation area, the stresses change from a vertical σ_1 to a vertical σ_3 regime. Principal stresses transition between regimes depending on the area of the glacier; in the accumulation area, where the snow is being compressed into ice as more snow falls each year, the maximum principal stress is vertical. As the glacier moves out of the accumulation area, σ_1 rotates to the horizontal as lateral shear dominates flow. The farther from the accumulation area you get, the smaller the vertical principal stress gets, until it is finally the lowest of the three stresses at the toe of the glacier. A rough bedrock does change the stress regimes locally, but the overall patterns of the principal stresses stay the same.

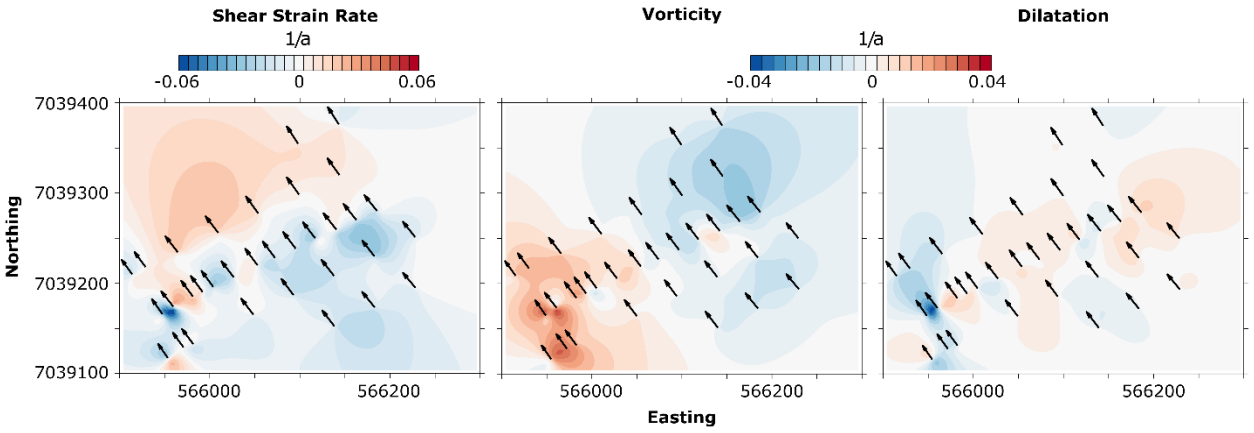

Figure B2: Surface strain rates of the field site. Shear strain rate, vorticity and dilatation are calculated from the surface velocity measured from July 2017 to August 2018. Black arrows are the velocity vectors at each of the stakes left in the ice for the year, length to scale.

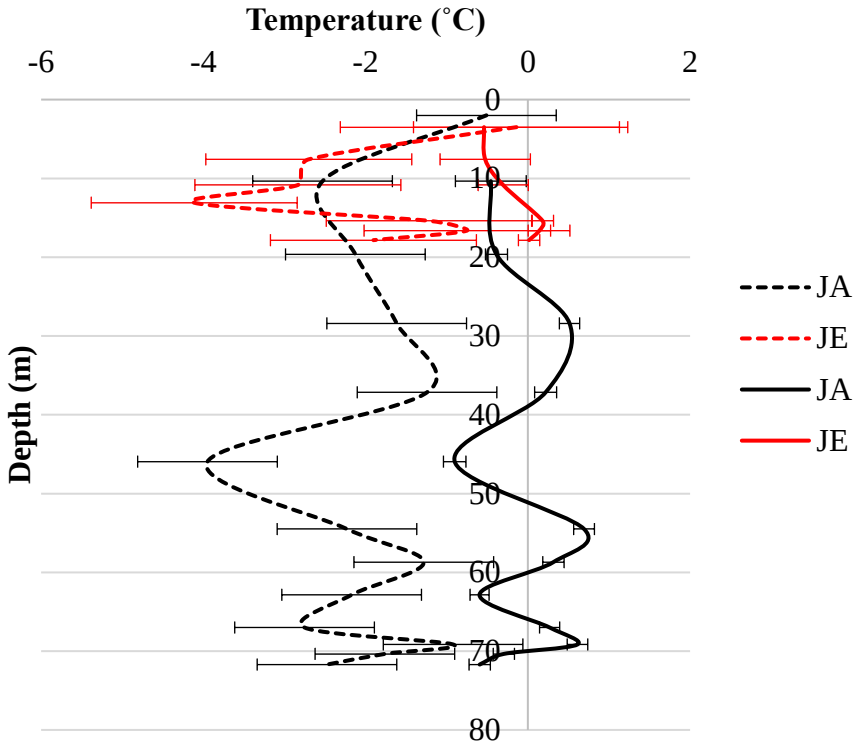

Figure B3: Annual temperature data compared to July 2017 data. Annual temperature data was collected 7/28/17-8/7/18, and July data was collected 7/11/17 to 7/28/17. Annual data are solid lines, dotted lines are the July data. Cold and warm patterns persist through the ice despite the length of the record. Data from Lee 2019.

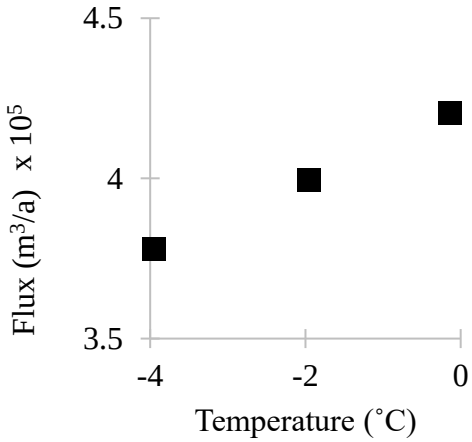

Figure B4: Flux versus temperature for July 2017 core data. Minimum, maximum and average temperatures in the two cores from July 11th, 2017 to July 28th, 2017 ranged between -4 and 0˚C. July and August are normally the warmest months, but in 2017, July ice temperatures did not reach above 0˚C.

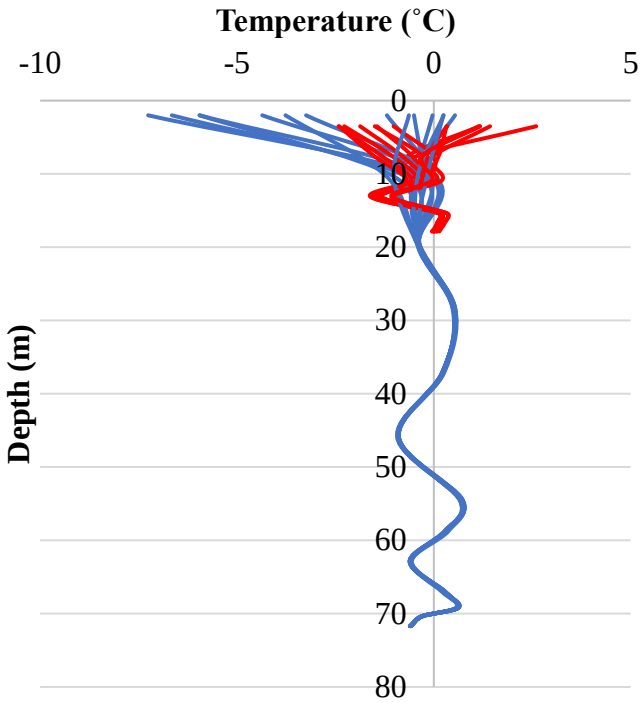

Figure B5: Monthly temperature averages with depth from July 28th, 2017 to August 7th, 2018. Blue are data from the JA core, red are data from the JE core. Standard deviation below 20 m is, on average, less than 0.14. From 10-20 m standard deviation is 0.21 and above 10 m it is 1.16. Data from Lee 2019.

SAMPLE NAME	DEPTH (M)	# OF GRAINS	A2_11	A2_22	A2_33	A2_12	A2_23	A2_13
JA10	4	220	0.24	0.33	0.44	-0.027	-0.11	-0.042
JA10	4	13	0.12	0.61	0.27	-0.078	-0.12	0.0014
JA22	11	309	0.37	0.23	0.4	-0.032	-0.076	0.038
JA35	21	180	0.25	0.4	0.35	-0.014	-0.077	-0.023
JA48	30	76	0.35	0.25	0.4	0.13	-0.14	-0.025
JA58	35	192	0.34	0.35	0.31	-0.11	-0.083	-0.065
JA72	45	25	0.32	0.48	0.19	-0.0028	0.058	-0.046
JA74		32	0.5	0.31	0.19	0.24	0.095	0.17
JA80	49	14	0.74	0.11	0.15	0.15	-0.015	0.04
JA87	55	430	0.19	0.45	0.36	-0.053	-0.13	-0.0011
JA91	56	24						
JA96	60	86						
JA106	65	32						
JA112	69	45						
JA117	72	22						
JA122		20						
JA128	76	26						
JA132	79	19						
JE1	0	75	0.16	0.72	0.12	-0.064	0.019	-0.034
JE5		45	0.15	0.75	0.11	0.096	0.027	-0.038
JE7	4	99						
JE10	6	48	0.64	0.25	0.11	-0.0084	-0.047	-0.0084
JE12	8	45	0.15	0.75	0.11	0.096	0.027	-0.038
JE15	10							
JE21	14	27						
JE24		29	0.56	0.33	0.11	0.23	-0.11	-0.056

Table B1: Fabric orientation data for the JA and JE cores. Data collected by Chris Gerbi. This table represents data collected at the time of modeling and has since been completed.

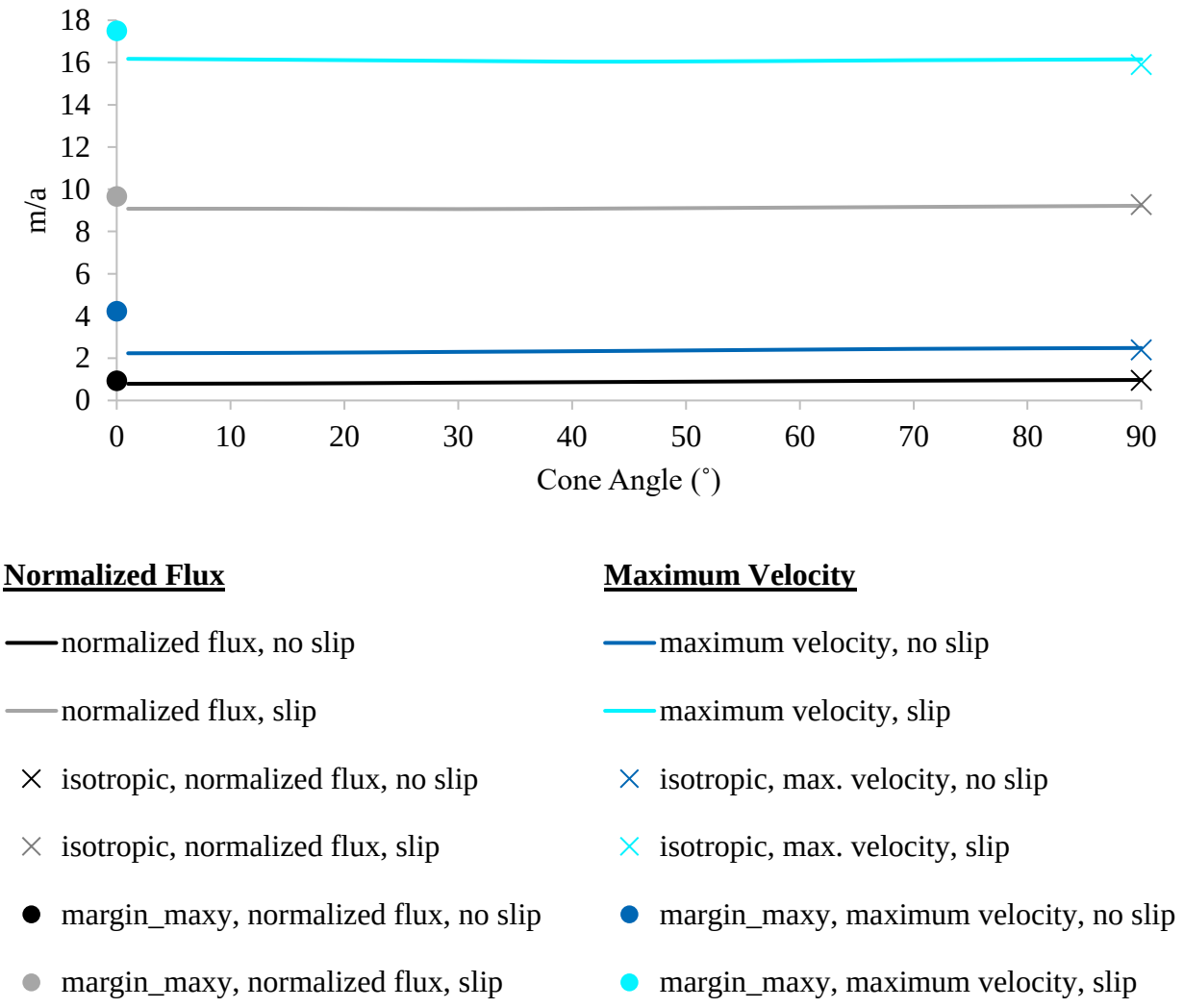

Figure B6: Maximum velocity and flux for lateral margin runs. Flux is normalized to area for all runs, both slipping and non-slipping in the Jarvis geometry. Lines are cone angle variations, circles are longitudinal single-maximum (maxy) fabric at the lateral margin, and x's are the all-isotropic model. Light colors are slip, dark colors are non-slipping. Grey/black is normalized flux and blues are maximum velocities.

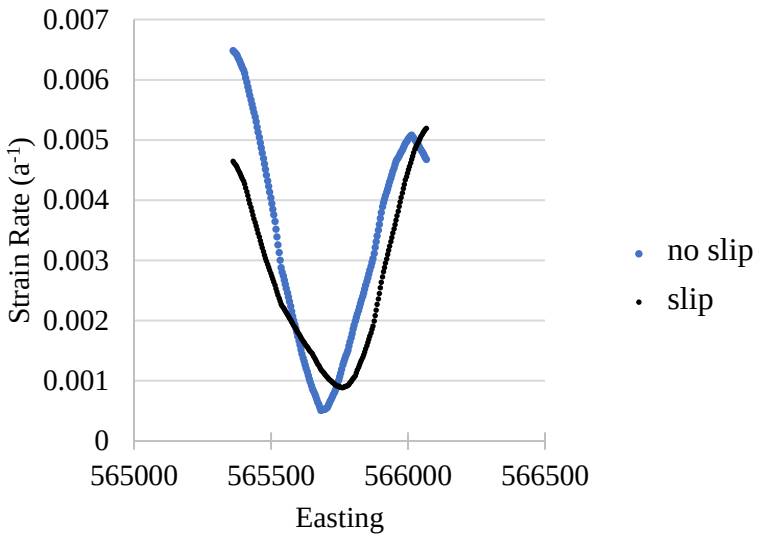

Figure B7: Effective strain rate for a surface transect north of the field site. This location is where the model shows the greatest surface velocity and is past the glacier's curve. These data come from the slipping 175 m border model with fabric rotated to the bed and a temperature of -0.09˚C.

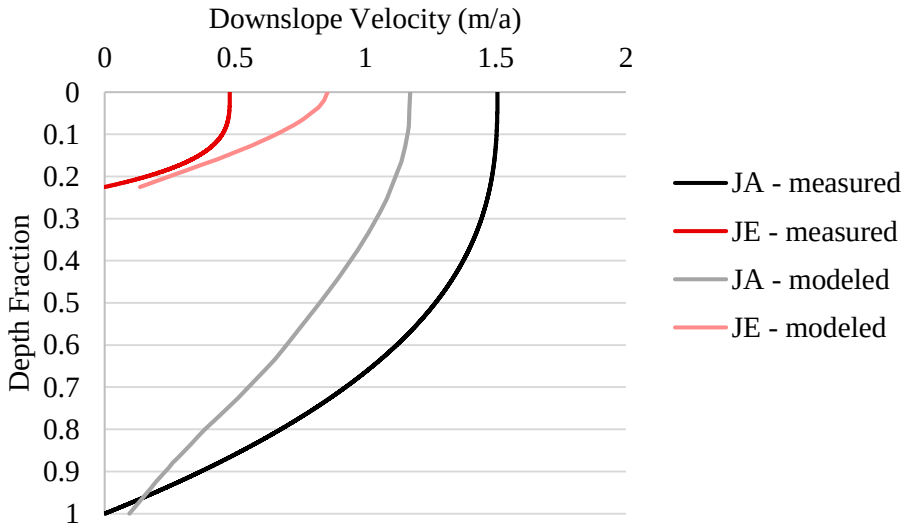

Figure B8: Velocity profiles with depth for the modeled and measured flow without slip or surface velocity applied to the data. Depth fraction is related to the 80 m JA core depth. Measured flow profile is a curve fit to the core deformation data with Glen's flow law (Lee 2018).

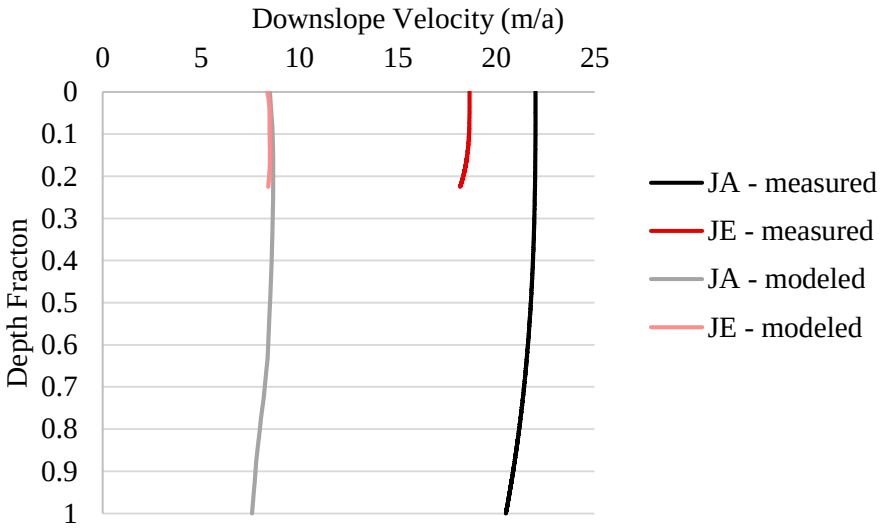

Figure B9: Velocity profiles with depth for the modeled and measured flow with slip. Depth fraction is related to the 80 m JA core depth. Measured flow is a curve fit to the core deformation data with Glen's flow law and added to measured annual surface velocity at each of the core locations (Lee 2018).

BIOGRAPHY OF THE AUTHOR

Kate Hruby is a transplanted northwesterner, growing up in Washington State and journeying east for both her undergraduate and graduate degrees. She graduated in 2016 with her Bachelors of Science in Environmental Science from the University of New England and promptly left land life for one of her passions: sailing. Deciding to take a gap two-years from the maritime industry, she returned to the northeast to obtain a Masters of Science from the University of Maine. After receiving her graduate degree, Kate will return to the water, delving back into the world of outdoor science education and science communication, hopefully deepening the conversation of climate change throughout our country. Kate is a candidate for the Master of Science degree in Earth and Climate Science from the University of Maine in May 2019.